

## The Multilayer Nature of Molecular Gas toward the Cygnus Region

SHIYU ZHANG,<sup>1,2</sup> YANG SU<sup>†,1,2</sup> XUEPENG CHEN,<sup>1,2</sup> MIN FANG,<sup>1,2</sup> QINGZENG YAN,<sup>1</sup> SHAOBO ZHANG,<sup>1</sup> YAN SUN,<sup>1,2</sup>  
XIAOLONG WANG,<sup>3,\*</sup> HAORAN FENG,<sup>1,2</sup> YUEHUI MA,<sup>1</sup> MIAOMIAO ZHANG,<sup>1</sup> ZI ZHUANG,<sup>1,2</sup> XIN ZHOU,<sup>1</sup> ZHIWEI CHEN,<sup>1</sup> AND  
JI YANG<sup>1</sup>

<sup>1</sup>*Purple Mountain Observatory and Key Laboratory of  
Radio Astronomy, Chinese Academy of Sciences, Nanjing 210034,  
People's Republic of China*

<sup>2</sup>*School of Astronomy and Space Science, University of  
Science and Technology of China, 96 Jinzhai Road, Hefei 230026,  
People's Republic of China*

<sup>3</sup>*Department of Physics, Hebei Normal University,  
Shijiazhuang 050024, People's Republic of China*

### ABSTRACT

We study the physical properties and 3D distribution of molecular clouds (MCs) toward the Cygnus region using the MWISP CO survey and Gaia DR3 data. Based on Gaussian decomposition and clustering for <sup>13</sup>CO lines, over 70% of the fluxes are recovered. With the identification result of <sup>13</sup>CO structures, two models are designed to measure the distances of the molecular gas in velocity crowding regions. The distances of more than 200 large <sup>13</sup>CO structures are obtained toward the 150 deg<sup>2</sup> region. Additionally, tens of the identified MC structures coincide well with masers and/or intense mid-IR emission. We find multiple gas layers toward the region: (1) the extensive gas structures composing the Cygnus Rift from 700 pc to 1 kpc across the whole region; (2) the  $\sim 1.3$  kpc gas layer mainly in the Cygnus X South region; and (3) the 1.5 kpc dense filament at the Cygnus X North region and many cometary clouds shaped by Cygnus OB2. We also note that the spatial distribution of young stellar object candidates is generally consistent with the molecular gas structures. The total molecular mass of the Cygnus region is estimated to be  $\sim 2.7 \times 10^6 M_{\odot}$  assuming an X-factor ratio  $X_{\text{CO}} = 2 \times 10^{20} \text{cm}^{-2} (\text{K} \cdot \text{km} \cdot \text{s}^{-1})^{-1}$ . The foreground Cygnus Rift contributes  $\sim 25\%$  of the molecular mass in the whole region. Our work presents a new 3D view of the MCs' distribution toward the Cygnus X region, as well as the exact molecular gas mass distribution in the foreground Cygnus Rift.

*Keywords:* Distance measure (395) — Interstellar medium (847) — Molecular clouds (1072)

### 1. INTRODUCTION

CO surveys are of great importance and helpful for studying MCs directly and coordinating Galactic emission at multiple wavelength bands (Heyer & Dame 2015). In particular, stars are born in the densest parts of MCs, therefore, studies of MCs can accelerate our understanding of the link between star formation and the surrounding molecular gas environment, as well as the large scale structures of the Milky Way (Dame et al. 2001; Schuller et al. 2017; Umemoto et al. 2017).

As one of the most massive nearby star formation regions (SFRs) (Reipurth & Schneider 2008), the Cygnus region harbors giant MC complexes (e.g., DR21, Schneider et al. 2010; Cao et al. 2022) and several OB associations (e.g., the well-known Cygnus OB2, Massey & Thompson 1991; Knödseder 2000; Comerón et al. 2002; Hanson 2003; Wright et al. 2010b, 2015). With Cygnus OB2 in the center, Cygnus X region is divided into the northern and southern parts by Schneider et al. (2006). Hundreds of OB stars toward this region indicate intense star formation activity therein,

Corresponding author: Yang Su  
yangsu@pmo.ac.cn

\* Physics Postdoctoral Research Station at Hebei Normal University

including extended ionized features from HII regions and supernova remnants (SNRs; [Wendker et al. 1991](#); [Anderson et al. 2014](#)), interstellar bubbles ([Abbott et al. 1981](#); [Higgs et al. 1994](#)), and outflows ([Duarte-Cabral et al. 2013](#); [Zhang et al. 2020](#)).

We focus on molecular gas in the whole Cygnus region, especially the gas emission within 1 kpc; including Cygnus X ([Schneider et al. 2006](#)), North America/Pelican (NAP; [Zhang et al. 2014](#)), and other interesting regions. The Cygnus X region is prominent by its strong and extended Galactic radio continuum emission ([Downes & Rinehart 1966](#); [Wendker et al. 1991](#)). The multiple wavelength studies are also fruitful, e.g. CO surveys ([Dame et al. 1987](#); [Schneider et al. 2006](#); [Gottschalk et al. 2012](#); [Yamagishi et al. 2018](#)), CII ([Bonne et al. 2023](#); [Schneider et al. 2023](#)), millimeter continuum ([Motte et al. 2007](#); [Bontemps et al. 2010](#)), and infrared ([Egan et al. 1998](#); [Beer et al. 2010](#); [Hennemann et al. 2012](#); [Schneider et al. 2016](#); [Cao et al. 2019](#)). Recently, many new works have also been presented toward the region (e.g., [Takekoshi et al. 2019](#); [Comerón et al. 2020](#); [Ortiz-León et al. 2021](#); [Quintana & Wright 2021, 2022](#); [Beuther et al. 2022](#); [Dharmawardena et al. 2022](#); [Gong et al. 2023](#)). The NAP region is located adjacent to the massive star-forming regions of Cygnus X in projection. L935 is the densest dark cloud in this region, which separates the North America and Pelican nebulae (see [Figure 1](#)). Evidence of the star formation process across the complex has been revealed by studying MCs and young stellar objects (YSOs; [Zhang et al. 2014](#); [Fang et al. 2020](#)).

Although the Cygnus region has been extensively studied in multiwavelengths, the distances and properties of clouds in the region are not well determined in a global view. Distance uncertainty is one of the major problems in studying the various star forming regions and gas structures/properties in this direction.

The distances of MCs have been subject to considerable debate with several difficulties. Firstly, it is hard to derive the kinematic distances of clouds because of the near–far distance ambiguities in the first quadrant ([Mertsch & Vittino 2021](#)). In fact, the kinematic distances of MCs produce a large uncertainty when the velocity field of gas is crowding in a small velocity range ([Yan et al. 2020](#)). On the other hand, due to the large degree of overlap between the inner and outer Galaxy along the line of sight (LOS), coherent MCs are difficult to distinguish in position–position–velocity (PPV) space. In particular, toward the Cygnus X region, a collective cloud emission across the tangential point overlaps with each other from several hundred parsecs to 2 kpc and even farther in LSR velocities close to zero and velocity gradient smaller than the typical velocity dispersion of interstellar gas ([Reipurth & Schneider 2008](#)).

Some methods have been used to deal with the kinematic distance ambiguities. Different layers may be demonstrated based on the HI self-absorption features toward the Cygnus X ([Gottschalk et al. 2012](#)). The distances of some massive star formation regions (MSFRs) have been precisely determined by the trigonometric parallax of the associated masers ([Rygl et al. 2012](#); [Xu et al. 2016](#)). These methods are limited by the small amount of observed samples and can only focus on some small specific areas, thus lacking an overall understanding of the whole region.

Before Gaia’s age, large distance uncertainties of MCs by photometric methods prevented us from determining the exact 3D distribution of molecular gas. Thanks to the release and convenient acquisition of Gaia DR3 data, huge amounts of stars with parallaxes and extinctions make it possible to accurately measure the distance of MCs. For example, all sky extinction maps are derived by different models based on dust properties ([Chen et al. 2019](#); [Green et al. 2019](#); [Lallement et al. 2019](#); [Hottier et al. 2020](#)). In addition, extinction jump models are applied to distance measurements of MCs ([Yan et al. 2019b](#); [Zucker et al. 2019](#); [Sun et al. 2021a](#); [Guo et al. 2022](#)), and SNRs ([Yu et al. 2019](#); [Zhao et al. 2020](#)). Toward the Cygnus X region, [Orellana et al. \(2021\)](#) revealed that the OB2 association consists of several substructures, ranging from 1.2 to 1.7 kpc based on Gaia DR2 data. The above evidences suggest that the gas and the SFRs toward this direction are chance superpositions of several complexes along the LOS.

Finally, ultrahigh energy (UHE) cosmic rays’ emissions are prevalent in our Galaxy ([Cao et al. 2021](#); [Banik & Ghosh 2022](#)). Several UHE sources are detected toward the Cygnus X region ([Cao et al. 2024](#)). The origin of these UHE sources is still unknown. Are they from hadronic processes from the interaction of high velocity winds of massive stars (e.g. Cygnus OB2) and/or SNR shock (e.g.  $\gamma$ -Cygni) with the surrounding dense molecular gas? Evaluating the molecular gas distribution toward the Cygnus region might be helpful to reveal the possible origin of UHE emission.

This paper is structured as follows. We will introduce the Milky Way Imaging Scroll Painting (MWISP) CO survey and the Gaia DR3 in [Section 2](#). The data processing methods are described in detail, including Gaussian decomposition in [Section 3.1](#) and the clustering algorithm in [Section 3.2](#). In [Section 4](#), we determined the distances and physical properties of identified  $^{13}\text{CO}$  structures. Based on our new distance measurement of MCs, we introduce the physical properties and the 3D distribution of gas structures for several subregions in [Section 5](#), and later, in [Section 6](#), we mainly focus on molecular gas in the Cygnus Rift, and discuss the big picture of MCs in different layers and estimate

the total molecular mass. Finally, we give our summary in Section 7. More details of techniques can be seen in Appendixes A–F.

## 2. DATA

### 2.1. CO data

The MWISP (Su et al. 2019) project is an ongoing CO survey by using the PMO 13.7 m millimeter-wavelength telescope at Delingha, China. The survey observes  $^{12}\text{CO}$ ,  $^{13}\text{CO}$ , and  $\text{C}^{18}\text{O}$  simultaneously toward the northern Galactic plane. The first epoch (MWISP I) has been completed from 2011 to 2021 for the whole region of  $10^\circ \leq l \leq 230^\circ$ ,  $|b| \leq 5^\circ$ . The MWISP II is launching toward  $5^\circ \leq |b| \leq 10^\circ$ .

The PMO 13.7 m telescope uses the  $3 \times 3$  multi-beam side band-separating Superconducting Spectroscopic Array Receiver system (see details in Shan et al. 2012). Briefly, the total bandwidth of the receiver is 1 GHz with 16,384 channels, providing a frequency interval of 61 kHz and covering a velocity range of  $2700 \text{ km s}^{-1}$ . The channel separations (rms level) of the data are  $0.158 \text{ km s}^{-1}$  ( $\sim 0.48 \text{ K}$ ) for  $^{12}\text{CO}$  and  $\sim 0.166 \text{ km s}^{-1}$  ( $\sim 0.25 \text{ K}$ ) for  $^{13}\text{CO}$  and  $\text{C}^{18}\text{O}$ , respectively. With moderate spatial resolution ( $\sim 51''$ ), the three-dimensional (3D) FITS data cubes of each cell ( $30' \times 30'$ ) were made with a grid spacing of  $30''$ .

A preliminary analysis on the noise characteristics (Cai et al. 2021) has been done to increase the quality of data, including removing bad channels, decreasing edge effects, and correcting baseline distortion.

In this paper, the data cube to Cygnus is clipped in the following range:  $l$ ,  $72^\circ \sim 87^\circ$ ;  $b$ ,  $-5^\circ.1 \sim 5^\circ.1$ ;  $v$ ,  $-100 \sim 50 \text{ km s}^{-1}$ . We resampled the velocity channels of all three lines to  $0.2 \text{ km s}^{-1}$  (the corresponding rms level is  $0.42 \text{ K}$  for  $^{12}\text{CO}$ ,  $0.22 \text{ K}$  for  $^{13}\text{CO}$  and  $\text{C}^{18}\text{O}$ ) to reduce the bias in data processing. The resultant data are in  $-45 \sim 40 \text{ km s}^{-1}$ , covering the major emission of Cygnus (see Figure 1 and 2). A dataset of  $^{12}\text{CO}$  and  $^{13}\text{CO}$  used in this work are available at doi: [10.57760/sciencedb.16716](https://doi.org/10.57760/sciencedb.16716).

### 2.2. Gaia DR3

We use the photometric data and parallaxes from Gaia DR3, which was released in 2022 June 13 (Andrae et al. 2023; Creevey et al. 2023; De Angeli et al. 2023). In total, 1.8 billion objects have source classification and probabilities in DR3. Over 470 million sources have astrophysical characterizations from General Stellar Parameterizer from Photometry (GSP-Phot) results for apparent magnitude  $G \leq 19$ . In our CO coverage, 1,730,905 stars are included with a parallax over error larger than 5. The stars with very small  $A_G$  errors ( $\leq 0.01 \text{ mag}$ ; see details in Section 4.2.2) are discarded. Finally, 1,362,839 stars are used for following MC distance measurement.

Assuming a constant  $R_0 = 3.1$ , the interstellar extinction was applied to the model grid according to Fitzpatrick (1999). We take  $A_G$  from the GSP-Phot results. The reddened spectral energy distributions are integrated over Gaia  $G$  passband, and the derived magnitude can be compared to the corresponding value without extinction (Andrae et al. 2023). For estimating the geometric distances from parallaxes, we use a simple Monte Carlo sampling to inverse the parallaxes. Statistical comparisons of distances with different methods have been done by following the work of Luri et al. (2018). We find all methods give consistent results (see Appendix C for detailed analysis).

## 3. CLOUD IDENTIFICATION

MCs often display extended and irregular morphology. Some clouds show intricate hierarchical morphology, characterized by filamentary networks and clumpy structures. So how to describe or define the structure of an MC needs to be explored.

Many agglomerative clustering algorithms have been proposed and applied to construct MC samples from various CO surveys. The Dendrogram (Rice et al. 2016) is applied to CO data from CfA-Chile 1.2m survey (Dame et al. 2001). SCIMES is used in various CO lines surveys, for example,  $^{12}\text{CO}$  (1–0) from the MWISP (Ma et al. 2021),  $^{12}\text{CO}$  (3–2) from the James Clerk Maxwell Telescope CO (3–2) High-Resolution Survey (Colombo et al. 2019), and  $^{13}\text{CO}$  (2–1) from the SEDIGISM (Duarte-Cabral et al. 2021). Recently, Yan et al. (2021b) provided a catalog of MCs based on DBSCAN and  $^{12}\text{CO}$  data in the MWISP.

Different from the above methods, Miville-Deschênes et al. (2017) used a hierarchical cluster identification method to extract MC samples based on Gaussian decomposition. Hacar et al. (2013) characterized  $\text{C}^{18}\text{O}$  velocity coherent components in PPV space by using the friends in velocity algorithm. And Henshaw et al. (2019) used agglomerative clustering to organize nested structures (ACORNS). Due to the complicated velocity structures in Cygnus, we adopt the ACORNS algorithm based on Gaussian decomposition, and apply it to extract MC structures based on the  $^{13}\text{CO}$  emissions from the MWISP survey (Section 3.2).

### 3.1. Gaussian decomposition

Gaussian decomposition has been widely applied to the fitting of various spectral lines, e.g., HI (Marchal et al. 2019; Panopoulou & Lenz 2020);  $^{12}\text{CO}$  (Miville-Deschênes et al. 2017);  $^{13}\text{CO}$  (Riener et al. 2020);  $\text{C}^{18}\text{O}$  (Clarke et al. 2018); HNC (Henshaw et al. 2019); OH (Petzler et al. 2021);  $\text{NH}_3$  (Sokolov et al. 2020), etc. There are several manual tools to fit the spectra, such as Pyspeckit (Ginsburg & Mirocha 2011; Ginsburg et al. 2022), ScousePy (Henshaw et al. 2019), etc. And automatic fitting methods are also developed, such as GaussPy+ (Riener et al. 2019), Amoeba (Petzler et al. 2021), and other methods (e.g., Sokolov et al. 2020).

Manual fitting methods are often applied to small data sets (Henshaw et al. 2019), especially with prior understanding of the data. However, once the amount of data becomes large, it is really a time-consuming work for manual fitting. Additionally, the fitting results might be biased because of human factors. Therefore, automatic fitting methods are better suited for large-scale data analysis, such as the MWISP survey.

In the case of sufficient computing resources, the fitting results can be quickly obtained. Then, one or more sets of fitting parameters for each pixel are obtained, such as centroid velocity  $v_{0,i}$ , full width at half-maximum ( $\text{FWHM}=\sqrt{8\log(2)}\sigma_i$ ), and peak intensity  $A_i$ . In this way, the spectral line data of each pixel can be described by several parameters, leading to a clear presentation of line intensities and spatial relations among different velocity components. For example, Henshaw et al. (2020) has obtained the velocity structure of molecular gas at different scales by fitting the centroid velocities of multiple lines, and found the fluctuation and periodicity everywhere. Without spectral fitting, such interesting results cannot be obtained from the original PPV data due to the effects of line broadening and blending velocity components.

In this work, we use GaussPy+ module proposed and improved by Riener et al. (2019) to fit and decompose the  $^{13}\text{CO}$  lines. The  $^{13}\text{CO}$  data are chosen because it is usually optically thin (e.g., Wang et al. 2023; Yuan et al. 2023) and more favorable to trace the inner structure of the MCs. Moreover, Yuan et al. (2022) shows that the  $^{13}\text{CO}$  emitting area of a large-scale cloud can cover  $\sim 30\%$  of the corresponding  $^{12}\text{CO}$  area. It indicates that  $^{13}\text{CO}$  is actually a good tracer to reveal large MCs (also see Su et al. 2020; Wang et al. 2023). In the same time,  $^{13}\text{CO}$  spectral lines are often relatively velocity separated compared to the  $^{12}\text{CO}$  line profile for different MCs. All these features can largely mitigate overfitting problems.

The study on giant MCs in Orion B (Bron et al. 2018) proves that  $J = 1-0$  lines of three isotopologues of CO are good at revealing distinct density regimes. In a data-driven approach, Gratier et al. (2021) found that the  $^{13}\text{CO}$  line from Orion B cloud is effective for the estimation of the column density in various environments, especially for translucent gas ( $2 \leq Av \leq 5$ ). For clouds traced by  $^{13}\text{CO}$  emission, its extinction is neither too large nor too small. Actually, the MWISP survey shows that  $^{13}\text{CO}$  emission can trace the molecular gas in a range of  $N_{\text{H}_2} \sim 3 \times 10^{21} \text{ cm}^{-2}$  to several  $10^{22} \text{ cm}^{-2}$  (Ma et al. 2021; Wang et al. 2023). As a result, it is helpful for the distance measurement based on MC samples identified from  $^{13}\text{CO}$  emission. Finally, different molecular structures can be well distinguished for velocity-crowded regions using  $^{13}\text{CO}$  data.

Based on our experiments, we adopt the following parameters:

1. *Signal-to-noise ratio.* We set the signal to 5 rms to skip those weak emission. The signals with a level  $\gtrsim 1.2$  K are remained.
2. *Minimum FWHM.* We set it to be at least 2 channels ( $0.4 \text{ km s}^{-1}$ ) for the MWISP data.
3. *Maximum FWHM.* We did not set this parameter before fitting.
4. *Smoothing parameter.* We take the optimal smoothing parameters (i.e.,  $\alpha_1 = 2.18$ ,  $\alpha_2 = 4.94$ , Riener et al. 2020) for the MWISP.

For each pixel at sky position, the brightness temperature  $T'_B(l, b, v)$  is described as the sum of all Gaussian components, and the total intensity  $W_{\text{CO}}(l, b)$  as a function of velocity  $v$  is in the following form:

$$T'_B(l, b, v) = \sum_{i=1}^N A_i e^{-\frac{(v - v_{0,i})^2}{2\sigma_i^2}} \quad (1)$$

and

$$W_{\text{CO}}(l, b) = \sum_i \int A_i e^{-\frac{(v - v_{0,i})^2}{2\sigma_i^2}} dv = \sqrt{2\pi} \sum_i A_i \sigma_i \quad (2)$$

where  $A_i$ ,  $v_{0,i}$  and  $\sigma_i$  are the amplitude, centroid velocity, and width of each Gaussian component, respectively.

Our data cube includes  $1801 * 1225$  (2,206,225) pixels, among which 17.5% of the pixels have been fitted by GaussPy+. According to the fitted results, we can discern some MC structures by combining the pixels with a coherent single velocity component (see Figure 2g). 79.7% of pixels have only one velocity component along the LOS in the fitted pixels. 14.1% pixels have two, and 5% pixels have three components. Only 1.2% pixels have more than three components among fitted pixels. The pixels with two components are mainly located in the boundaries of different MC structures (see Figure 2g), showing superposition between them. The pixels with multiple components ( $\geq 3$ ) are located near the Galactic disk, revealing the crowded velocities therein.

For the whole map, we apply a moment masking criteria ((1) pixels within the  $^{12}\text{CO}$  emission structure and (2) pixels with three consecutive channels larger than 3 times the noise rms) to estimate the total valid flux of the raw data. The identification of  $^{12}\text{CO}$  emission was following DBSCAN algorithm (see details in Yan et al. 2021a). The total recovered flux from Gaussian reconstruction makes up 74.3% of the flux of the raw data. And we reconstruct the integrated intensity map from the Gaussian fitting shown in Figure 2a. The distribution of other Gaussian parameters (e.g., centroid velocities, velocity dispersion, fitted components numbers, and residuals between the reconstructed map and raw image) is presented in Figure 2 c–h.

### 3.2. Clustering

As mentioned above, many MCs in the Cygnus region display hierarchical structures and nested velocity components along the LOS. And Henshaw et al. (2019) summarized that a single MC structure has the features to be coherent in both space, velocity, and velocity dispersion. In other words, MC structures separated by ACORNS are different from each other in physical properties and statistics. For the Gaussian decomposed  $^{13}\text{CO}$  data cube, ACORNS can effectively avoid line blending effects along the LOS, and successfully separate molecular gas emission toward the Cygnus region into substructures. However, the definition of MCs has been debated for decades and as indicated in some simulations (e.g., Zamora-Avilés et al. 2017; Clarke et al. 2018). We will give some discussions in Section 6.3.

We made parametric tuning on the algorithm implemented in the MWISP data. In order to avoid the influence of noise and highlight the major structure, we only focus on the structures with relatively strong emission and large angular areas. As the signal is set to 5 times the noise RMS in Section 3.1, the decomposition results are reliable for clustering. In order to further develop the hierarchy and to reduce overdecomposition, we specify the “relax” step. After manually comparing the identified cloud structure with the coherent characteristics of the raw data, a group of parameters are adopted in ACORNS here:

1. *min\_radius*. We set it to be a bit smaller than 2 pixel. It ensures that the smallest structure in the clustering result has  $\geq 9$  pixels.
2. *velo\_link*. We set it to  $0.2 \text{ km s}^{-1}$  based on resampled data.
3. *dv\_link*. The line width link parameter is set to  $0.4 \text{ km s}^{-1}$ .
4. The coefficients of the relax step are set to [3, 2, 0.5] times the cluster criteria (as default if “relax” was activated).
5. The stop criteria is set to 3.

Then, the algorithm further eliminates some small structures that are not merged into the adjacent large structures. Finally, the MC samples with coherent  $^{13}\text{CO}$  emission are constructed based on the above steps.

After adding another loop to the clustering process (details in Appendix E), 72.6% of the flux is recovered compared to the raw data. It indicates that a large proportion of flux restored by both Gaussian decomposition (Figure 2a) and clustering (Figure 2b). We find that only a small fraction of emission ( $\approx 1.7\%$ ) fails to merge into branches.

Different from the other methods (e.g. SCIMES, Dendrogram, DBSCAN, etc.), we mainly use the results of Gaussian fitting and the ACORNS clustering algorithm to produce the cloud table, so the definition of cloud boundary is different in the spatial projection and in the direction of velocity. In the plane perpendicular to the LOS, the boundary of the cloud can be determined by aggregating all pixel locations. In the forest of clusters, each tree corresponds to a cloud structure. For a tree with a hierarchical structure (with branches and leaves for large-scale structures), the cloud is a complex that is composed of discrete, nonoverlapping substructures. For a tree with no hierarchy, the cloud is a uniform and coherent structure. In either case, the positions of the outermost pixels form the boundary of the cloud

in the projection plane. In the LOS direction, the Gaussian fitted line width of each component corresponds to the “velocity thickness” of the cloud. For simplicity, we take the position of the line centroid velocity  $\pm 3\sigma_v$  (see equation (9)) as the range of cloud in the velocity direction. According to the above clustering criterion, the velocity boundary of adjacent pixels is also similar, so that the cloud in PPV space has a relatively smooth contour.

### 3.3. Check identified structures

For comparisons, we plot an average spectrum that illustrates the total emission intensity reproduced by GaussPy+ (blue line in Figure 3) as well as clouds clustering (red line in Figure 3). The total integrated intensity reconstructed by fitting components and clustering accounts for 81.5% and 79.5% of flux (black line in Figure 3), respectively, for all fitted pixels based on Gaussian decomposition (see Section 3.1). Note that the flux of all fitted pixels here is  $\sim 10\%$  smaller than the flux of the whole region.

In the Cygnus X North region, the widely studied filament DR21 with HII regions is extracted, as well as other globular structures with brightness temperatures in the vicinity (see Section 5.1). In the Cygnus X South region, a large cloud is identified with a straight clubbed body, and waterfall-like arms adjoin in its center (later on, we call it L889; see Section 5.2). The filamentary cloud L914 is divided into two segments because the centroid velocity turns sharply between the two MC structures (see Section 5.4). As a typical subregion with relatively simple velocity components, the identified cloud of L914 after clustering restores about 77% flux of the raw data in a moment masking method (larger than the average 72.6%).

### 3.4. Cloud parameters

Based on cloud identification from  $^{13}\text{CO}$  emission, there is only one single Gaussian component along the LOS in each coherent structure. For a structure with pixels number  $n_{\text{pixels}}$ , the integrated intensity of the  $j$ th component  $W_{\text{CO}}^{\text{cloud}}(l_j, b_j) = W_{\text{CO}}^j$ . Here, we define intensity-weighted coordinates of identified structures, with the following:

$$l_0 = \frac{\sum_j W_{\text{CO}}^j l_j}{\sum_j W_{\text{CO}}^j} \quad (3)$$

and

$$b_0 = \frac{\sum_j W_{\text{CO}}^j b_j}{\sum_j W_{\text{CO}}^j} \quad (4)$$

The total intensity of cloud is  $W_{\text{CO}}^{\text{cloud}} = \sum_j W_{\text{CO}}^j$ . The standard deviation along  $l$  and  $b$  is

$$\sigma_l = \sqrt{\frac{\sum_j W_{\text{CO}}^j (l_j^2 - l_0^2)}{\sum_j W_{\text{CO}}^j}} \quad (5)$$

and

$$\sigma_b = \sqrt{\frac{\sum_j W_{\text{CO}}^j (b_j^2 - b_0^2)}{\sum_j W_{\text{CO}}^j}} \quad (6)$$

The total brightness temperature of a cloud at  $v$  is provided by summing of all pixels in the identified boundary:

$$T_B^{\text{cloud}}(v) = \sum_j A_j e^{-\frac{(v - v_{0,j})^2}{2\sigma_j^2}} \quad (7)$$

We then can compute the cloud’s intensity-weighted mean velocity and velocity dispersion as

$$v_0^{\text{cloud}} = \frac{\int v T_B^{\text{cloud}}(v) dv}{W_{\text{CO}}^{\text{cloud}}} \quad (8)$$

and

$$\sigma_v = \sqrt{\frac{\int v^2 T_B^{\text{cloud}}(v) dv}{W_{\text{CO}}^{\text{cloud}}} - v_0^{\text{cloud}2}} \quad (9)$$

The angular size of a given cloud is straightforward, which is described in units of square arcminutes:

$$S_{\text{ang}} = n_{\text{pixels}} \delta l \delta b \quad (10)$$

and angular radius

$$R_{\text{ang}} = \sqrt{\frac{S_{\text{ang}}}{\pi}} \quad (11)$$

where  $\delta l$ ,  $\delta b$  is the grid size of data cube, respectively. The peak intensity of the cloud  $T_{\text{peak}}$  is the maximum of derived amplitudes:

$$T_{\text{peak}}(^{13}\text{CO}) = \max\{A_1, A_2, \dots, A_j, \dots\} \quad (12)$$

The column density of MCs here can be estimated by the abundance of  $^{13}\text{CO}$  emission as well as the  $\text{H}_2$ - $^{12}\text{CO}$  conversion factor. The first method uses a radiative transfer model under the local thermodynamic equilibrium (LTE) condition, assuming an equal excitation temperature for  $^{12}\text{CO}$  and  $^{13}\text{CO}$  lines, while the second method gives a direct relation between the line intensity and the  $\text{H}_2$  column density. For the identified  $^{13}\text{CO}$  MC structures, assuming the emission is optically thin, the temperature of the cosmic microwave background radiation  $T_{\text{bg}} \approx 2.7$  K. The summed column density of a given cloud can be described as follows (Bourke et al. 1997; Wilson et al. 2009):

$$N_{\text{tot}} = C \times 2.42 \times 10^{14} \frac{\tau(^{13}\text{CO})}{1 - e^{-\tau(^{13}\text{CO})}} \times \frac{1 + 0.88T_{\text{ex}}}{1 - e^{-5.29/T_{\text{ex}}}} W_{^{13}\text{CO}}^{\text{cloud}} \quad (13)$$

Here,  $C$  is a ratio between the abundance of  $\text{H}_2$  and  $^{13}\text{CO}$ . We adopt  $8 \times 10^5$ , from the empirical abundance ratio  $[\text{H}_2/^{12}\text{CO}] = 1.1 \times 10^4$  in Frerking et al. (1982) and  $^{12}\text{C}/^{13}\text{C}$  relation from Milam et al. (2005).  $\tau(^{13}\text{CO})$  is the optical depth at the peak intensity  $T_{\text{peak}}$ , which is calculated by the excitation temperature  $T_{\text{ex}}$ . The values of  $T_{\text{ex}}$  and  $\tau_{13}$  can be written as follows (see also Nagahama et al. 1998; Pineda et al. 2010; Li et al. 2018):

$$T_{\text{ex}} = \frac{5.53}{\ln\{1 + 5.53/[T_{\text{peak}}(^{12}\text{CO}) + 0.819]\}} \quad (14)$$

and

$$\tau_{13} = -\ln\left\{1 - \frac{T_{\text{peak}}}{5.29 [1/(e^{5.29/T_{\text{ex}}} - 1) - 0.164]}\right\} \quad (15)$$

Finally, the average column density of each  $^{13}\text{CO}$  cloud is

$$N_{\text{mean}} = \frac{N_{\text{tot}}}{n_{\text{pixels}}} \quad (16)$$

#### 4. DISTANCES AND PROPERTIES OF MCS

In the background eliminated extinction–parallax method (i.e., BEEP; Yan et al. 2019a), the unrelated extinction was removed to calculate distances of MCs by calibrating the stellar extinction toward MCs with the extinction of stars around them. The jump point in the  $A_G$ –*Distance* map is detected using Markov Chain Monte Carlo (MCMC) method by a Bayesian modeling approach. There are five key parameters in the distance measurement: the location of the jump point (*Distance*), the extinction value of the foreground and background stars ( $\mu_1$  and  $\mu_2$ ), and the dispersion of the foreground and background extinctions ( $\sigma_1$  and  $\sigma_2$ ). A Gaussian distribution is used as the likelihood function of  $A_G$  distribution. We set the jump points in 100–3000 pc with a uniform distribution, considering the limitation of Gaia’s precision. The initial distance is set to the average value of the selected stars. The initial values and errors’ transformation of other parameters follow Yan et al. (2019b).

We choose *emcee* (Foreman-Mackey et al. 2013), the affine-invariant ensemble sampler for our model, instead of *Pymc3* and Gibbs samplings (Yan et al. 2019b). We also test the difference between *emcee* and *Pymc3* (Salvatier et al. 2016) for MCMC sampling (see details in Appendix B). *emcee* has better performance.

##### 4.1. Selection of star samples

Yan et al. (2019a) showed that the BEEP method is suitable for distance estimations of MCs at low Galactic latitudes. However, cloud identification in their procedures could introduce significant uncertainties for clouds in

velocity crowding regions, especially in the first quadrant. As discussed in Section 3, the cloud boundary in the projection toward Cygnus region cannot be well delineated by direct clustering (e.g., Dendrogram, DBSCAN, etc.) in PPV space. The identified structures might include emission from other clouds due to the overlap between neighboring structures in PPV space. The extent of both on-cloud and off-cloud stars is thus not well demarcated by the signal levels (Yan et al. 2019a) or identified boundaries (Yan et al. 2021a). As a result, the influence of other structures along the LOS could lead to an inaccurate distance measurement with a deviation of the jump point. We follow the procedures of BEEP, but with a different cloud identification method. Some improvements are made to solve the puzzles in the velocity crowding regions (see details in Section 4.1.2).

#### 4.1.1. Selection of on-cloud stars

After clustering based on Gaussian decomposition (see Section 3.2), we obtain coherent MC structures with exact boundaries from  $^{13}\text{CO}$  emission. As seen in the work of Yan et al. (2019b), the number of star samples within the cloud helps to improve the precision of the distance measurements. We thus include all stars inside the cloud boundary (see red and black area in Figure 4).

A further validation of the reliability of the selection is to consider those stars in the overlapping part (black region in Figure 4). We propose that stars in the overlapping area have more of a contribution to the distance measurement than introduced uncertainties. This was also confirmed in a series of tests (see Appendix B), where we used all the on-cloud stars and another set of stars with the removal of the overlapping region. We found that most distances show good coincidence between the two scenarios. While the results from selecting all the source stars show smaller errors and more stable sampling.

#### 4.1.2. Selection of field stars

It is also crucial to construct samples of field stars for accurate distance measurement. That is, the selection of suitable field stars can be used for background elimination to highlight the jump caused by the target MC (Yan et al. 2019a). It is difficult to find a clean reference region near the Galactic disk. Generally, to determine the jump point of  $A_G$ -Distance map after background elimination, the extinction of field stars should be rather smaller than that of on-cloud stars, and the displacement from on-cloud stars should be close enough. That is so that reference stars can be fitted as an extinction background (hereafter “background extinction” means the unrelated extinction toward MCs) for on-source stars and the  $A_G$  jump of the cloud structure can reach a threshold to be detected. Obviously, the above two conditions need to be balanced. So we designed Models A and B (see Figure 4) to measure the distance of MCs.

*Model A.* To highlight the jump features in the  $A_G$ -Distance map, we use the region of  $^{12}\text{CO}$  emission free ( $^{12}\text{CO}$  integrated intensity  $\leq 1 \text{ K km s}^{-1}$ ) as the reference region (see orange region in Figure 4a). The outer boundary of the reference region (black dashed contour in Figure 4) is limited to within  $30'$  from the MC. Obviously, here, we considered the complicated features of MCs in the velocity crowding region based on  $^{12}\text{CO}$  and  $^{13}\text{CO}$ . This is due to the fact that MCs with multiple velocity components are filled with  $^{12}\text{CO}$  emission with which they can contribute nonnegligible extinction. On the other hand, enough field stars are needed for the accurate distance measurement.

This scheme allows more  $^{13}\text{CO}$  MCs to do background elimination in complex regions. After correcting the field stars' effects, the distance of the cloud can be clearly identified (see examples in Figure 5a). 185 clouds (see Table 1) out of 300 large-size clouds (angular sizes  $\geq 60 \text{ armin}^2$ ) are measured by Model A.

*Model B.* Another scheme is more straightforward. We choose a ring-like area outside the  $^{13}\text{CO}$  emission as the reference region. An empirical offset helps reveal the jump point. The inner and outer boundaries of the ring-like structure are  $2.5'$  and  $7.5'$  away from  $^{13}\text{CO}$  emission, respectively. We do not exclude field stars located within the  $^{12}\text{CO}$  emission in the ring-like area (see Figures 5b and 6b). The number of field stars is then sufficient to capture the extinction characteristics of the background. The distance measurements from Model B are probably more reliable for some special cases (see Appendix D).

Nevertheless, Model B demands that the target MC should have a higher column density than its surroundings. In other words, Model B only works when CO-dark extended gas has a small influence on the distance measurement. Otherwise, after subtracting the background extinction, the jump value is too small to be detected. Generally, the results from Model B may be less accurate than those from Model A (see simulations in Appendix B).

In total, the distances of 120 MC structures from Model B are roughly consistent with those from Model A (see Table 1 and Figure 7). Additionally, another 22 clouds are successfully measured by Model B, which are not measured by Model A.

#### 4.1.3. *On-cloud stars only*

As a comparison, we also measured a group of results without background elimination (see blue squares in Figure 7). To reduce the contamination from different components along the same LOS, we remove the on-source stars in the overlapped region (from ACORNS). Since the background extinction is not subtracted, the distance measurements will be affected by other structures (traced by  $^{12}\text{CO}$  emission) as well as the accumulated extinction along the LOS. So the obtained distances tend to jump to the position corresponding to the maximal  $\Delta A_G$  (i.e.,  $\mu_2 - \mu_1$ ), or to the average of multiple components. As a result, this scheme gives more distances to the MC samples, but the measurements are not accurate enough for the identified MC structures in the Galactic plane (Zucker et al. 2019; Sun et al. 2021a; Guo et al. 2022).

### 4.2. *Uncertainties*

#### 4.2.1. *Uncertainty from our model*

Two effects have a decisive influence on distance measurements of clouds. One comes from the nested clustering algorithm. Considering the complex cloud structures, the criteria settings (see details in Section 3.2) can only extract the physical structure to some extent. On the other hand, a physical structure might be divided into different parts due to velocity gradients, variations of line widths, and nonuniform intensities. This effect can be retrieved by accurate distance measurement for overdecomposed complexes in the procedure.

Another effect comes from the complicated extinction of the interstellar medium (ISM) environment. As discussed in Section 3.1,  $^{12}\text{CO}$  emission can trace more extended MC structure of the translucent molecular gas than  $^{13}\text{CO}$  emission. Even though we have already considered the extinction effect of  $^{12}\text{CO}$  gas in the Model A, the atomic gas and CO-dark gas are likely more space filled in the surrounding region. For the  $^{13}\text{CO}$  free region, the envelope of the cloud might still contribute to the considerable extinction. We have to carefully deal with the influence from neighboring gas in complicated environment. The separation of the different extinction environments cannot be thoroughly removed due to the multiphase gas structure in the ISM. Therefore, it is much more difficult to choose on-cloud and off-cloud regions traced by  $^{13}\text{CO}$  emission in the complicated extinction environment. Nevertheless, our methods (Models A and B) should be better than detecting extinction jumps directly by considering the MCs' morphology of  $^{13}\text{CO}$  (see Section 3.2) and background elimination (see Section 4.1.2).

How do we check whether identified MC structures in the clustering are from a physical cloud? For some large-scale structures, we can measure the different subregions to explore the possible connection between them. In Appendix A, some subregions (boxes or contours in Figures A1 and A2) are chosen to do distance measurements. We find that most of them are at similar distances (see lower left panel in Figures A1 and A2). The ambiguities from neighboring clouds cannot be totally removed, especially for small structures overlapping with adjacent extensive structures.

Besides the 5%~10% system uncertainties within 3 kpc from Gaia data, the sampling process itself also introduces measurement dispersion. As mentioned above, many effects can cause uncertainties of distance measurements, e.g., fewer on-cloud stars, smaller  $\Delta A_G$  of background eliminated extinction, and multiple jumps along a certain LOS. We first remove the clouds with a large dispersion of distance caused by the lacking of on-cloud stars ( $\leq 20$ ). Then, some clouds have a small difference between both sides of the jump point (i.e.,  $\Delta A_G$  smaller than 0.2 mag). As for the detection of multiple jumps, this problem will be further discussed in a future paper. In this paper, combining the results of Model A and B can largely reduce this problem.

For some large-scale MC structures, their distances are not detected by either Model A or B. It could be due to the severe extinction environment in front of them. The reddening from dust might be more extensive or saturated by Gaia's observation limit for the foreground dark clouds.

In our model, we assume that the cloud is a simple screen perpendicular to our sight lines. We thus ignore the clouds' thickness and possible inclination to us. Among MCs with a measured distance, some display an abnormal feature near the jump point (e.g., the ascending slope in  $A_G$ -Distance map). In particular, for some large-scale MC structures with a large number of stars (e.g. L889 in the upper right panel in Figure A2), it might suggest a continuous medium or cloud inclination along the LOS. These effects can cause the deviations of the jumps we determined.

#### 4.2.2. *Uncertainty from baseline elimination*

The statistical distributions of stars in the foreground and/or background of the cloud follow a Gaussian distribution. In some of LOS, we found that the distribution of  $A_G$  is Gaussian with an increasing baseline near the jump point.

The reddening of stars increases with a gentle slope when the distance increases. Note that the off-cloud region is not extinction free. We just identify the jump point of this cloud when the jump is much steeper to the off-cloud region.

Based on the monotonic fitting method (Kruskal 1964; de Leeuw 1977) and using a module called scikit-learn in Python, we performed the isotonic regression to fit the baseline of background extinction weighted by the inverse-variance of  $A_G$  (Yan et al. 2019a). The stars with high weights (standard deviations  $\leq 0.01$  mag) are removed in this work. As the uncertainty of extinction in the  $G$  band of Gaia is not a direct measurement, the posterior distribution of  $A_G$  with very small values could be unphysical. On the other hand, the high weights of individual sources might introduce deviations of fitting, especially for the monotonic fitting to the off-cloud stars (Yan et al. 2019a). Nevertheless, the scarcity of stars and the large dispersion of  $A_G$  in the far end cause a large bias to our results. We found that  $\Delta A_G \geq 0.2$  mag can mitigate the problems.

$A_G$  is derived from  $A_0$  in the Fitzpatrick extinction law (Fitzpatrick 1999) and absolute  $M_G$  magnitude from isochrones (Andrae et al. 2023). The median value of uncertainties of  $A_G$  and  $A_0$  is around  $0.06 \sim 0.07$  mag, considering the inflation effect. Although Gaia collaboration did not apply corrections for GSP-Phot uncertainties, we use the inflated value for safety, i.e. the lower limit  $\Delta A_G = 0.2$  mag ( $3\sigma$  confidence level) for identifying extinction jumps. For Model B, the larger  $A_G$  values in the reference region make a smaller  $\Delta A_G$  after background elimination, we thus set  $\Delta A_G = 0.15$  mag ( $2\sigma$ ). Considering the fluctuations of  $A_G$  from random errors, biases from monotonically increasing fit, and the variations of stars'  $A_G$  dispersion with increased distance, the larger  $\Delta A_G$  from MC structures helps to reduce false detection.

Figure 7 shows the distance results of  $^{13}\text{CO}$  structures (see Sections 4.1.2 and 4.1.3). For most MC samples, the distance measurements match well in Models A and B. We check all the samples and confirm the jump points presented by Models A and B are the same one.

We find 75% of samples from Model A have a slightly smaller distance compared to those from Model B. We adopt the result from Model A in the following analysis because of the more clear jump in Model A (see example in Figure 5). The differences come from a sampling process due to different  $\Delta A_G$  for on-cloud stars after a different background elimination (see simulations in Appendix B).

There are two exceptions, G076.74–0.43 (ID 30 in Table 1 and Figure 6) and G084.70+0.44 (ID 181 in Table 1). For cloud G076.74–0.43, the distance difference from Models A and B is larger than 200 pc. In fact, we find two extinction layers toward the direction (see details in Section 5.2). When reference stars are chosen farther away from the target cloud (e.g., Model A), the measured distance tends to be affected by other structures along LOS. In Figure 6a, after the baseline elimination, extinctions of on-cloud stars fluctuate along the  $A_G$ -Distance map, indicating the inconsistency of  $A_G$ -Distance relation between on-cloud and off-cloud stars. So the baseline subtracted data from Model A might suffer from fluctuations in the sampling result. And the distance of the cloud should be  $1041_{-68}^{+67}$  pc from Model B. Similar to cloud G076.74–0.43, the distance difference of G084.70+0.44 from Models A and B is 137 pc, but Model B has a better background elimination, and presents a smaller sampling uncertainty.

For more special cases with complex background extinction, Model A is invalid because of insufficient field stars in the nearby region. Model B provides distance measurements for another 22 MC structures (see Appendix D). Among these cases, some structures likely suffer from severe contamination from neighboring clouds.

### 4.3. Molecular cloud parameters

We summarize the parameters of 207 clouds with distances in Table 1. 120 clouds are measured by both Models A and B (class I). Their distances are used in Figures 7 to 16. 22 clouds are only measured by Model B (class II), and over 60 clouds are alone measured by Model A (class III). Generally, the dust-based distances to specific MCs might introduce  $\approx 5\%$  uncertainties out to at least 2 kpc from Gaia data (see the recent review from Zucker et al. 2023). In all the following discussions, we added a 5% system uncertainty to the MC distances.

In the left panel of Figure 7, we plot the distance distribution of the 120 class I clouds. There is a gradient from east to west for the molecular gas traced by  $^{13}\text{CO}$  emission within 1 kpc. For example, the clouds near NAP are located at  $759 \pm 57$  pc, while the western clouds near L889 are systematically larger than 800 pc. In Cygnus X South region, we also find a middle gas layer in  $\sim 1.3$  kpc.

Because of the “extinction wall” effect (Straizys et al. 1993), we fail to obtain the distance of some clouds in the Cygnus X SFR, including DR21, DR20, and the clouds behind L889 (see details in Section 5.1–5.2). After removing the foreground clouds, the distance of the rest of clouds can be determined based on the spatial coincidence between

the  $^{13}\text{CO}$  structures and the corresponding masers/photodissociation (PDR) interfaces (see details in Cygnus North Filament from  $^{13}\text{CO}$  in Section 5.1 and PDR interfaces traced by intense infrared emission in Section 5.2).

Once the distances of clouds are determined, we can derive the physical parameters of these MCs, such as effective radius, mass, and surface density. Physical radius can be calculated from the angular size  $R_{\text{ang}}$  and cloud distance  $d$ :

$$R = d \tan(R_{\text{ang}}) \quad (17)$$

Then, the mass and surface density of  $^{13}\text{CO}$  clouds can be estimated by

$$M = N_{\text{tot}} d^2 \Omega \mu m_{\text{H}} \quad (18)$$

where  $\Omega$  is the solid angle of each pixel;  $\mu = 2.8$  is the atomic weight of molecular hydrogen. And the surface densities of cloud structures is

$$\Sigma_{\text{cloud}} = \frac{M}{\pi R^2} \quad (19)$$

We compute the virial parameter to characterize the dynamical state of clouds or cores; the virial mass is in the form

$$M_{\text{vir}} = 5 \frac{R \sigma_v^2}{G} \quad (20)$$

where  $G$  is the gravitational constant;  $\sigma_v$  is the velocity dispersion of each cloud, which is provided in equation (9), assuming the  $^{13}\text{CO}$  cloud has a uniform density profile, and the virial parameter can be described as

$$\alpha_{\text{vir}} = \frac{5 \sigma_v^2 R}{GM} \quad (21)$$

The cloud distance perpendicular to the Galactic disk is directly described by

$$z = d \sin(b_0) \quad (22)$$

## 5. SUBREGIONS TOWARD CYGNUS

### 5.1. *Cyg-North region*

Based on the measured distances of MCs, we find at least two layers of gas emission in the foreground toward the Cygnus X North region (see Figures 8–10). One is at  $\sim 800$  pc and another is at  $\sim 1$  kpc. Combining the other information (see below), many  $^{13}\text{CO}$  structures are located in more distant regions.

*800 pc gas layer.* The velocities of molecular gas in this layer are mainly concentrated in 1–7 km s $^{-1}$  (see contours in Figure 8b and orange dots in Figure 9), including the filament L914 (see Section 5.4 and Figure 15). In the region of  $l = [82^\circ, 84^\circ]$  and  $b = [1.5^\circ, 2.5^\circ]$ , some MCs are at higher velocities intervals ( $8 \leq v \leq 13$  km s $^{-1}$ ). Including those NAP clouds in the velocity interval of  $[-6, 6]$  km s $^{-1}$  (Section 5.3), we find that a large molecular gas loop is located at  $\sim 800$  pc (see below in Figures 8 and 17).

*1 kpc gas layer.* In Figure 8a–c, we find a gas layer at  $\sim 1$  kpc. MCs in this layer have a large velocity extent from  $-4$  to  $14$  km s $^{-1}$  (black dots in Figure 9), inferring a large velocity dispersion between clouds. We identify them as an MC complex from  $(l = 81^\circ, b = 0.8^\circ)$  to  $(l = 79^\circ, b = -1.8^\circ)$ . We note that the “twins cluster” structures are located in this layer (marked as clusters a and b in Figures 9 and 10b, also see IDs 123 and 113 in Table 1). The two clusters’ distances are  $962_{-67}^{+64}$  pc and  $1024_{-73}^{+77}$  pc, respectively. We note that the two structures have almost the same physical properties but very different velocities. Both of them also have higher bright temperature than other clouds in the 800 pc and 1 kpc gas layer. What causes the twin clouds’ velocity to differ by 15 km s $^{-1}$  is still unknown. Further studies would be interesting to find out the kinematic origin of them.

*Background layer for more distant gas at  $\sim 1.5$  kpc.* The distances of many MC structures with intense  $^{13}\text{CO}$  emission have failed to be determined because of the large extinction from the above two layers. We attribute these filamentary structures with fluctuated velocities from  $-9$  to  $1$  km s $^{-1}$  (see Figure 8a) as the Cygnus North Filament. The Cygnus North Filament is very prominent in the north of Cygnus OB2. DR21(OH), DR21, DR23, DR22 are all located along the dense CO filament. The filament can be divided into different substructures in a clustering result due to velocity gradient (see Figure 8d). DR21 and DR21(OH) at  $\sim -3$  km s $^{-1}$  are on the most bright DR21 filament (see the intensive C $^{18}\text{O}$  emission in gray scale of Figure 8a). The distance of the Cygnus North Filament is estimated

to be 1.5 kpc by a methanol maser measurement from DR21 and DR20 (Rygl et al. 2012). We also find that some dense molecular gas with slightly high velocities are different from MCs at 800 and 1 kpc layers. For example, the MC associated with W 75N (see m11 in Table 2) is overlapped with DR21 filament, but at a nearer distance of 1.3 kpc (Rygl et al. 2012).

Furthermore, we also find several corresponding structures between  $^{13}\text{CO}$  emission and bright infrared features (see Figure 8e). Among them, the two globules (see Schneider et al. 2006, 2016) and DR17 with large velocities (from 7 to 20  $\text{km s}^{-1}$ ) are probably associated with nearby star-forming regions (e.g., Cygnus OB2). We assume these MCs, together with clouds on the Cygnus North Filament, range from 1.3 to 1.7 kpc based on the association between MCs and masers or OB stars (Rygl et al. 2012; Quintana & Wright 2021). Tentatively, we put them together as a background layer with an averaged distance at  $\sim 1.5$  kpc.

In Figure 9 we plot the  $^{13}\text{CO}$  bright temperature, velocity dispersion, and column density of MCs in different gas layers. The bright temperature and column density of the molecular gas at  $\sim 1.5$  kpc are obviously larger than those for the gas in 800 pc and 1 kpc gas layers.

The 3D illustration in Figure 10 denotes the distribution of three layers toward the Cygnus X North region. Again, the extended molecular gas in the 800 pc and 1 kpc layers is overlapped in front of the  $\sim 1.5$  kpc MCs, leading to the failure of distance measurements of these MCs at larger distances based on our models.

## 5.2. Cyg-South region

The molecular gas in  $\sim 4^\circ \times 4^\circ$  region of Cygnus X South is divided into three velocity intervals: the mid-interval ( $-3 \sim 3 \text{ km s}^{-1}$ ), minus interval ( $-10 \sim -3 \text{ km s}^{-1}$ ), and positive interval ( $3 \sim 12 \text{ km s}^{-1}$ ) based on our clouds' identification. These results can be compared with the work from Schneider et al. (2006). We also identified at least three gas layers toward this direction.

*950 pc gas layer.* In Figure 11a, we found that a bulk of molecular gas are at a distance of  $\sim 950$  pc (e.g. the prominent emission from giant molecular complex L889). The mean bright temperature of the clouds in this layer is low, which is different from the gas associated with the star-forming regions (see the background layer below). From Figures 11 and 12, most clouds in the Cygnus X South region are near  $0 \text{ km s}^{-1}$ , which causes great difficulty to distinguish them. The clouds in  $\sim 950$  pc layer are distributed in all velocity intervals. Figure 11f shows agreement between our result and the 3D dust maps by Green et al. (2019). As the largest  $^{13}\text{CO}$  structure in Table 1 (ID 57 for L889), we will further discuss it in Appendix A.

*1.3 kpc gas layer.* We also identify a group of clouds with larger distances, which construct a layer of molecular gas at  $\sim 1.3$  kpc toward the Cygnus X South. The velocities of these clouds are distributed in  $[-12, 12] \text{ km s}^{-1}$ . The spatial distribution of these 1.3 kpc clouds with smaller sizes are relatively discrete from those in the 950 pc gas layer. Because of the great extinction caused by the 950 pc layer, the clouds with measured distances in the 1.3 kpc layer are mainly found in the region with weak CO emission from L889 structure (see Figure 11ac).

Interestingly, we find a cloud (see cloud 94 in Table 1) is located at  $1271_{-115}^{+116}$  pc, which agrees well with the maser G079.73+0.99 at 1.36 kpc (Rygl et al. 2012). Another cloud associated with HII region DR7 (see cloud 86 in Table 1) is at  $1247_{-100}^{+113}$  pc based on our models.

For the DR13 cloud (see cloud 48 in Table 1) with bright CO and infrared emission, its distance by Model B is also at  $\sim 1.3$  kpc. Next to DR13, the cloud G077.9–1.1 with bright CO emission (see cloud 44 in Table 1) matches the IR dark area very well (see Figure 11 a and e). Our distance measurement confirms it is at  $1215_{-87}^{+90}$  pc. We suppose that cloud G077.9–1.1 is slightly in front of DR13 cloud, leading to the matched morphology between the molecular gas structure and IR dark area. These results demonstrate the accuracy and effectiveness of our methods.

*Background layer for more distant gas associated with PDR interfaces.* For the clouds farther away than  $\gtrsim 1.4$  kpc toward the Cygnus X South region, only two MCs can be determined by Model B (IDs 19 and 67 in Table 1). However, at least tens of dense CO clouds with cometary, oval-shaped, and irregular structures coincide well with bright  $8\mu\text{m}$  emission. We also find good agreement in physical properties of these clouds (e.g.,  $^{13}\text{CO}$  peak temperature and column density; see blue dots in Figure 12).

We note that the cometary clouds (see Table 3) show a head-to-tail morphology pointing away from the Cygnus OB2, indicating the interaction between the molecular gas and intense UV radiation or stellar wind from nearby OB stars. These results are similar to those from Schneider et al. (2007). One of those cometary clouds (see m7 in Table 2 and p11 in Table 3; also named globules in Schneider et al. 2006, 2016) is exactly located at 1.61 kpc based on maser

measurement of G079.87+01.17 (see IRAS 20286+4105 in Xu et al. 2013). The coincidence of molecular gas and IRAS 20286+4105 demonstrates the above picture.

For these cometary clouds, clouds A and B identified by Schneider et al. (2006) correspond to our cases p1 and p3 (see Table 3). From our clouds' identification, we find another cloud C (p5 in Table 3) is next to cloud B (see Figure 11 a and e). The high temperatures of the three clouds in the Cygnus X South region, as well as the high column densities, are different from clouds in 950 pc and 1.3 kpc gas layers (see Figure 12). We suggest that all of them are probably shaped by nearby Cygnus OB2 and subgroups of OB1 associations.

Besides the cometary clouds, the spatial morphology of some oval-shaped clouds also coincide with the structure of HII regions (e.g. DR 6, DR 9 identified by Downes & Rinehart 1966), indicating the physical association between them. For these oval-shaped clouds, we do not have enough evidences to associate them with a large-scale radiation field; thus, their distances cannot be confirmed. Here, we temporarily put the oval-shaped and irregular MCs in the background layer (see hollow circles in Figure 12).

We conclude that L889 and the nearby clouds in 950 pc layer contain the majority of molecular gas with low peak temperature and column density. Toward the Cygnus X South region, parts of MCs in the 1.3 kpc layer are associated with the nearer HII regions and star-forming regions (e.g., DR 13). We propose MCs associated with W75 N in the Cygnus X North also belong to the 1.3 kpc layer. The clouds embedded in the Cygnus X South SFR are mainly in a narrow velocity interval  $\lesssim 3 \text{ km s}^{-1}$ , mixing up with 950 pc and 1.3 kpc gas layers. It is different from velocity distributions in the Cygnus X North region (see Figure 9). These clouds with high column densities and temperatures are being affected by stellar feedbacks from massive OB associations.

### 5.3. North America/Pelican (NAP) region

Our identified clouds in NAP have multiple velocity components from  $-6$  to  $6 \text{ km s}^{-1}$  (see Figure 13b), which is also shown by Kuhn et al. (2020) using the moment 1 map from FCRAO  $^{13}\text{CO}$ . We also present  $\text{C}^{18}\text{O}$  emission in this area (gray scale in Figure 13a).

In Figure 14a, we plot the measured distances of different trees from ACORNS of the NAP (see cloud IDs 169  $\sim$  195 in Table 1). We find that the MC complex is located at about  $759 \pm 57 \text{ pc}$ , which is roughly consistent with previous studies based on Gaia EDR3 YSO samples in the NAP region ( $\sim 785 \text{ pc}$  in Kuhn & Hillenbrand 2020). The group E (l  $\sim 84.^\circ 8$ , b  $\sim -1.^\circ 2$ ) identified by Kuhn et al. (2020) has a distance of  $\sim 746 \text{ pc}$ , which is slightly smaller than their average distance of  $\sim 785 \text{ pc}$  for the complex. We note that at least three cloud structures (IDs 173, 190, and 193 in Table 1) are located at  $\sim 740 \text{ pc}$  toward the Group E. Figure 14b presents a system deviation of distance measurements between our results and Zucker et al. (2020). We propose that the differences come from the upgrade of both  $A_G$  and parallaxes from DR2 to DR3 (systematic uncertainty), and different details between two models: (1) an on-cloud stars' selection based on different cloud decomposition to the stratified gas structure, and (2) a model with vs. without background elimination. Moreover,  $A_G$  uncertainty is likely to be different along different LOS. For example, our distance measurements toward the Cygnus X region have no prominent systematic deviation compared with those of Zucker et al. (2020). We suggest that the NAP complex in the "800 pc gas layer" (see Section 5.1) is part of the Cygnus Rift.

### 5.4. L914 filament

L914 (see cloud IDs 139 and 161 in Table 1) is a filamentary dark cloud connecting the NAP region and the Cygnus X North region. The filament with a large velocity gradient along the spine has a rather small intrinsic velocity dispersion (see Figure 15b). Bright  $\text{C}^{18}\text{O}$  emission also presents a filamentary structure from right to left (hereafter head to tail). We find that the main structure (head, ID 139 in Table 1) has a distance of  $787_{-44}^{+45} \text{ pc}$ . Obviously, L914 and NAP clouds belong to the 800 pc gas layer of the Cygnus X North region. We also note that the substructure in the tail of L914 (ID 161 in Table 1) is located at a smaller distance of  $723_{-47}^{+51} \text{ pc}$ . Considering the spatially continuous distribution of the molecular gas (especially for the coherent filamentary structure traced by  $\text{C}^{18}\text{O}$  in Figure 15a), we propose that they belong to a single structure at  $\sim 770 \text{ pc}$ . There are also some interesting striations (Goldsmith et al. 2008) perpendicular to the spine of L914 (see details in Sun et al. 2024).

### 5.5. S106

S106 is a well-known HII region in the Cygnus X South. The dense cloud G076.33–0.74 (hereafter S106 cloud; see contours in Figure 16) is considered to be shaped by nearby OB associations (e.g., see NGC 6913 discussed by

Schneider et al. 2007). Besides, the new results show that the OB stars of Group C identified by Quintana & Wright (2021) could be the source shaping S106 cloud.

Although the distance measurement to the S106 cloud failed for both Models A and B, we suspect the cloud is located at least 1 kpc away. The 800 pc gas layer (see ID 28 in Table 1) extends to the S106 region, which could be why previous measurement to S106 have a closer distance (e.g., 600 pc in Staude et al. 1982). Actually, one nearby cloud (see cloud ID 30 in Table 1; see Section 5.2) in the 950 pc gas layer is also overlapped with the S106 cloud. The heavy extinction effect of these clouds leads to the failure of distance measurement for the cloud.

The maser G076.38–0.61 (see m3 in Table 2) is located in S106 region at 1.3 kpc (Xu et al. 2013), suggesting molecular gas at 1.3 kpc layer in this direction. In addition to the S106 cloud, we also identify another cloud structure G076.39–0.66 (see red dots in Figure 16) is superposed with the maser. This structure (see m3 in Table 2) is presented as another velocity component, which spatially coincides with the maser G076.38–0.61. Similar to the S106 cloud, MC G076.39–0.66 has high peak temperature and intense  $^{13}\text{CO}$  emission. Both structures could be the HMSFR where the maser located in, indicating the S106 cloud probably at the 1.3 kpc gas layer. However, the cometary morphology traced by  $^{13}\text{CO}$  and infrared emission for the S106 cloud might be shaped by the nearby OB associations. Thus, other opinions suggest the distance to S106 cloud is at  $\sim 1.7$  kpc (Quintana & Wright 2021), while the maser G076.38–0.61 might be associated with G076.39–0.66 at 1.3 kpc.

Interestingly, we find that a cloud G075.79+0.42 (see cloud ID 24 in Table 1) is adjacent to the S106 cloud in the projection. The cloud is at  $\sim 800$  pc from Model A. In addition, another component at 1.7 kpc can be discerned in a new multijump model (in preparation), indicating the possible gas layer in there. It shows that, toward the region, there are complicated gas distributions at different distances. We will study the multijump features of molecular gas in a forthcoming paper. In Table 2, we temporarily associate maser G076.38–0.61 with MC G076.39–0.66 (m3 in Table 2).

### 5.6. Other interesting regions

*Cygnus-NW.* The dark cloud complex L897 is located in the Cygnus Northwest (Cygnus-NW, see Figure 1). The clouds associated with it have velocities ranging from  $\sim 5$  to  $10 \text{ km s}^{-1}$ . Four of them (IDs 97, 99, 102, and 104 in Table 1) have been measured at a uniform distance (UD) of  $\sim 1$  kpc, reflecting the 1 kpc gas layer therein. We also note two structures (IDs 99 and 104 in Table 1) have very small virial parameters ( $\lesssim 1$ ). Combined with the good agreement with the overdensity of YSOCs toward the Cygnus-NW clouds within 1 kpc (see Appendix F), we infer that these MCs are gravity bounded and that the dark cloud is physically associated with the ongoing star-forming region.

*Cygnus OB3 and OB8.* Cygnus OB3 and OB8 are located at  $\sim 1895$  pc and  $\sim 1726$  pc, respectively (Quintana & Wright 2021).

Toward the Cygnus OB3, we identified a massive  $^{13}\text{CO}$  cloud (ID 1 in Table 1) at  $\sim 1.8$  kpc, which agrees with the median distance of the OB association. And several small clouds (see IDs 3 and 5 in Table 1) toward this direction are at  $\sim 1$  kpc.

Toward the Cygnus OB8, we find an interesting  $^{13}\text{CO}$  cloud G078.12+3.63 that is associated with a maser G078.12+03.63 at a distance of  $\sim 1.55$  kpc (Reid et al. 2019). The median distance of Cygnus OB8 from EDR3 (Quintana & Wright 2021) is a bit farther than the maser’s distance. However, considering the distance uncertainty, they are probably at the same place. Based on our models, another two MCs (IDs 33 and 35 in Table 1) are located in  $\sim 1.2$  kpc in this direction, indicating that the extended 1.3 kpc gas layer extends in front of the OB8 association (see Figure 17).

*Other clouds associated with masers.* Two masers G074.03–1.71 and G080.80–1.92 (see m1 and m8 in Table 2) are located at about 1.6 kpc (Zhang et al. 2012; Xu et al. 2013). We find two MCs (i.e., cloud IDs 16 and 116 in Table 1) that are probably at  $\sim 1.3$  kpc and  $\sim 1$  kpc, respectively, based on Model A. However, due to lacking a convincing distance measurement from Model B, we suspect that the foreground molecular gas at 1–1.3 kpc is likely overlapped on the masers’ cloud. This effect leads to where we just detect the nearer distance of the foreground gas. According to the multijump model (in preparation), jump features in the  $A_G$ -Distance map can be discerned at  $\sim 1.51$  kpc and 1.73 kpc, respectively.

We identify that an MC (see m5 in Table 2) with an LSR velocity of  $-5 \text{ km s}^{-1}$  is associated with AFGL2591 at a distance of 3.3 kpc (Rygl et al. 2010). We find that the m5 cloud is overlapped with L889 filament (see Figure 11d). The cloud has a high bright temperature and large line widths, indicating the massive star formation within it. Another small cloud (see m2 in Table 2) with a medium bright temperature and column density is associated with a

2.7 kpc maser toward the direction of Cygnus OB1. Finally, for the two masers more than 3 kpc G075.76+0.33 (Xu et al. 2013) and G075.78+0.34 (Ando et al. 2011), we find intense CO emission at  $\sim 800$  pc located just in front of the two masers. As a result, we are unable to identify the MCs associated with them.

The difficulty increases when looking for more distant CO emission in our field of view (FOV). For the more distant clouds, smaller angular sizes, together with large extinction and parallax uncertainty of stars from Gaia DR3, limit us from determining their distances. These more distant clouds also suffer from extinction of foreground layers (i.e. the 800 pc, 1 kpc, and 1.3 kpc gas layer) identified in this paper.

We measured at least seven clouds (classes I and II) with distances larger than 1.4 kpc. All of them are in a large radius (i.e., at least larger than  $5'$  based on  $^{13}\text{CO}$  emission). Most of them are located in relatively high latitude regions and/or simple extinction environments, leading to less contamination of foreground emission. The above two facts enable us to determine their distances after background elimination.

Table 1. Parameters of 207 MC structures with distance measurement

(1)	(2)	(3)	(4)	(5)	(6)	(7)	(8)	(9)	(10)	(11)	(12)	(13)
ID	$l$	$b$	$v_{\text{LSR}}$	$\sigma_v$	$R$	$d^A$	$d^B$	$N_{\text{mean}}$	Mass <sup>LTE</sup>	Mass <sup>Xfactor</sup>	$\alpha$	Adopted Model
	(deg)	(deg)	(km s <sup>-1</sup> )	(km s <sup>-1</sup> )	(pc)	(pc)	(pc)	(cm <sup>-2</sup> )	( $m_{\odot}$ )	( $m_{\odot}$ )		
1	72.29	2.31	-2.2	1.2	5.2	1784 <sup>+27</sup> <sub>-20</sub> ± 89	1745 <sup>+20</sup> <sub>-26</sub> ± 87	5.98e+21	10,920	12,170	0.8	A
2	72.43	0.38	4.1	1.4	4.1	2478 <sup>+76</sup> <sub>-42</sub> ± 123		1.50e+21	1740	3000	5.5	A
3	72.62	0.76	5.6	0.7	1.5	959 <sup>+18</sup> <sub>-19</sub> ± 47	964 <sup>+22</sup> <sub>-22</sub> ± 48	7.21e+20	110	210	8.3	A
4	72.68	-0.74	5.0	1.2	2.5	1072 <sup>+30</sup> <sub>-28</sub> ± 53		1.39e+21	570	870	6.9	A
5	73.23	0.58	5.4	0.6	1.4	1001 <sup>+37</sup> <sub>-33</sub> ± 50	994 <sup>+39</sup> <sub>-36</sub> ± 49	1.03e+21	140	240	3.9	A
6	73.23	-0.69	7.1	0.9	1.9	1095 <sup>+24</sup> <sub>-34</sub> ± 54	1052 <sup>+36</sup> <sub>-35</sub> ± 52	1.68e+21	400	360	4.1	A
7	73.31	-0.06	3.1	1.2	6.5	1671 <sup>+32</sup> <sub>-31</sub> ± 83		2.39e+21	6750	10,240	1.5	A
8	73.44	-0.69	3.7	1.3	2.5	1060 <sup>+22</sup> <sub>-30</sub> ± 53	1038 <sup>+25</sup> <sub>-26</sub> ± 51	1.67e+21	710	940	6.4	A
9	73.99	3.56	-4.5	1.2	3.6	1909 <sup>+74</sup> <sub>-93</sub> ± 95	1872 <sup>+90</sup> <sub>-74</sub> ± 93	4.62e+21	3930	4610	1.6	A
10	74.08	0.38	1.9	1.7	4.4	1108 <sup>+26</sup> <sub>-20</sub> ± 55		2.70e+21	3460	5350	4.2	A
11	74.09	-0.50	6.2	0.9	2.1	1000 <sup>+83</sup> <sub>-41</sub> ± 50		1.91e+21	570	790	3.6	A
12	74.18	-4.79	10.1	1.0	1.6	959 <sup>+22</sup> <sub>-23</sub> ± 47	969 <sup>+24</sup> <sub>-24</sub> ± 48	8.91e+20	160	240	12.5	A
13	74.31	0.16	2.3	1.3	2.8	1014 <sup>+36</sup> <sub>-34</sub> ± 50		2.60e+21	1390	2180	4.3	A
14	74.35	-2.47	3.1	1.2	1.7		1258 <sup>+42</sup> <sub>-57</sub> ± 62	2.33e+21	430	820	6.9	B
15	74.88	-4.67	11.9	0.5	1.8	908 <sup>+20</sup> <sub>-20</sub> ± 45	899 <sup>+35</sup> <sub>-27</sub> ± 44	1.01e+21	220	290	2.8	A

NOTE—

- (1) ID: cloud ID in this work of distance measured molecular clouds, sorted by longitude.  
(2)  $l$ : longitude of cloud center weighted by intensity; see Equation (3).  
(3)  $b$ : latitude of cloud center weighted by intensity; see Equation (4).  
(4)  $v_{\text{LSR}}$ : velocity of cloud center weighted by intensity; see Equation (8).  
(5)  $\sigma_v$ : intensity weighted velocity dispersion of clouds; see Equation (9).  
(6)  $R$ : physical size of molecular cloud, in unit of pc; see Equation (17).  
(7)  $d^A$ : median value of cloud distance measured using Model A. The uncertainties represent 16th/84th value in MCMC samples of cloud distance measured using Model A (lower/upper value of  $1\sigma$  confidence interval).  
(8)  $d^B$ : median value of cloud distance measured using Model B. The uncertainties represent 16th/84th value in MCMC samples of cloud distance measured using Model B (lower/upper value of  $1\sigma$  confidence interval).  
(9)  $N_{\text{mean}}$ : the mean column density of each cloud based on LTE, which is calculated by Equation (13) and (16).  
(10) Mass<sup>LTE</sup>: LTE mass derived from <sup>13</sup>CO emission with determined distance, which is calculated by column density of <sup>13</sup>CO emission; see Equation (13) and (18).  
(11) Mass<sup>Xfactor</sup>: mass calculated by <sup>12</sup>CO emission with determined distance, in a <sup>13</sup>CO traced cloud boundary. The CO-to-H<sub>2</sub> conversion factor adopts  $X_{\text{CO}} = 2 \times 10^{20} \text{ cm}^{-2} (\text{K} \cdot \text{km} \cdot \text{s}^{-1})^{-1}$ .  
(12) Virial parameter of <sup>13</sup>CO traced cloud, which is calculated by Equation (21).  
(13) Adopted Model: determine which model to give a more accurate distance.  
(This table is available in its entirety in machine-readable form.) Only a portion of this table is shown here to demonstrate its form and content. A machine-readable version of the full table is available.

**Table 2.** Physical Properties of molecular clouds matched with masers

ID	$l$	$b$	Parallax <sup>a</sup>	Parallax Error <sup>a</sup>	$v_{\text{maser}}^a$	$v_{\text{LSR}}$	$\sigma_v$	$T_{\text{peak}}$	Column Density	$R_{\text{eff}}$	Mass	$\alpha_{\text{vir}}$
	(deg)	(deg)	(mas)	(mas)	(km s <sup>-1</sup> )	(km s <sup>-1</sup> )	(km s <sup>-1</sup> )	(K)	(cm <sup>-2</sup> )	(pc)	( $M_{\odot}$ )	
m1 <sup>(1)</sup>	73.93	-1.86	0.629	0.017	5.0	5.6	1.3	6.9	3.4e+21	5.8	7580	1.4
m2 <sup>(2)</sup>	74.56	0.79	0.367	0.083	-1.0	-0.6	1.0	4.6	2.8e+21	2.7	1420	2.3
m3 <sup>(1)</sup>	76.39	-0.66	0.770	0.053	-2.0	-2.1	1.3	10.6	9.6e+21	1.1	810	2.8
m4 <sup>(3)</sup>	78.12	3.63	0.645	0.030	-6.0	-3.3	1.3	7.9	9.8e+21	0.6	250	4.6
m5 <sup>(4)</sup>	78.60	0.89	0.300	0.010	-5.7	-5.3	1.7	10.8	3.1e+21	14.1	41,530	1.2
m6 <sup>(4)</sup>	79.74	1.01	0.737	0.062	-3.0	-1.6	1.0	4.5	3.3e+21	1.9	840	2.9
m7 <sup>(1)</sup>	79.87	1.19	0.620	0.027	-5.0	-4.2	1.2	8.0	9.9e+21	0.6	290	3.6
m8 <sup>(6)</sup>	80.39	-2.33	0.620	0.047	-3.0	-4.1	1.1	8.4	2.9e+21	5.5	5770	1.3
m9 <sup>(4)</sup>	80.88	0.36	0.687	0.038	-3.0	-2.1	1.4	11.7	7.0e+21	3.1	4510	1.7
m10 <sup>(4)</sup>	80.91	-0.28	0.666	0.035	-3.0	-3.4	1.0	10.9	9.5e+21	1.1	770	1.7
m10 <sup>(7)</sup>	80.98	-0.13	0.666	0.035	-3.0	-3.1	0.8	10.6	1.0e+22	1.3	1180	0.8
m10 <sup>(7)</sup>	80.99	-0.09	0.666	0.035	-3.0	-2.4	0.9	10.0	6.9e+21	0.8	300	2.7
m10 <sup>(7)</sup>	81.08	-0.19	0.666	0.035	-3.0	-4.9	1.0	14.1	7.8e+21	2.2	2620	0.9
m10 <sup>(7)</sup>	81.22	0.88	0.666	0.035	-3.0	14.6	1.6	10.9	1.1e+22	2.7	5790	1.4
m10 <sup>(7)</sup>	81.35	-0.05	0.666	0.035	-3.0	-5.0	1.2	16.3	1.1e+22	3.6	9440	0.7
m10 <sup>(7)</sup>	81.54	0.09	0.666	0.035	-3.0	-6.0	1.0	11.0	7.5e+21	2.3	2740	0.9
m10 <sup>(7)</sup>	81.57	0.71	0.666	0.035	-3.0	-1.6	1.0	14.4	8.0e+21	3.8	7700	0.5
m10 <sup>(7)</sup>	81.61	-0.03	0.666	0.035	-3.0	9.6	1.0	10.1	5.7e+21	2.3	2110	1.4
m10 <sup>(7)</sup>	81.64	0.49	0.666	0.035	-3.0	-2.0	0.7	10.1	1.4e+22	0.5	230	1.1
m10 <sup>(7)</sup>	81.64	0.75	0.666	0.035	-3.0	8.5	0.8	10.4	5.9e+21	1.4	770	1.2
m10 <sup>(7)</sup>	81.74	0.58	0.666	0.035	-3.0	-4.1	1.7	17.3	2.2e+22	0.9	1390	2.4
m10 <sup>(7)</sup>	81.83	0.97	0.666	0.035	-3.0	-0.7	1.1	14.6	7.5e+21	2.9	4140	1.0
m10 <sup>(7)</sup>	81.83	1.26	0.666	0.035	-3.0	11.3	1.3	13.3	1.0e+22	2.6	4630	1.1
m10 <sup>(7)</sup>	81.86	0.88	0.666	0.035	-3.0	-2.1	1.1	15.9	1.2e+22	2.3	4160	0.7
m11 <sup>(4,5)</sup>	81.95	0.71	0.772	0.042	7.0	11.2	1.7	11.6	6.4e+21	2.6	2990	3.1

Note.

(1): cloud parameters of m3 (Xu et al. 2013) are alternatively from S106 cloud or G076.39–0.66; here is the latter one (see Section 5.5).

(2): Burns et al. (2014).

(3): Moscadelli et al. (2011), Nagayama et al. (2015).

(4): in order, AFGL2591, IRAS 20290+4052, DR20, DR21, and W 75N from Rygl et al. (2012).

(5): Rygl et al. (2010).

(6): Zhang et al. (2012).

(7): clouds associated with DR21 filament (Rygl et al. 2012).

<sup>a</sup> Parameters derived from masers' measurement.

## 6. DISCUSSION

### 6.1. Big picture

#### 6.1.1. The Cygnus Rift

Cygnus Rift is a foreground molecular structure in Cygnus complex (Hiltner & Johnson 1956; Dame & Thaddeus 1985), which makes heavy obscuration in optical images. Dame & Thaddeus (1985) assumed that the Rift is confused together with Cygnus X above  $l=74^\circ$ . However, the exact spatial and distance distribution is still up for debate, especially in the part overlapping with the background Cygnus X star-forming region. What is the real extension of Cygnus Rift in true 3D space? What are the accurate distances for the different gas distribution for the whole Cygnus region? What is the difference between the molecular gas in Cygnus X star-forming region and those in Cygnus Rift?

The overall distributions of MCs toward the Cygnus region (including both the Cygnus X star-forming region and the foreground Cygnus Rift) show multiple gas layers based on our new measurements (see Section 5). We reveal that the clouds in the 800 pc gas layer mainly concentrate along the 800 pc loop, mainly including the foreground emission of the Cygnus X North and NAP region therein (see Sections 5.1 and 5.3). Based on the MC distance measurements

**Table 3.** Physical Properties of MCs matched with PDR interfaces

ID	$l$	$b$	$v_{\text{LSR}}$	$\sigma_v$	$T_{\text{peak}}$	Column Density	$R_{\text{eff}}$	Mass	$\alpha_{\text{vir}}$
	(deg)	(deg)	(km s <sup>-1</sup> )	(km s <sup>-1</sup> )	(K)	(cm <sup>-2</sup> )	(pc)	( $M_{\odot}$ )	
p1 <sup>a</sup>	76.94	2.22	1.4	1.1	17.2	6.0e+21	4.3	7440	0.8
p2 <sup>b</sup>	77.22	1.52	0.0	0.8	7.8	3.3e+21	0.8	140	4.0
p3 <sup>a</sup>	77.47	1.85	1.4	1.4	13.3	1.1e+22	4.6	16,170	0.6
p4 <sup>c</sup>	77.97	0.03	-2.5	1.2	6.5	3.6e+21	2.7	1830	2.6
p5 <sup>a</sup>	77.98	1.77	-1.9	1.0	11.7	8.4e+21	3.4	6490	0.6
p6 <sup>c</sup>	78.00	0.56	-2.5	2.0	7.3	6.3e+21	2.0	1610	5.5
p7 <sup>c</sup>	78.16	-0.31	-0.5	2.1	7.1	6.4e+21	2.7	3080	4.3
p8 <sup>b</sup>	78.46	2.67	0.5	0.8	15.2	1.4e+22	1.0	980	0.9
p9 <sup>a</sup>	79.18	2.21	-2.2	0.8	11.1	8.3e+21	1.4	1120	1.0
p10 <sup>d</sup>	79.26	0.25	3.4	1.0	10.0	6.2e+21	1.0	440	2.8
p11 <sup>d</sup>	79.87	1.19	-4.2	1.2	8.0	9.9e+21	0.7	330	3.4
p12 <sup>d</sup>	79.98	0.84	-10.8	1.2	12.5	9.6e+21	1.3	1150	1.8
p13 <sup>d</sup>	80.38	0.44	8.3	0.9	16.8	1.3e+22	1.0	890	1.0
p14 <sup>d</sup>	80.84	0.56	11.6	1.0	8.8	8.4e+21	1.0	600	2.1
p15 <sup>e</sup>	80.91	-0.28	-3.4	1.0	10.9	9.5e+21	1.2	980	1.5
p16 <sup>e</sup>	80.98	-0.13	-3.1	0.8	10.6	1.0e+22	1.5	1510	0.7
p17 <sup>e</sup>	81.08	-0.19	-4.9	1.0	14.1	7.8e+21	2.5	3360	0.8
p18 <sup>a</sup>	81.27	1.05	15.5	0.7	7.9	7.4e+21	0.8	350	1.3
p19 <sup>a</sup>	81.50	0.48	7.0	0.8	11.6	7.7e+21	1.5	1120	1.1

*Note.*

<sup>a</sup> Cometary clouds are likely shaped by Cygnus OB associations.

<sup>b</sup> Irregular clouds.

<sup>c</sup> Oval-shaped HII regions identified by [Downes & Rinehart \(1966\)](#), in order: DR9, DR6, and DR13.

<sup>d</sup> Globules near the center of far-FUV sources.

<sup>e</sup> Clouds match a hub-like HII region in Cygnus X North; see panel (e) of [Figure 8](#).

**Table 4.** Mass Evaluation

Region	Comments	LTE ( $M_{\odot}$ )	X-factor ( $M_{\odot}$ )	by <sup>13</sup> CO (2-1) <sup>a</sup> ( $M_{\odot}$ )
Cygnus	by Table 1	$2.4 \times 10^5$	$3.5 \times 10^5$	
	by Table 1-3	$4 \times 10^5$	$5.3 \times 10^5$	
	whole	$1.1 \times 10^6$	$2.7 \times 10^6$	
Cygnus within 1 kpc	by Table 1	$2.6 \times 10^5$	$6.2 \times 10^5$	
Cygnus X	Cygnus X North (0~3 kpc)	$2.3 \times 10^5$	$4 \times 10^5$	
	Cygnus X North (1.3~1.7 kpc)	$1.7 \times 10^5$	$3.2 \times 10^5$	$2.8 \times 10^5$
	Cygnus X South (0~3 kpc)	$4.1 \times 10^5$	$8.3 \times 10^5$	
	Cygnus X South (1.3~1.7 kpc)	$3.2 \times 10^5$	$7 \times 10^5$	$4.5 \times 10^5$

**Table 4.** The mass estimated in different subregions/distance intervals.

<sup>a</sup> Estimated by [Schneider et al. \(2006\)](#) based on <sup>13</sup>CO (2-1) and the LTE method.

toward the whole region, the 800 pc gas layer also extends to the Cygnus X South region. The 800 pc gas layer extends to at least  $\sim 135$  pc along the longitude and a thickness of  $\sim 80$  pc (i.e., the FWHM of the Gaussian fitting from the distances distribution of MCs). The average value and variance of the column density in this layer ( $700 \text{ pc} \leq d \leq 900 \text{ pc}$ ) are  $3.1 \times 10^{21} \text{ cm}^{-2}$  and  $2.3 \times 10^{21} \text{ cm}^{-2}$ , respectively.

The 1 kpc gas layer is also widespread in both of the Cygnus X North and Cygnus X South regions. We find that these clouds have similar velocity distributions, peak temperature, and mean column density. Based on our results, we attribute them as a whole gas layer at  $\sim 1$  kpc; nevertheless, the clouds in the Cygnus X North region are slightly more distant. Similarly, we estimate the length and depth of the 1 kpc gas layer with  $\sim 145$  pc along the longitude and a thickness of  $\sim 70$  pc, respectively. The average value and variance of the column density in this layer ( $900 \text{ pc} \leq d \leq 1100 \text{ pc}$ ) are  $2.5 \times 10^{21} \text{ cm}^{-2}$  and  $1.2 \times 10^{21} \text{ cm}^{-2}$ , respectively.

Combining the 800 pc and 1 kpc gas layers, the Cygnus Rift is distributed across a large spatial extent of at least in  $l = [72^\circ, 87^\circ]$  and  $b = [-5^\circ, 4^\circ]$ . The distance of Cygnus Rift ranges from the nearer NAP region ( $\gtrsim 700$  pc) to the farther gas layers (e.g., Cygnus X North, Cyg-NW at 1 kpc) according to MCs' distances. These dark clouds toward the region, composing multiple gas layers with slightly different distances. The accumulation of molecular gas along these layers makes large extinctions in some directions (i.e. the ‘‘extinction wall’’ effect, [Straizys et al. 1993](#)). Therefore, it is hard to determine the distances for the distant MCs behind the Cygnus Rift. For example, the contamination from foreground emission at the Cygnus Rift leads to a biased distance measurement in previous studies of S106. The average value and variance of the column density of combined layers are  $2.8 \times 10^{21} \text{ cm}^{-2}$  and  $1.9 \times 10^{21} \text{ cm}^{-2}$ , respectively.

As is presented above, the molecular gas in Cygnus Rift is better identified and measured. It plays an important role in revealing the 3D view along the LOS. Studying molecular gases (e.g., distributions and physical properties) in the foreground is also helpful to reveal the MCs behind them. For example, we may reveal the detailed gas structures associated with the high-energy emission from Cygnus Cocoon ([LHAASO Collaboration 2024](#)) We need more advanced methods (e.g., multijump) to properly separate the gas at different distances. Finally, a big picture of the whole region will be well delineated.

### 6.1.2. Molecular Gas behind the Cygnus Rift

The distribution of clouds in the 1.3 kpc gas layer is different between the Cygnus X North and South regions. The majority of clouds in this layer are located in the south region based on our distance measurements (see Section 5.2; also see the special cases measured only by Model B in Appendix D). The result also agrees with the previous studies ([Zucker et al. 2020](#); [Dharmawardena et al. 2022](#)). However, it does not mean that there is no molecular gas at 1.3 kpc gas layer in the Cygnus X North region. We propose that clouds (see m11 in Table 2 and Figure 10a) associated with W 75N ( $\sim 1.3$  kpc, [Rygl et al. 2012](#)) in the Cygnus X North are also in this layer. These clouds' distances are relatively smaller than that of the Cygnus North Filament ( $\sim 1.5$  kpc for DR20 and DR21 in [Rygl et al. 2012](#)). We notice clouds in this layer have a slightly larger brightness temperature and mean column densities than the clouds within 1 kpc (see Figure 12). The clouds are probably heated by nearby star-forming regions, i.e. substructures of Cygnus OB2 identified by [Berlanas et al. \(2019\)](#), [Orellana et al. \(2021\)](#).

We note 1.3 kpc layer is also distributed extensively (see middle layer in Figure 17) based on the MWISP data and our results. It is interesting that some clouds associated with HII regions (DR6, DR9, DR13, etc.) have similar physical properties as compared to those clouds in 1.3 kpc layer (see Figure 12). Furthermore, DR13 cloud (see ID 48 in Table 1) has been measured in  $1320_{-157}^{+182}$  pc, supporting the association between the heated molecular gas and PDR interfaces. Therefore, some clouds with intense infrared emission are probably located in the 1.3 kpc layer, although we temporarily put the clouds matching with infrared structures (Table 3) at  $\sim 1.7$  kpc.

On the contrary, few clouds in the 1.3 kpc gas layer toward the Cygnus X North are successfully measured in our method. We suspect that the majority of molecular gas behind the 800 pc and 1 kpc gas layers are likely located at  $\sim 1.5$  kpc. For example, the massive Cygnus North Filament (see Figure 10a) contributes to the majority of CO emission in this region, which also agrees with the presence of the densest region toward Cygnus X North at  $\sim 1.5$  kpc ([Rygl et al. 2012](#); [Dharmawardena et al. 2022](#)).

The clouds associated with background PDR interfaces in both regions are likely related to the Cygnus OB2, while cometary clouds in Cygnus X South (labeled in A, B, C, and S106; see Figures 11 and 16) could also be influenced by star members in Cygnus OB1 ( $\sim 1.7$  kpc from [Quintana & Wright 2021](#); [Rastorguev et al. 2023](#)). In addition, the molecular gas is likely concentrated in 1.5 kpc toward the Cygnus X North region (see blue histogram in right panel in

Figure 7). On the other hand, the gas in the Cygnus X South region is mainly at  $\sim 1.3$  and  $\sim 1.7$  kpc. Actually, only two MCs (IDs 19 and 67 in Table 1) in the Cygnus X South region are at 1.5 kpc with Model B. These indicate the different molecular gas distribution between the Cygnus X North and South regions. We suggest that the Cygnus X star-forming region is not an integral structure located in the same distances based on maser measurements and our new MC distance measurements from Gaia DR3.

### 6.1.3. Comparison with the distribution of YSOs

Furthermore, we use selected YSO candidates (see Appendix F) to trace the spatial distribution of young stars toward the Cygnus region. We find that the majority of YSO candidates spatially coexist very well with the  $^{13}\text{CO}$  structures, especially for molecular gas within 1 kpc (see Figure 17). Along the 800 pc gas loop (see 800 pc layer in Section 5.1), the significant overdensity of YSO candidates can be found toward the NAP region and the superposed subregion toward the Cygnus X North (see Figure 10b), while the coincidence between the YSOs and molecular gas is also discerned in L914 and molecular gas at  $[l \sim 83^\circ, b \sim 2^\circ]$ . Additionally, the overdensity of YSO candidates also coincides with the molecular gas in the Cygnus X South region. Different from the Cygnus X North region, the distribution of YSO candidates extends to farther gas layers. It again indicates the 1.3 kpc middle gas layer is mainly distributed toward the Cygnus X South region.

Behind the Cygnus Rift, YSOs still roughly follow the distribution of molecular gas. Interestingly, the spatial distribution of YSO candidates is much more extended toward the star-forming regions at  $\gtrsim 1.4$  kpc. We find that the overdensities of YSOs are roughly associated with identified molecular gas and OB associations in those regions.

For the multiple gas layers, the results reveal that a significant overdensity of potential young stars occurs in the vicinity of molecular gas traced by  $^{13}\text{CO}$ , indicating the connection between them.

## 6.2. Molecular gas mass toward the Cygnus Region

A summary of the derived masses is listed in Table 4. Here, we first discuss the total mass of the molecular gas based on  $^{13}\text{CO}$  emission in LTE (see equation 14 and 18). Obviously, the fractional detection rate ( $FDR$ ) of clouds with distance has a major influence on the total mass estimation.  $FDR$  can be estimated by the ratio of flux between the distance measured clouds (see Tables 1–3) and raw data.

First we defined  $FDR_1$  (here, 48.6% for the whole region) as the flux ratio between MCs with distance and the total identified  $^{13}\text{CO}$  clouds. Second,  $FDR_2$ , the flux ratio between the total identified  $^{13}\text{CO}$  clouds and masked raw data, is 72.6% (see Section 3.2). Thus, we obtain  $FDR = FDR_1 \times FDR_2 = 35.3\%$ . The total mass of clouds with known distances in Cygnus traced by  $^{13}\text{CO}$  structures, including clouds within 1 kpc and Cygnus X MSFRs, is about  $M_{\text{Table1-3}} \sim 4 \times 10^5 M_\odot$ , leading to the total mass  $M_{\text{overall}} \sim 1.1 \times 10^6 M_\odot$  for the whole region.

We note that  $FDR_1$  in different layers are not the same, which has a dominant influence on the total mass estimation in Cygnus traced by  $^{13}\text{CO}$ . In addition, the beam filling factor (Sun et al. 2021b; Yan et al. 2021c) and the smaller coverage of  $^{13}\text{CO}$  emission would lead to the underestimation of the molecular gas mass. So the total mass estimated above is still a lower limit toward the whole Cygnus region traced by  $^{13}\text{CO}$  emission.

Alternatively, we further use  $^{12}\text{CO}$  emission to estimate the total mass of molecular gas toward the whole Cygnus region. For each identified  $^{13}\text{CO}$  structure, we give an X-factor mass from corresponding  $^{12}\text{CO}$  emission in the same PPV space. Similarly, the molecular mass can be estimated to be  $M_{\text{Table1-3}}^{\text{Xfactor}} \sim 5.3 \times 10^5 M_\odot$  for the corresponding  $^{13}\text{CO}$  structure by adopting  $X_{\text{CO}} = 2 \times 10^{20} \text{cm}^{-2} (\text{K} \cdot \text{km} \cdot \text{s}^{-1})^{-1}$  (Bolatto et al. 2013). The  $^{12}\text{CO}$  flux ratio between the identified structures with distance and the raw data is about 19.5%, leading to the total molecular mass of  $M_{\text{overall}}^{\text{Xfactor}} \sim 2.7 \times 10^6 M_\odot$  in the whole Cygnus region. Considering the underestimation of  $FDR_1$  in the above calculation, the estimated mass of  $M_{\text{overall}}^{\text{Xfactor}} \sim 2.7 \times 10^6 M_\odot$  is still a lower limit.

In Table 4, we make further efforts to estimate the mass of molecular gas within 1 kpc (mainly from Cygnus Rift). Similar to the above analysis, we use  $FDR_2 = 72.6\%$  and  $FDR_1 \sim 1$  to evaluate the total mass within 1 kpc. According to Table 1, the total molecular mass within 1 kpc is estimated to be  $M_{1\text{kpc}}^{\text{LTE}} \sim 2.6 \times 10^5 M_\odot$ . Assuming the same ratio from  $M_{\text{overall}}^{\text{Xfactor}} / M_{\text{overall}}^{\text{LTE}}$  for the gas layers within 1 kpc, the low limit of  $M_{1\text{kpc}}^{\text{Xfactor}}$  is about  $6.2 \times 10^5 M_\odot$  because the emissions of those small structures are ignored.

For comparison with previous work (e.g., Schneider et al. 2006), we evaluate the mass of the Cygnus X region. For the Cygnus X North region ( $FDR_1 = 59.3\%$ ,  $FDR_2 = 83.9\%$ ), the total mass (0–3 kpc) of molecular gas is  $M_{\text{CygNorth}}^{\text{LTE}} \sim 2.3 \times 10^5 M_\odot$  and  $M_{\text{CygNorth}}^{\text{Xfactor}} \sim 4 \times 10^5 M_\odot$ , respectively. Assuming  $FDR_1 \approx 1$  for foreground molecular gas within 1 kpc, we estimated that molecular mass from background emission (mainly from 1.3 to 1.7 kpc)

is  $M_{\text{CygNorth}}^{\text{LTE}} \sim 1.7 \times 10^5 M_{\odot}$  and  $M_{\text{CygNorth}}^{\text{Xfactor}} \sim 3.2 \times 10^5 M_{\odot}$  by subtracting the foreground mass. Similarly, for the Cygnus X South region ( $FDR_1 = 48.9\%$ ,  $FDR_2 = 74.6\%$ ), the total molecular mass is  $M_{\text{CygSouth}}^{\text{LTE}} \sim 4.1 \times 10^5 M_{\odot}$  and  $M_{\text{CygSouth}}^{\text{Xfactor}} \sim 8.3 \times 10^5 M_{\odot}$ . Additionally, the molecular masses associated with the nearby star-forming region are  $M_{\text{CygSouth}}^{\text{LTE}} \sim 3.2 \times 10^5 M_{\odot}$  and  $M_{\text{CygSouth}}^{\text{Xfactor}} \sim 7 \times 10^5 M_{\odot}$  for 1.3~1.7 kpc.

The total mass toward Cygnus X in 1.3~1.7 kpc is  $M_{\text{CygnusX}}^{\text{LTE}} \sim 4.9 \times 10^5 M_{\odot}$ ,  $M_{\text{CygnusX}}^{\text{Xfactor}} \sim 1 \times 10^6 M_{\odot}$ , respectively. We note ~20% flux toward the direction is from the molecular gas within 1 kpc. We also attached the mass evaluated by  $^{13}\text{CO}$  (2–1) (Schneider et al. 2006) based on LTE method. Our new results are supposed to be smaller than those of Schneider et al. (2006), knowing that we put part of the MCs in a closer place (e.g., the gas layers within 1 kpc). On the other hand, the difference of estimated molecular mass between the two works is likely from the different transitions from  $^{13}\text{CO}$ .

### 6.3. From PPV to PPP

It is sometimes assumed that the CO emission in PPV space corresponds to coherent structures in position–position–position (PPP) space. However, in the simulation results in Beaumont et al. (2013), there are two possible problems in cloud decomposition from PPV to PPP. The first one is that the gas emission with different velocity components (thus probably with different distances) are combined into the same spatial structure. And the other is that clouds belonging to a coherent structure in real 3D space exhibit two or more velocity components that are separated in PPV space. Due to the prevalent feedback from star-forming activities, great caution must be exercised when discussing the properties of identified features in PPV space (Clarke et al. 2018). Many structures with a single feature in PPV space would not be directly identified as coherent features in PPP space. For example, Perseus Arm in longitude–velocity diagram is not a continuous structure in true spatial space (Peek et al. 2022) based on the 3D dust map (Green et al. 2019). We also find that some identified gas structures with different velocities are located at the same distance (e.g., see Figures 9, 12, and 14).

Without a distance measurement, cloud clustering methods can actually introduce two problems. One is overdecomposition to the whole MC complex linked by many substructures with different velocity features, while the other is a mistaken aggregation of unrelated structures in PPP space because of close velocities. In our work, we confirmed that the clouds in NAP region are from a whole MC complex, although the algorithm decomposes the complex into different velocity structures (see Section 5.3, Figures 13 and 14). On the contrary, it is necessary to avoid a wrong aggregation of different spatial structures, considering the complicated velocity structure toward Cygnus region. For the first case, with the distance measurement, substructures from the overdecomposition can be linked together to form larger cloud complexes (see the 800 pc loop with a large extension of  $\sim 4^{\circ} \times 4^{\circ}$  in Figure 17). Finally, many identified MCs with close velocities are indeed located in different distances based on our cloud clustering and distance measurements (see Figures 8 and 11). Therefore, accurate distance measurements, together with appropriate cloud clustering, allow us to better describe the true distribution of molecular gas in the Milky Way.

Adler & Roberts (1992) indicate that the size–line width relationship from modeling galactic disk is not a reliable indicator of the physical nature of cloud complexes. We also caution against using the results of clustering MCs with various methods and size–line width relation from PPV space (Shetty et al. 2010; Pan et al. 2015) without an accurate distance measurement. Our results clearly demonstrate a very wide range of distances for clouds with close velocities toward the Cygnus region. And conversely, the clouds located in the same layers might have very different velocity features (see Figures 9 and 12). From this work, we propose that the studies of MCs within 3 kpc should be revisited in details at Gaia’s age of precise astronomy (Zucker et al. 2023). The true 3D distribution of MCs is essential to construct a large-scale structure of our Galaxy.

## 7. SUMMARY

We study the properties and distribution of MCs toward the Cygnus region ( $\sim 150 \text{ deg}^2$ ) from the MWISP CO survey. Here, we summarize the main conclusions in this work:

(1) We identified 3829 structures based on coherent spatial and velocity structures of  $^{13}\text{CO}$  emission. About 72.6% fluxes are recovered after Gaussian decomposition and clustering from GaussPy+ and ACORNS.

(2) Combining the identified cloud structures and data from Gaia DR3, we design two models (A and B) to measure distances of molecular gas in the Cygnus region. Among the identified  $^{13}\text{CO}$  structures, we obtain distances for over 200 large clouds (i.e.,  $\geq 60 \text{ arcmin}^2$ ). 120 clouds are measured by both Models A and B (class I). 22 clouds are only

measured by Model B (class II), and over 60 clouds are alone measured by Model A (class III). The flux of MCs with distance (classes I and II in Table 1) contributes to about 31.2% total flux of the identified  $^{13}\text{CO}$  structures.

(3) About 20 clouds are coincidental with bright mid-IR emission (see panel e in Figures 8 and 11; also see Table 3). The association between the MCs and surrounding star-forming regions is also supported by MC properties (cometary morphology, high peak temperature, and intense emission of the gas, etc.). Moreover, based on our models, some clouds with oval-shaped and irregular morphology (e.g., DR13) are indeed measured to be  $\sim 1.3$  kpc. These clouds associated with PDR interfaces are probably related to OB subgroups at  $\sim 1.3$  kpc.

(4) Additionally, we find that tens of MC structures are associated well with masers in Table 2. The distances of these MCs can be obtained based on the association between masers and the corresponding molecular gas. We also find that our independent measurement of a cloud (cloud 94 in Table 1) is consistent with the corresponding maser’s distance of 1.36 kpc (Rygl et al. 2012).

(5) The spatial distribution of YSOs’ candidates coincides well with  $^{13}\text{CO}$  structures within 1 kpc, indicating the tight connection between them. These cases in (2), (3), (4), and (5) show that our models are effective for distance measurement to MCs in velocity crowding regions.

(6) Our distance measurements of MCs, combined with the additional information from molecular gas associated with masers and nearby OB associations, show that there are multiple layers of gas structure toward Cygnus region: (I) the gas in 800 pc and 1 kpc layer composing Cygnus Rift, (II) the 1.3 kpc layer majorly in Cygnus X South, and (III) the Cygnus North Filament and the adjacent dense gas at 1.5 kpc, as well as many cometary MCs directly shaped by Cygnus OB associations at  $\sim 1.7$  kpc (see Figure 17). The results reveal the complex distribution of molecular gas toward Cygnus region, both in spatial and velocity distribution. The total masses of molecular gas of the whole Cygnus region are  $\sim 1.1 \times 10^6 M_{\odot}$  by LTE, and  $\sim 2.7 \times 10^6 M_{\odot}$  by X-factor (see Table 4).

(7) Our work determines the large spatial extent of Cygnus Rift at least in  $l = [72^{\circ}, 87^{\circ}]$  and  $b = [-5^{\circ}, 4^{\circ}]$ . The distances of the MCs are well determined in the range of 700 pc to 1 kpc, revealing the multilayer nature toward the Cygnus Rift (see Figures 7 and D1). For example, the foreground gas toward the Cygnus X North region is composed by 800 pc and 1 kpc layers. The superposition of gas structures toward L889 in the Cygnus X South also exists. The large extinction of the foreground gas in these directions causes the failure of the distance measurement for MCs at larger distances (i.e., “extinction wall” effect). The molecular mass of the foreground Cygnus Rift (within 1 kpc) contains  $\sim 25\%$  of the whole region.

(8) We propose that the molecular gas associated with the Cygnus X star-forming region does not come from an integral structure. Actually, there are different molecular structures at different distances, such as  $\sim 1.3$  kpc molecular gas that are likely associated with subgroups of Cygnus OB2, the dense gas in Cygnus North Filament at  $\sim 1.5$  kpc, and the cometary MCs shaped by Cygnus OB associations at  $\sim 1.7$  kpc (see histogram in right panel of Figure 7). Toward the Cygnus X SFR, the molecular gas within 1.3–1.7 kpc is about  $\sim 4.9 \times 10^5 M_{\odot}$  by LTE, and  $\sim 1 \times 10^6 M_{\odot}$  by X-factor.

We find that abnormal jumps and/or multijump features of  $A_G$ -Distance map are common toward the Cygnus region. Besides the gas layers discussed above, there are likely other gas structures at different distances in the whole region. For example, some MCs at  $\sim 550$  pc (i.e. clouds 198 to 203 and 205 in Table 1; also see light red contours in Figure 17) are in front of Cygnus Rift in the region  $l \geq 85.^{\circ}3$ . These clouds have relatively small sizes and column density, thus contribute to the small proportion of mass within 1 kpc (see histograms in Figure 7). These clouds at 500–600 pc are probably related to the MC complex toward the Cygnus OB7. We indeed detect that two jump features are exactly at  $\sim 550$  pc and  $\sim 760$  pc in NAP region, corresponding to the different gas layer therein. We propose that the multilayer nature of molecular gas is ubiquitous. We will develop a multiple jumps detection model to further reveal the 3D molecular gas distribution of Cygnus region in a forthcoming paper.

Acknowledgments. We would like to thank the anonymous referee for the valuable comments and suggestions that have largely improved the manuscript. This research made use of the data from the Milky Way Imaging Scroll Painting (MWISP) project, which is a multiline survey in  $^{12}\text{CO}/^{13}\text{CO}/\text{C}^{18}\text{O}$  along the northern Galactic plane with the PMO 13.7 m telescope. We are grateful to all the members of the MWISP working group, particularly the staff members at the PMO 13.7m telescope, for their long-term support. MWISP was sponsored by the National Key R&D Program of China with grants 2023YFA1608000, 2017YFA0402701, and the CAS Key Research Program of Frontier Sciences with grant QYZDJ-SSW-SLH047. This work is supported by NSFC grants 12173090, 12073079. X.C. acknowledges the support from the Tianchi Talent Program of Xinjiang Uygur Autonomous Region and the support by the CAS International Cooperation Program (grant No. 114332KYSB20190009). This work also made use of data from the European Space Agency (ESA) mission Gaia (<https://www.cosmos.esa.int/gaia>), processed by the Gaia Data Processing and Analysis Consortium (DPAC, <https://www.cosmos.esa.int/web/gaia/dpac/consortium>). Funding for the DPAC has been provided by national institutions, in particular the institutions participating in the Gaia Multilateral Agreement.

*Facilities:* PMO: DLH, Gaia

*Software:* astropy (Astropy Collaboration et al. 2013, 2018, 2022), scikit-learn (Pedregosa et al. 2011), emcee (Foreman-Mackey et al. 2013), Pymc3 (Salvatier et al. 2016), Matplotlib (Hunter 2007).

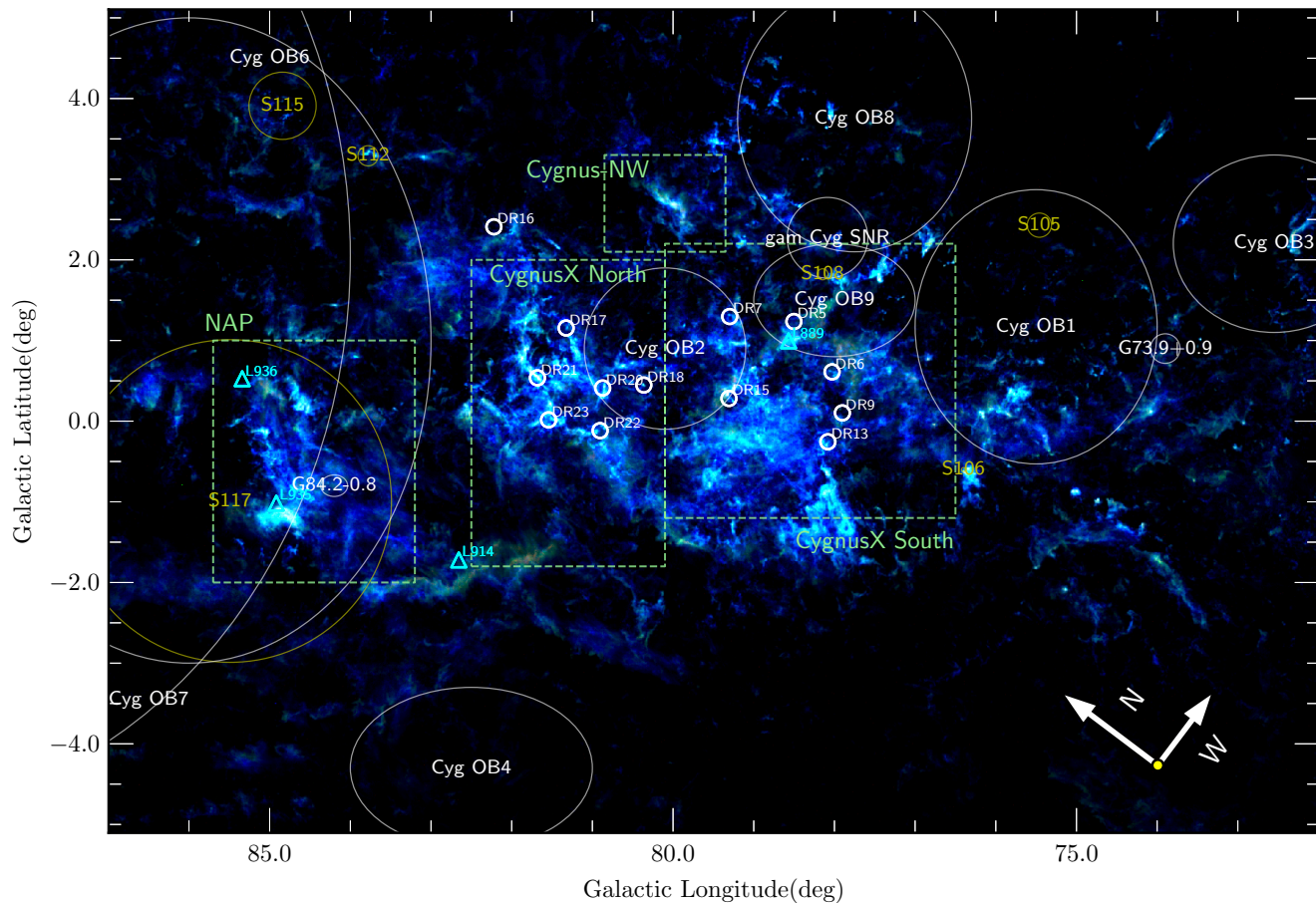


**Figure 1.** A composite guide map colored in R ( $C^{18}O$ ), G ( $^{13}CO$ ), B ( $^{12}CO$ ) based on the MWISP data. The map is made by moment masking method. That is, pixels with three continuous channels beyond 3 times that of the noise level have been kept. Many prominent structures are denoted on this map, including OB associations and SNR  $\gamma$  Cygni (labeled with large circles or ellipses), dark clouds (triangles), and radio sources (white small circles) collected by Downes & Rinehart (1966), as well as several HII regions (yellow circles). The light green rectangles indicate some interesting subregions discussed in Section 5.

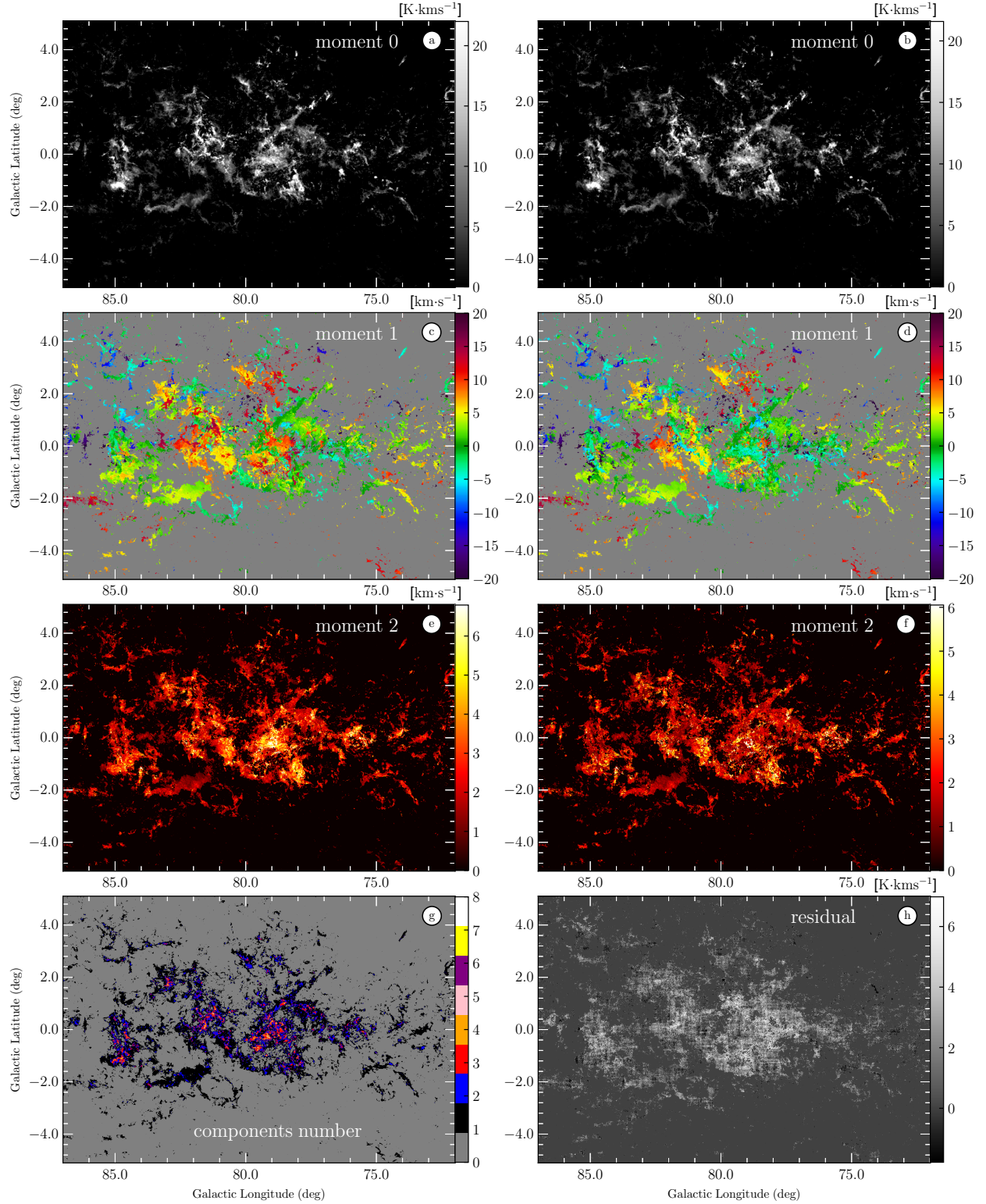


**Figure 2.** (a) Reconstruction of moment 0 map of  $^{13}\text{CO}$  emission; the values in gray scale are fluxes summed up by all Gaussian components in each sight line. (b) Similar to (a), but only for the emission with Gaussian components after clustering. (c) Reconstruction of moment 1 map, showing the centroid velocity of Gaussian components. We choose most positive velocities on the top (top positive), but not a weighted average. (d) The same with (c), but smallest velocities on the top (top minus). (e) The moment 2 map, showing the line width of most positive velocities on the top. (f) The same with (e), but smallest velocities on the top. (g) The distribution of the number of Gaussian components in the whole region. And (h) the residuals between integrated emission of raw data and reconstructed image by Gaussian decomposition.

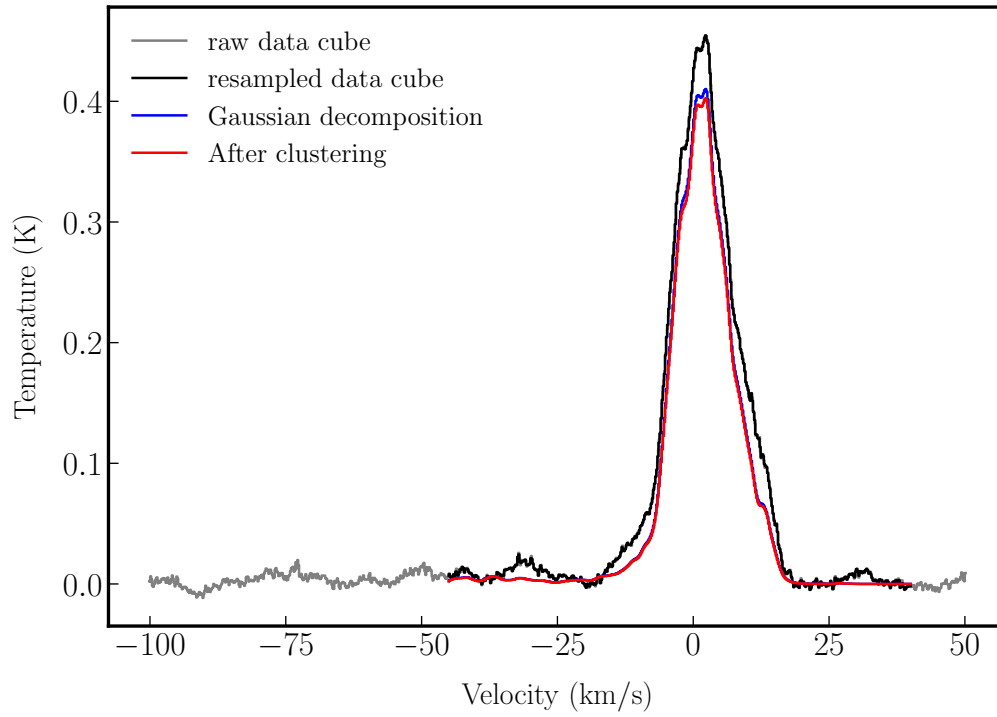


**Figure 3.** The average spectrum of  $^{13}\text{CO}$  toward the Cygnus region. Gray line shows the raw data truncated from  $-100$  to  $50 \text{ km s}^{-1}$ , while black line denotes the average spectrum after resampling. Blue curve indicates the average of all signals restored by Gaussian decomposition, while red line shows the average spectrum after clustering based on ACORNS (Henshaw et al. 2019). Toward the Cygnus region, we note that a collective cloud emission overlapped together within a narrow velocity range ( $-20$  to  $20 \text{ km s}^{-1}$ ). The flux reconstructed by Gaussian decomposition and clustering are 81.5% and 79.5% (see Section 3.3), respectively.

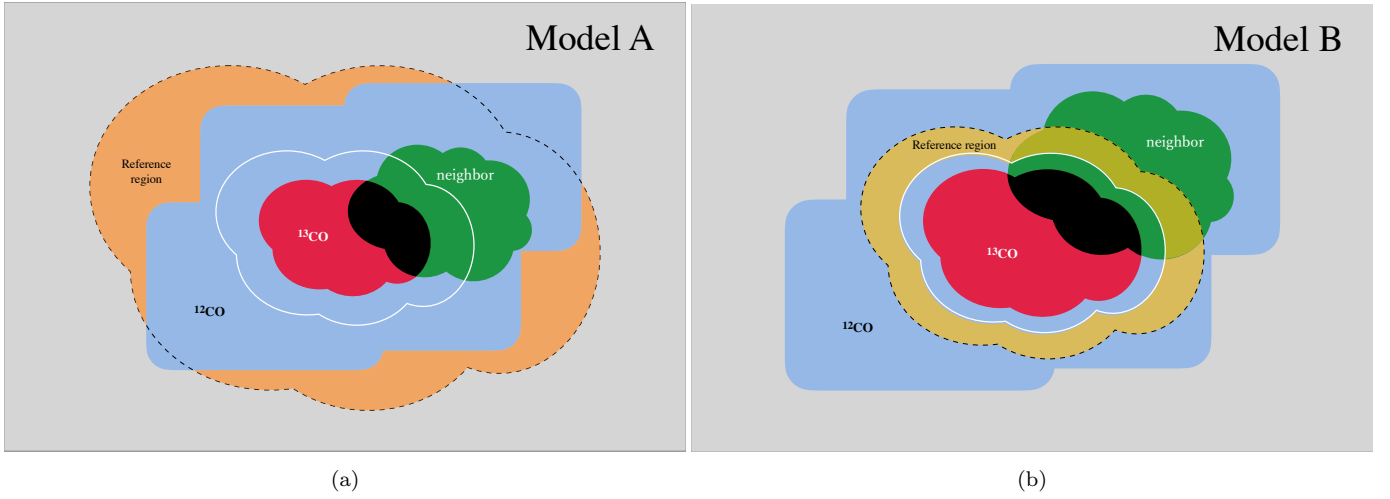


**Figure 4.** The sketches illuminate our method based on BEEP (Yan et al. 2019a). On-sources are selected within the  $^{13}\text{CO}$  structure. (a) Use  $^{12}\text{CO}$  emission to choose field stars. (b) Use  $^{13}\text{CO}$  from its own morphology to select field stars in its periphery. Red region is the identified  $^{13}\text{CO}$  cloud, which is partly overlapped by a neighboring cloud in green. The black part is the region with superposition, which include more than one Gaussian component. White solid contour and black dashed contour denote different dilation of cloud boundary. Orange part represents the reference region. Blue area represents the widespread  $^{12}\text{CO}$  emission. Obviously, Model A considers the  $^{12}\text{CO}$  free region as the reference region, while Model B refers to  $^{13}\text{CO}$  morphology to select the reference stars (see Section 4.1.2).

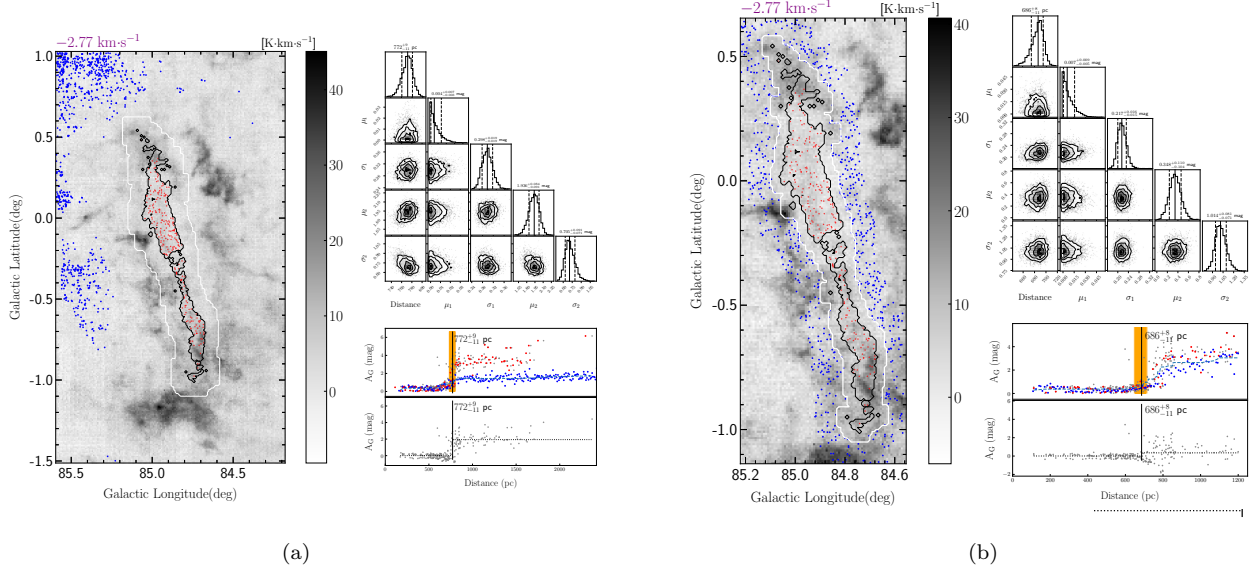


**Figure 5.** The distance measurement of cloud G084.88–0.20 (ID 185 in Table 1) from Models A and B. The Gray-scale map in the left side presents the  $^{13}\text{CO}$  integrated intensity of the cloud and its neighbors. Black contour plots the MC structure identified with ACORNS based on the Gaussian decomposition, while white contour expands the MC structure boundary with  $5'$ . All on-cloud stars located within the cloud are marked as red dots, while referenced stars (blue dots) are chosen out of white contour; see details in Figure 4. Corner plot in the upper right gives the MCMC sampling results from emcee. We set three parameters in our model,  $n_{\text{walker}}=50$ , the number of burn-in samples for Markov chain with 1000, and steps with 2000. All binary relations among parameters are presented as 2D Gaussian distributions. We compute median value (solid line) of all samples for result, and  $1\sigma$  confidence interval in dashed lines (16th and 84th percentile). Subplot in the lower right presents an  $A_G$ –Distance relation for on-cloud stars. The upper one gives  $A_G$  values before baseline elimination, while the lower one gives the result by subtracting a monotonous fitting of reference stars (see Section 4.2.2). Gray dots are raw data from Gaia DR3, while red and blue dots are binned values in a 10 pc interval for on-cloud and off-cloud stars, respectively. Orange vertical lines denote all the jump points in MCMC sampling. Model A give a significant jump, and it matches better with distances in literature of NAP region.

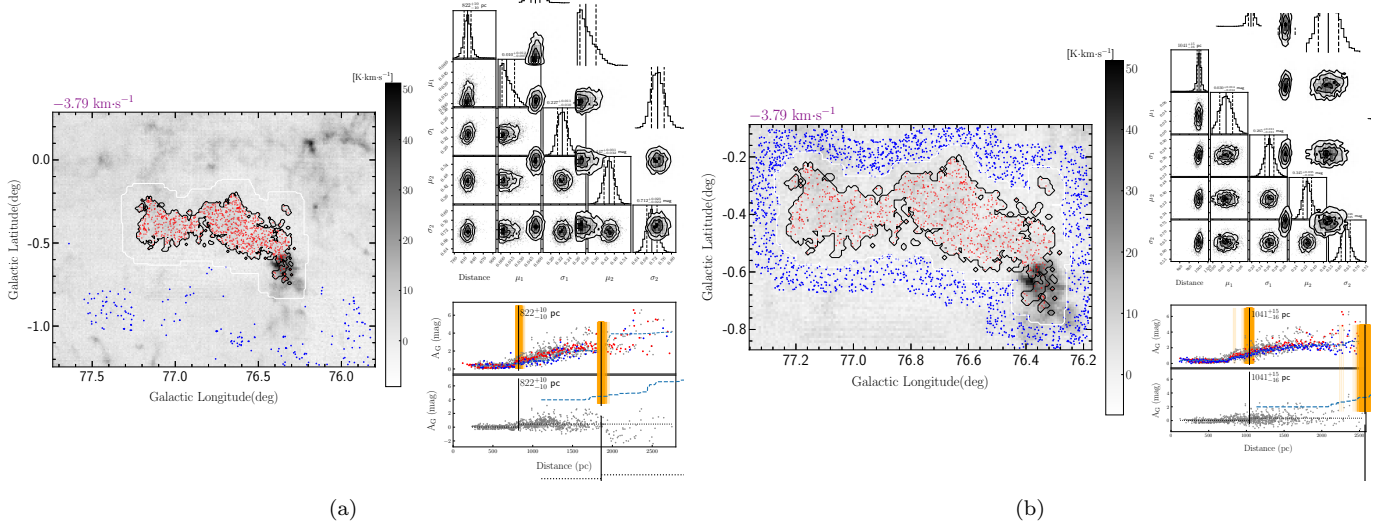


**Figure 6.** The same as Figure 5, but for cloud G76.74-0.43 (ID 30 in Table 1). The fluctuation of  $A_G$ –Distance relation for on-cloud stars for Model A denotes worse baseline fitting. We thus choose the result from Model B (see Section 4.2.2).

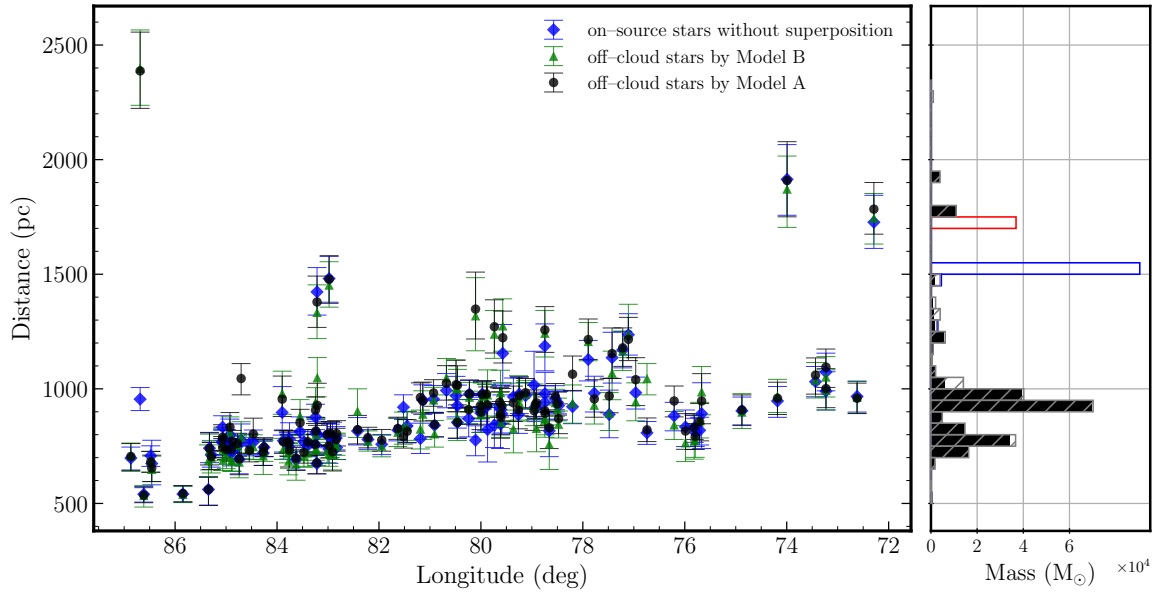


**Figure 7.** Left panel: Our results for 120 robust distance measurements both in Models A and B (class I, see details in Section 4.3). We find that all differences between Model A and Model B are smaller than 150 pc, except cloud G76.74-0.43 (ID 30 in Table 1). Right panel: LTE mass statistics based on our cloud catalog, i.e. black histogram from samples of class I in Table 1, gray histogram with slashes included class II results from Table 1, while blue and red histograms from Tables 2 and 3.

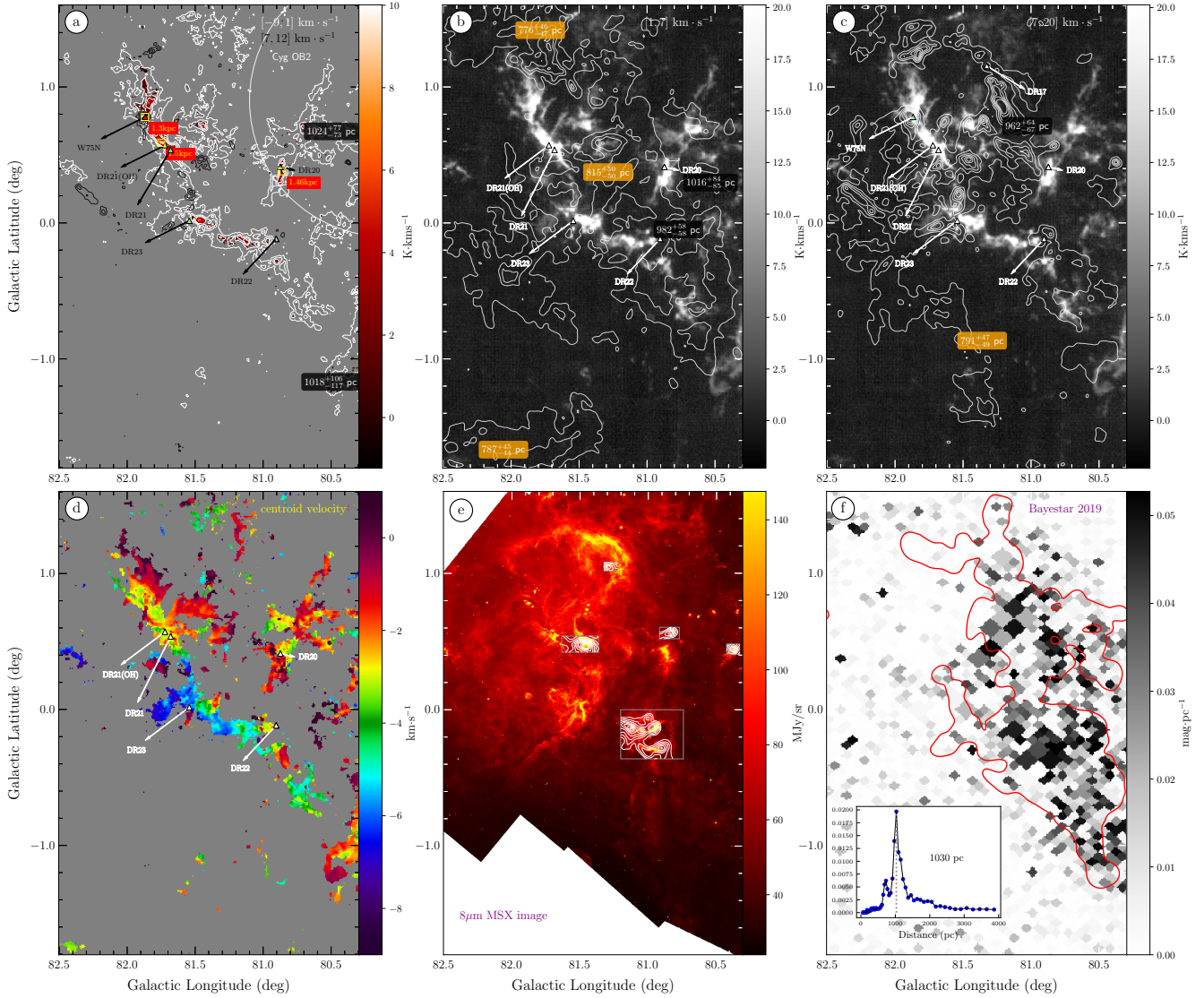


**Figure 8.** Subplots for the Cygnus X North region. Panel (a) shows  $^{13}\text{CO}$  (white contours in  $[5, 20, 35, 50] \times \sigma$ ,  $\sigma$  is the noise level of intensity map) and  $\text{C}^{18}\text{O}$  (colormap) emission in  $[-9, 1] \text{ km s}^{-1}$ . Massive star-forming regions are sited along the dense filamentary structure, i.e. DR21, DR23, and DR22. Black contours also denote the dense molecular gas in  $[7, 12] \text{ km s}^{-1}$  in same levels, e.g. W 75N is overlapped on the DR21 filament. Some HII regions are marked with triangles. The extent of Cygnus OB2 is plotted in a white circle. Distances with 5% system error of our measured clouds and those from masers are presented; different gas layers are also labeled with different colors. Panel (b): the gray-scale map is  $^{13}\text{CO}$  emission from velocity interval of  $[-9, 1] \text{ km s}^{-1}$ , overlaid with smoothed data from  $[1, 7] \text{ km s}^{-1}$  (white contours in  $[2, 6, 10, 14, 18, 22] \text{ K km s}^{-1}$ ). Panel (c): all the same with panel (b), but contours for velocities in  $[7, 20] \text{ km s}^{-1}$ . Panel (d): A moment 1 map of centroid velocities extracted from Gaussian decomposition for clouds in  $[-9, 1] \text{ km s}^{-1}$ . Obviously, prominent velocity gradient along filamentary structure can be seen. Panel (e): An  $8\mu\text{m}$  Midcourse Space Experiment (MSX) image toward the Cygnus X North region. Gray edged rectangles mark the identified molecular cloud with the associated mid-IR features. The extent of these rectangles is derived from the  $\pm 3\sigma$  of  $v$ ,  $l$ ,  $b$  relative to cloud center in Table 3. Panel (f): A 1030 pc slice of 3D dust map from Bayestar 2019 (Green et al. 2019), overlaid with the 1 kpc MC layer (red contours) from our samples (class I in Table 1) with well-determined distances. Note that our results are in good agreement with Green et al. (2019).

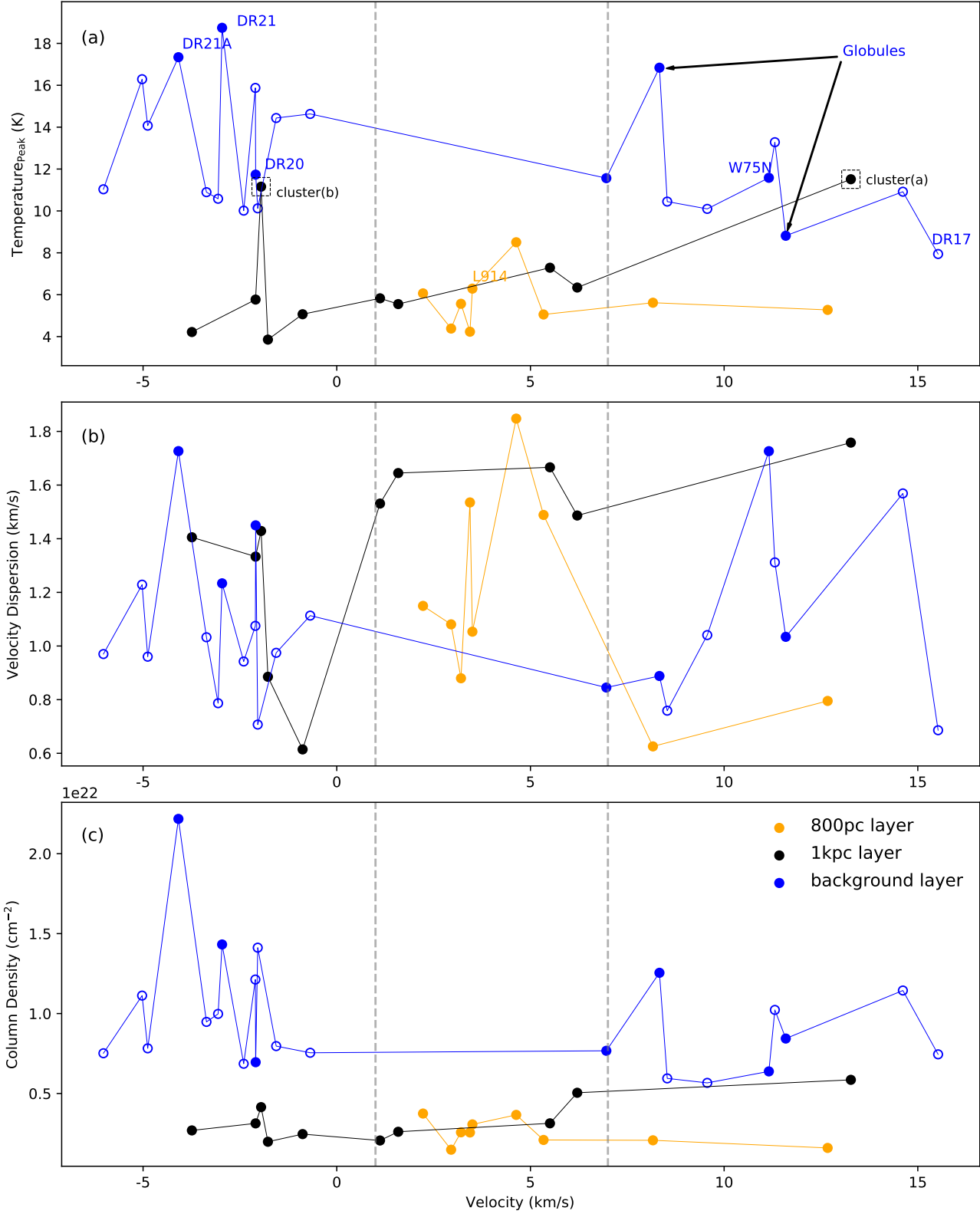


**Figure 9.** Physical properties of clouds in the Cygnus X North region. Panel (a):  $^{13}\text{CO}$  peak temperature of MCs. Different colors are marked for clouds in different layers. Clouds in background layer are associated with masers or bright cometary mid-IR features (filled blue dots) and the nearby dense gas structures (empty dots) along the filamentary structure of Cygnus X North star-forming region. Panels (b) and (c), the same with panel (a), but for velocity dispersion and column densities of the MCs.

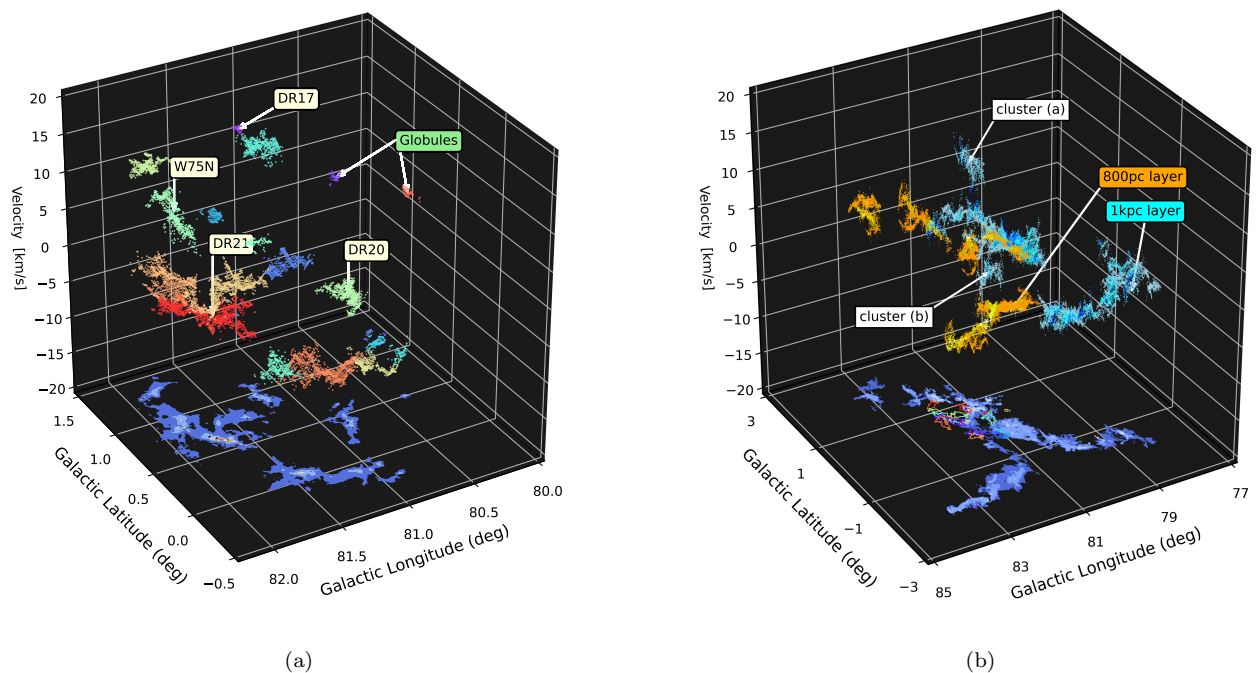


**Figure 10.** 3D plot of different gas layers toward the Cygnus X North region. Panel (a): Scatter plot of clouds in background layer (i.e., 1.3 ~ 1.7 kpc). Colors mark different  $^{13}\text{CO}$  structures identified by ACORNS, and each dot presents pixel-by-pixel centroid velocities. Their summed intensities are projected at the bottom. Panel (b): Scatter plot of clouds in 800 and 1 kpc layers. Clouds in 800 pc are in orange, while clouds in 1 kpc are in cyan. Both of the two layers display large filamentary complexes overlapped together. Clouds in 1.3 ~ 1.7 kpc layer are also plotted as colored contours on the bottom, which shows the spatial relation of different clouds on projection.

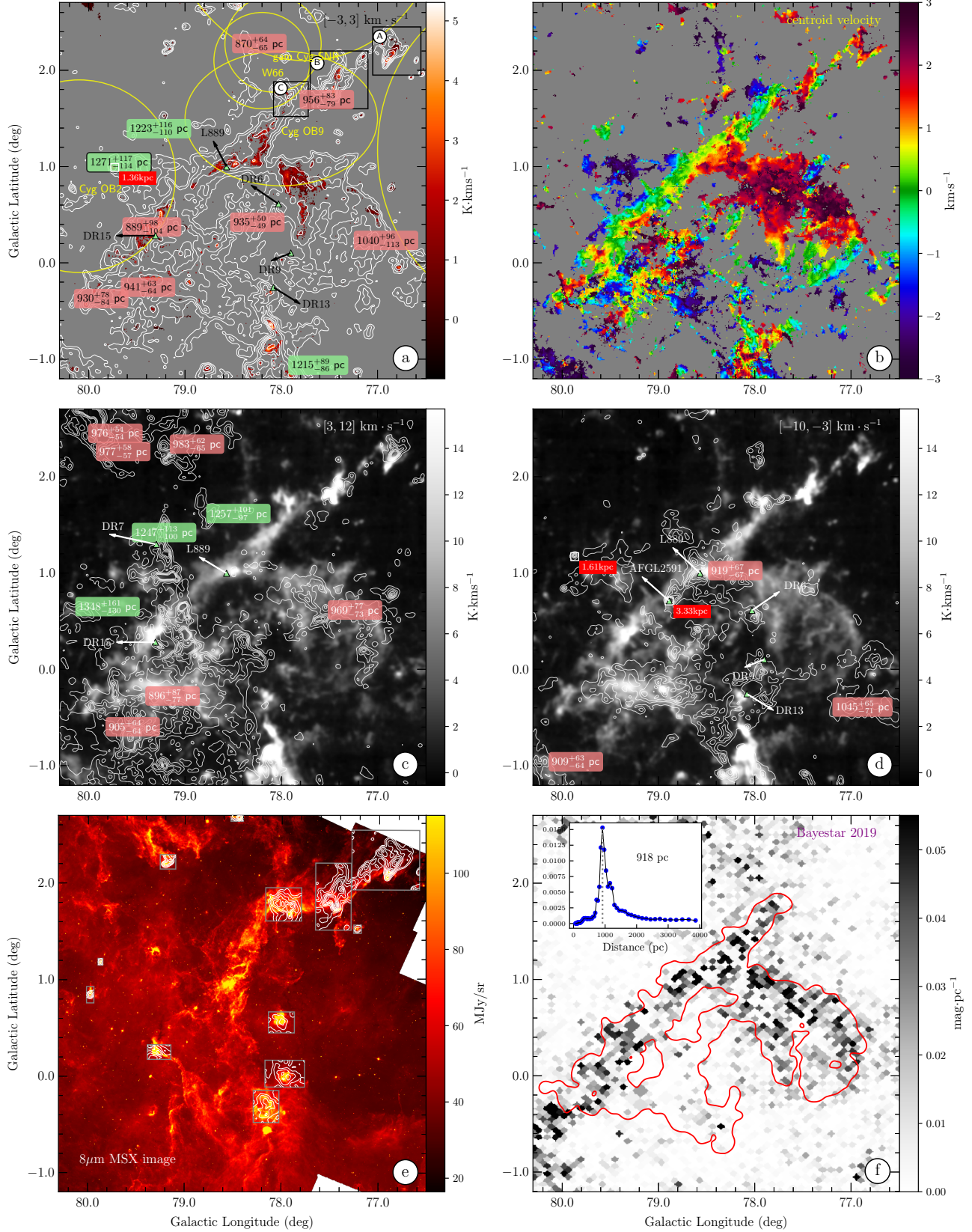


**Figure 11.** Subplots toward the Cygnus X South region. Panel (a):  $^{13}\text{CO}$  (white contours in  $[5, 10, 20, 35, 50, 70] \times \sigma$  is the noise level of intensity map) and  $\text{C}^{18}\text{O}$  (colormap) emission in  $[-3, 3] \text{ km s}^{-1}$ . These HII regions and dense cores of L889 are marked with triangles. The extent of OB associations and SNRs are plotted in yellow ellipses. Distances (with 5% system error) of our measured clouds and those from masers are also presented. Panel (b): moment 1 map in  $[-3, 3] \text{ km s}^{-1}$ . Panel (c): the grey scale map is  $^{13}\text{CO}$  emission from  $[-3, 3] \text{ km s}^{-1}$ , overlaid with smoothed data from  $[3, 12] \text{ km s}^{-1}$  with levels  $[10, 25, 40, 55, 70, 85] \times \sigma$ . Panel (d): all the same with panel (c), but contours for velocities in  $[-10, -3] \text{ km s}^{-1}$ . Panel (e): same with Figure 8e, but for Cygnus X South region. Panel (f): a 918 pc slice of 3D dust map from Bayestar 2019 (Green et al. 2019), overlaid with L889 cloud at  $\sim 935 \text{ pc}$  (red contour) from our samples (see cloud 57 in Table 1).

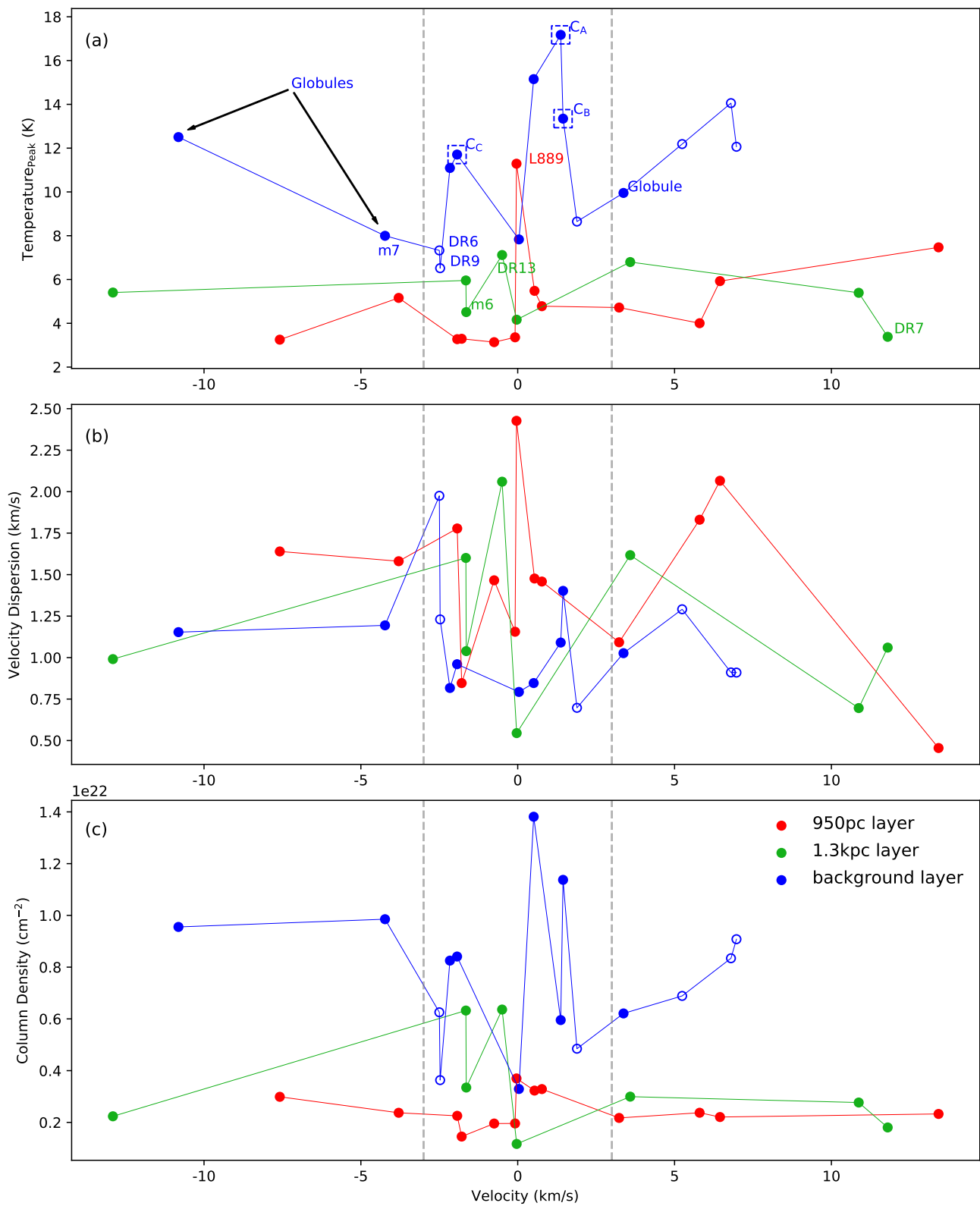


**Figure 12.** Physical properties of clouds in the Cygnus X South region. Panel (a):  $^{13}\text{CO}$  peak temperature of MCs. Different colors are marked for clouds in different gas layers. Clouds in background layer (blue dots) are all associated with bright mid-IR features. Clouds in filled dots have cometary or globular morphology, which is a strong evidence that has been shaped by massive OB star groups, e.g., cloud A, B marked by [Schneider et al. \(2006\)](#), while clouds in empty dots are oval shaped or irregular, e.g. DR6 and DR9. Panels (b) and (c): the same with panel (a), but show velocity dispersion and column densities of the clouds.

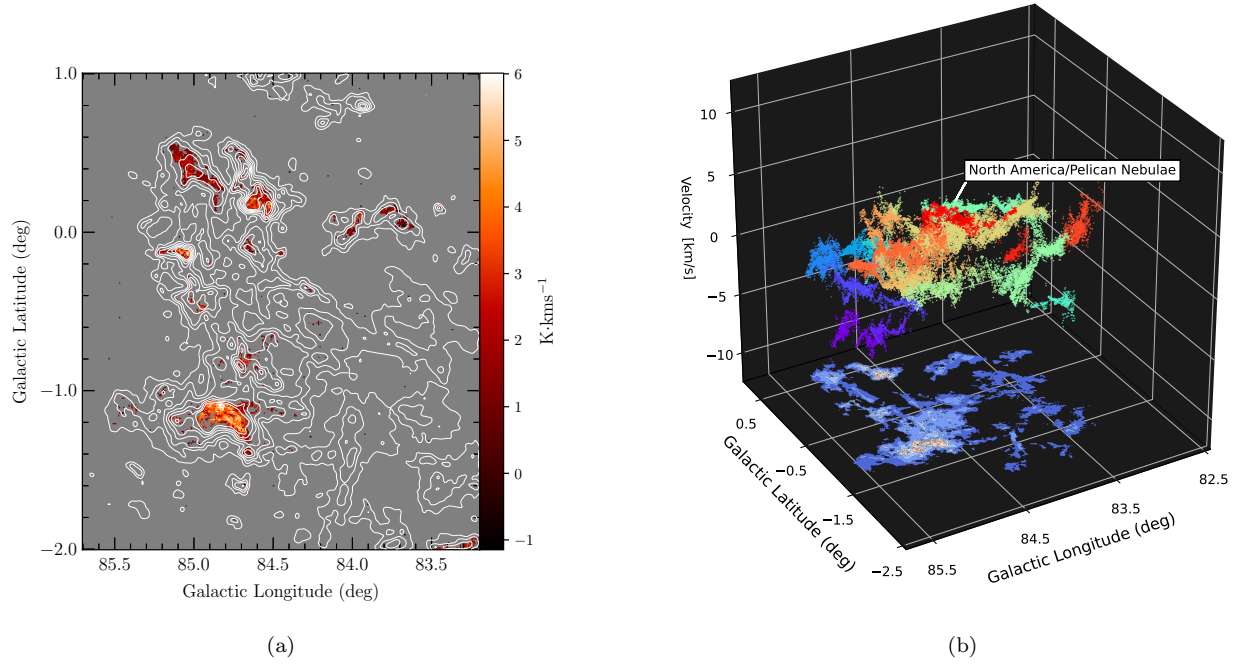


**Figure 13.** Panel (a):  $^{13}\text{CO}$  (white contours in  $[10, 20, 30, 45, 60, 75, 90] \times \sigma$ ,  $\sigma$  is the noise level of intensity map) and  $\text{C}^{18}\text{O}$  (colormap) emission in  $[-10, 10] \text{ km s}^{-1}$  toward the NAP region. Panel (b): a 3D plot for all  $^{13}\text{CO}$  structures with measured distances in the region.

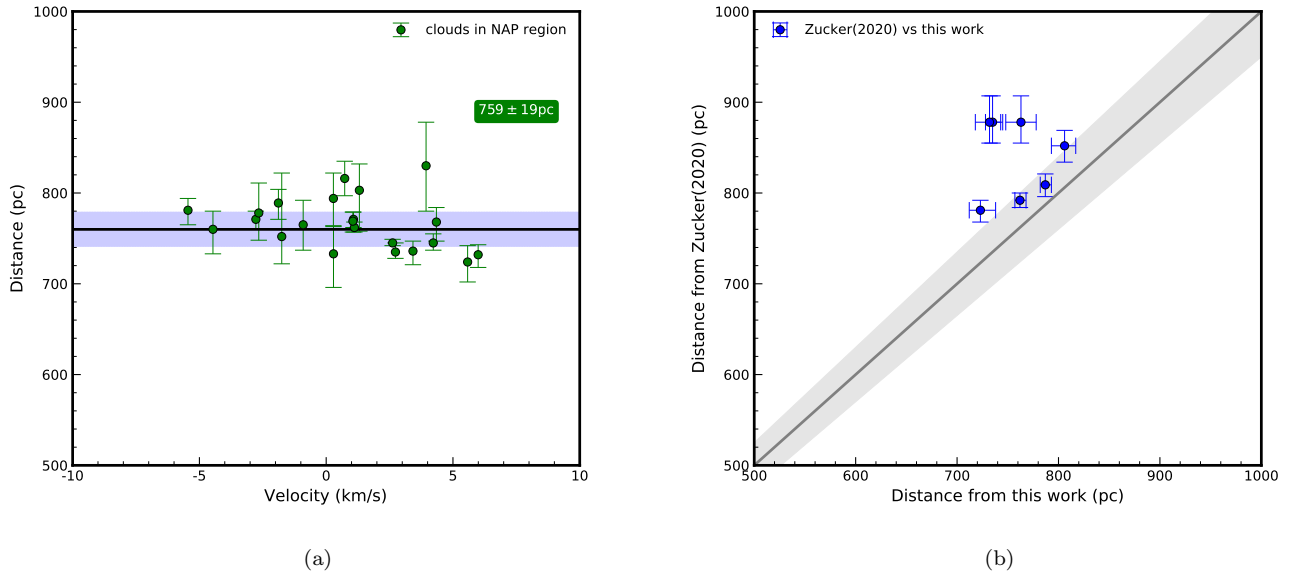


**Figure 14.** Panel (a): Measured distances of different  $^{13}\text{CO}$  structures toward the NAP region. Black line and blue shadow show the averaged distance and dispersion (without the 5% system error) weighted by clouds' masses. Panel (b): distances compared to Zucker et al. (2020) with labeled 5% system error (gray shadow) relative to distance; a systematic deviation can be found (see details in Section 5.3).

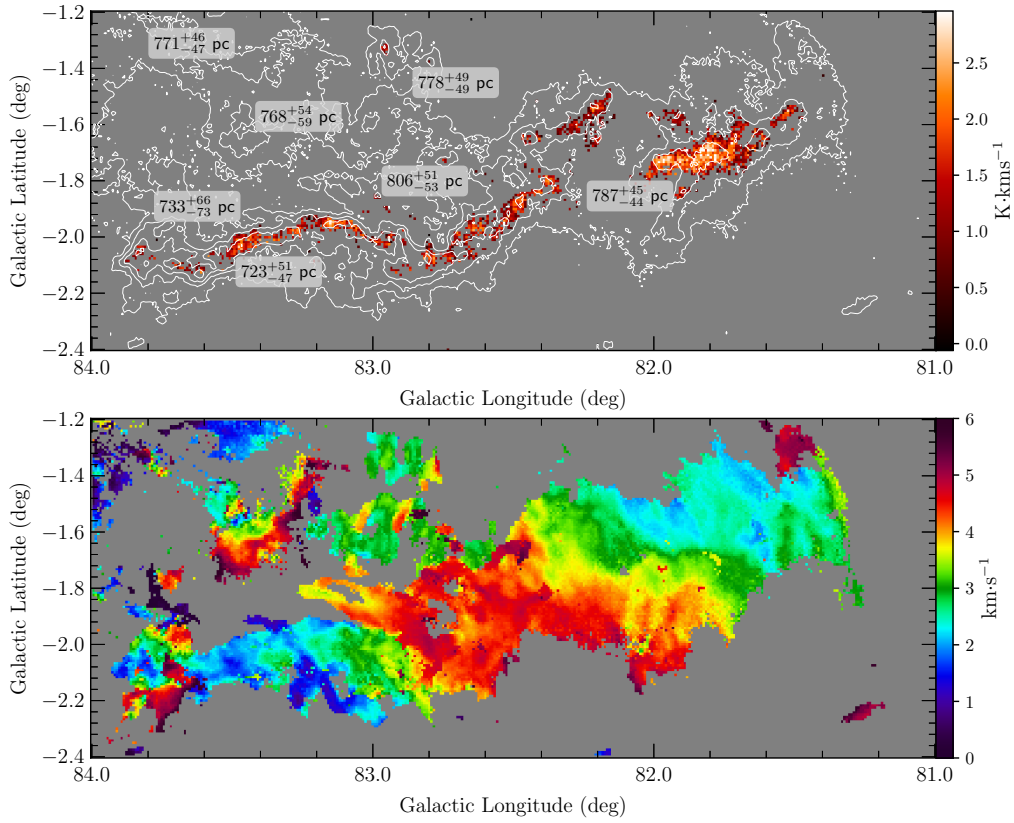


**Figure 15.** Upper panel:  $^{13}\text{CO}$  (white contours in  $[5, 15, 25, 35, 45, 55] \times \sigma$ ,  $\sigma$  is the noise level of intensity map) and  $\text{C}^{18}\text{O}$  emission (colormap) in  $[0, 6] \text{ km s}^{-1}$  toward L914. 5% system error of the distances is labeled for identified  $^{13}\text{CO}$  structures. Lower panel: moment 1 map of centroid velocities extracted from Gaussian decomposition for the above velocity interval.

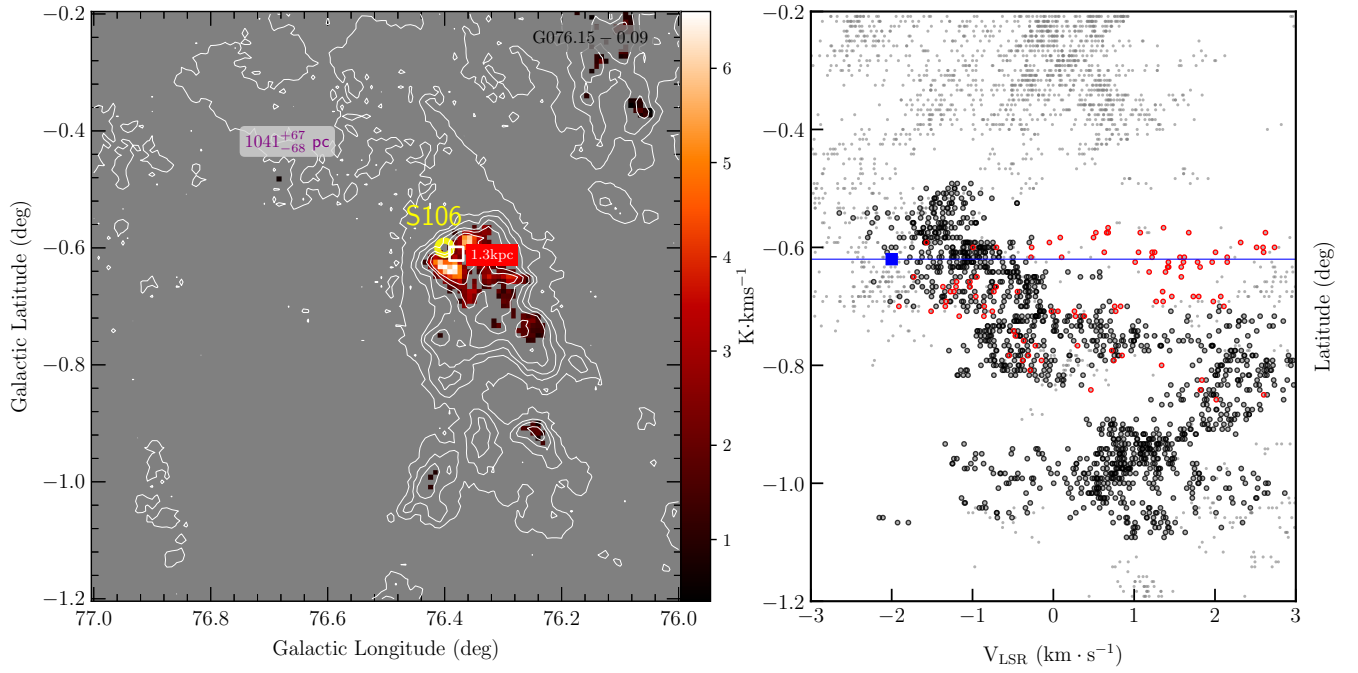


**Figure 16.** Left panel:  $^{13}\text{CO}$  (white contours in  $[5, 15, 25, 35, 45, 55] \times \sigma$ ,  $\sigma$  is the noise level of intensity map) and  $\text{C}^{18}\text{O}$  emission (colormap) in  $[-3, 3] \text{ km s}^{-1}$  toward S106. 5% system error of the distances is labeled for identified  $^{13}\text{CO}$  structures. The location of HII region (yellow circle) and maser (white box) are also labeled on the map. Right panel: the different velocity structures labeled in black and red dots in the velocity–latitude coordinates from Gaussian decomposition (see details in Section 5.5). The blue square with error represents the observed maser from Xu et al. (2013).

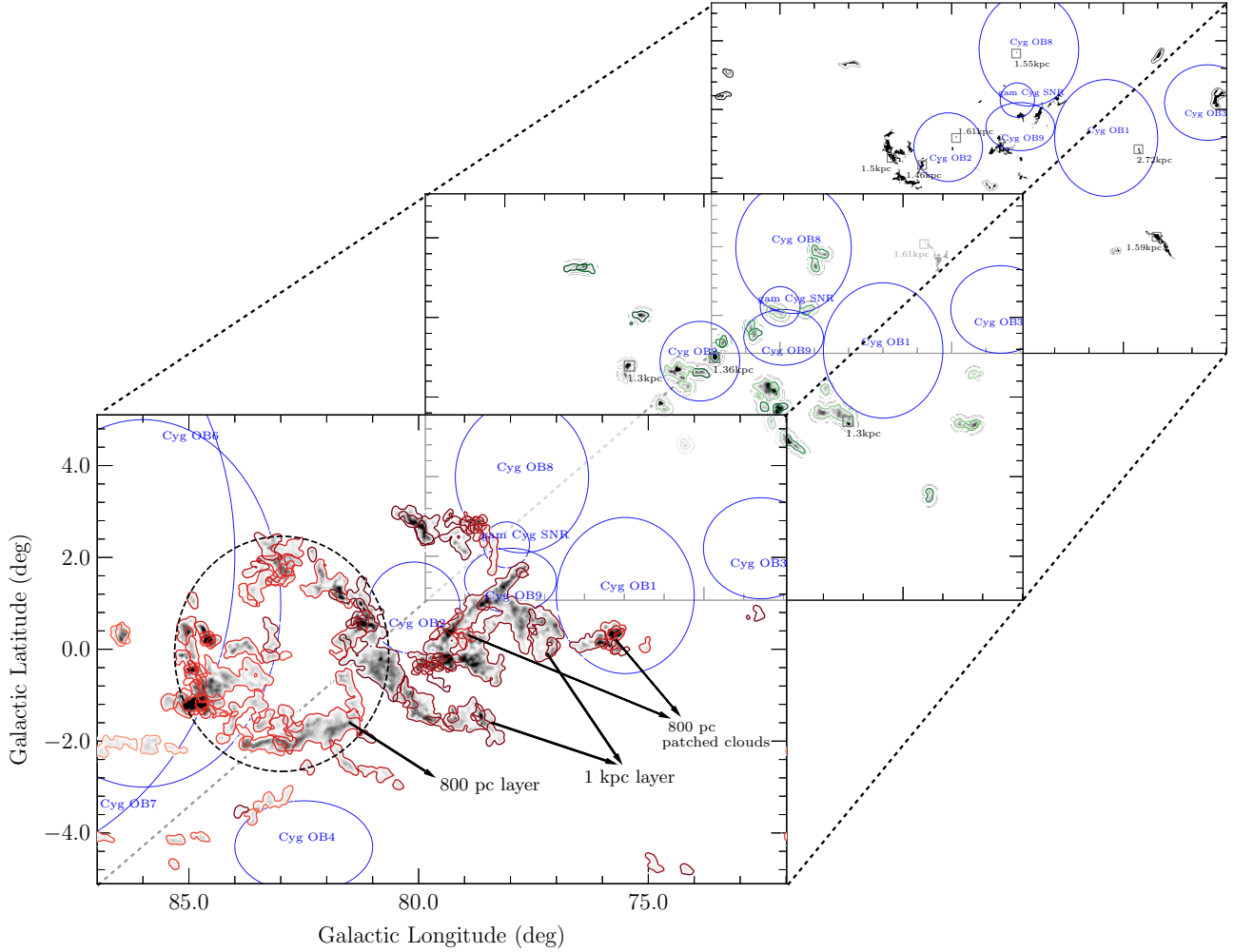


**Figure 17.** Big picture of multiple gas layers toward the Cygnus region. We divide clouds with distance measurement (see Tables 1, 2, and 3) into three intervals: [500, 1000] pc in red, [1000, 1400] pc in green, and [1400, 3000] pc in black. Lighter contours indicate nearer distance for each layer, while the darker shows the farther distances. Gray-scale maps are reconstructed by identified clouds from ACORNS, while their boundaries are delineated using a low-pass filtering method (*butterworth* in Python). The dashed ellipse shows a large-scale molecular loop with diameter of  $\sim 56$  pc at a distance of 800 pc. Different layers are also annotated in the [500, 1000] pc map. Middle map includes two layers, the  $\approx 1$  kpc clouds in light green, and  $\approx 1.3$  kpc clouds in green. Clouds in  $\geq 1.4$  kpc layer without contours are MCs associated with masers and/or mid-IR bright features in Tables 2 and 3. 7 clouds in Table 1 are successfully measured in this layer. Blue ellipses show OB associations and SNR, while boxes show the masers in Table 2.

## APPENDIX

## A. COHERENCE OF IDENTIFIED LARGE STRUCTURES

The large-size MC structures traced by  $^{13}\text{CO}$  usually display a hierarchical and spatially extended structure (see details in Section 3.1 and 3.2). See Figure A1a for an example; this large cloud, at 982 pc (see cloud 118 in Table 1 and Figure A1b) spanning  $2^\circ$  along latitude, probably suffers a different extinction environment.

We choose subregions along different LOS to measure their distances to check whether the substructures belong to a physical cloud. Firstly, the  $225 \text{ arcmin}^2$  boxes were chosen along the structure to cover various subregions as well as enough on-cloud stars. Alternatively, we took the secondary trunks in the hierarchy provided by ACORNS to include on-cloud stars. Using the same field stars for reference, we implement Model A the same way to derive their distances (blue squares for the boxes' samples and green triangles for the trunks in Figure A1c).

We find that the measured distance of the whole cloud is consistent with the mean value of the distances of every small part (see Figures A1bc). It indicates that the whole structure identified by our method does not suffer from significant contamination of unrelated emission at different distances. Similar results can also be found toward other large-scale structures, e.g. Figure A2. We suggest the large-scale structures identified by the  $^{13}\text{CO}$  emission are at similar distances.

Some subregions probably tend to be contaminated by other different MC structures along LOS (see the left three samples in Figure A1c). These small substructures in the east side are measured to be nearer (i.e.  $\sim 800$  pc). We find that these subregions are just located at the overlapping regions of 800 pc and 1 kpc gas layers of the Cygnus X North (see Figure A1d and details in Section 5.1). Our further study with the multijump detection model (in preparation) indeed shows that two layers of molecular gas are overlapped in the direction, i.e.  $\sim 800$  pc and  $\sim 1$  kpc gas in the east side of the cloud.

For another case of L889 cloud (Figure A2), the deviation of distance measurements in individual regions likely indicates the contamination from the farther 1.3 kpc layer and foreground emission (see Figure A2d and details in Section 5.2). The above discussions tell us that the overlapping between different identified structures may lead to deviations of distance measurements for subregions of a cloud.

## B. COMPARISON FOR DIFFERENT ON-CLOUD STARS' SELECTION AND MCMC SAMPLING MODULES

*All on-cloud stars versus stars after removing overlapping regions.* We test the influence of different on-cloud star samples on the measured distances by Model A (see Figure B1). In this work, we adopt all stars within the cloud boundary identified by  $^{13}\text{CO}$  as on-cloud stars (see Section 4.1.1). Alternatively, we also exclude the stars in the overlapping region. That is, we reject the stars in the black area, and keep those in the red area in Figure 4a.

We find that both of on-cloud star samples generally give consistent measurements relative to their uncertainties. The distances from overlap-removed stars give overall larger uncertainties due to fewer on-source samples. Additionally, the samples based on overlap-removed stars will decrease the number of clouds with a measured distance (29 cloud structures, about 16% in all Model A samples).

*Emcee working on the mock data.* Aiming to examine how the *emcee* works on single-jump-point detection, the mock data of extinction and distance of stars from the Cygnus region were randomly generated. In the simulation, the preset jump point (*Distance*) is randomly distributed in [500, 2000] pc, while stars samples are uniformly produced in [100, 2500] pc in number density  $0.2 \text{ pc}^{-1}$ .  $\Delta A_G$  (i.e.  $\mu_2 - \mu_1$ ) follows a truncated exponential distribution from 0.2 mag and a rate parameter of 0.5 mag. To simplify the simulation, we fix  $\sigma_1$  (0.2 mag) and  $\sigma_2$  (0.4 mag). Based on star samples toward the Cygnus region, the median error over distance and dispersion of errors are set to 0.1 and 0.06, respectively. And the mean error of  $A_G$  is set to 0.04 mag, and the dispersion of error of  $A_G$  is set to 0.04 mag. 200 groups of stars sample (see two examples in Figure B2) were produced.

We present deviations and uncertainties of distances derived from *emcee* in a relation with increasing  $\Delta A_G$  (see Figure B3). Both the deviations from the preset distance and the uncertainties from the posterior distribution decrease with the increasing  $\Delta A_G$ . Since the fitted background extinction is likely to be larger for Model B after a background elimination, Model A gives a statistically better fit when they reveal the same jump. The deviations from most samples ( $\gtrsim 90\%$ ) are smaller than 150 pc, and the uncertainties and deviations are comparable at least in  $\Delta A_G \geq 0.2$  mag.

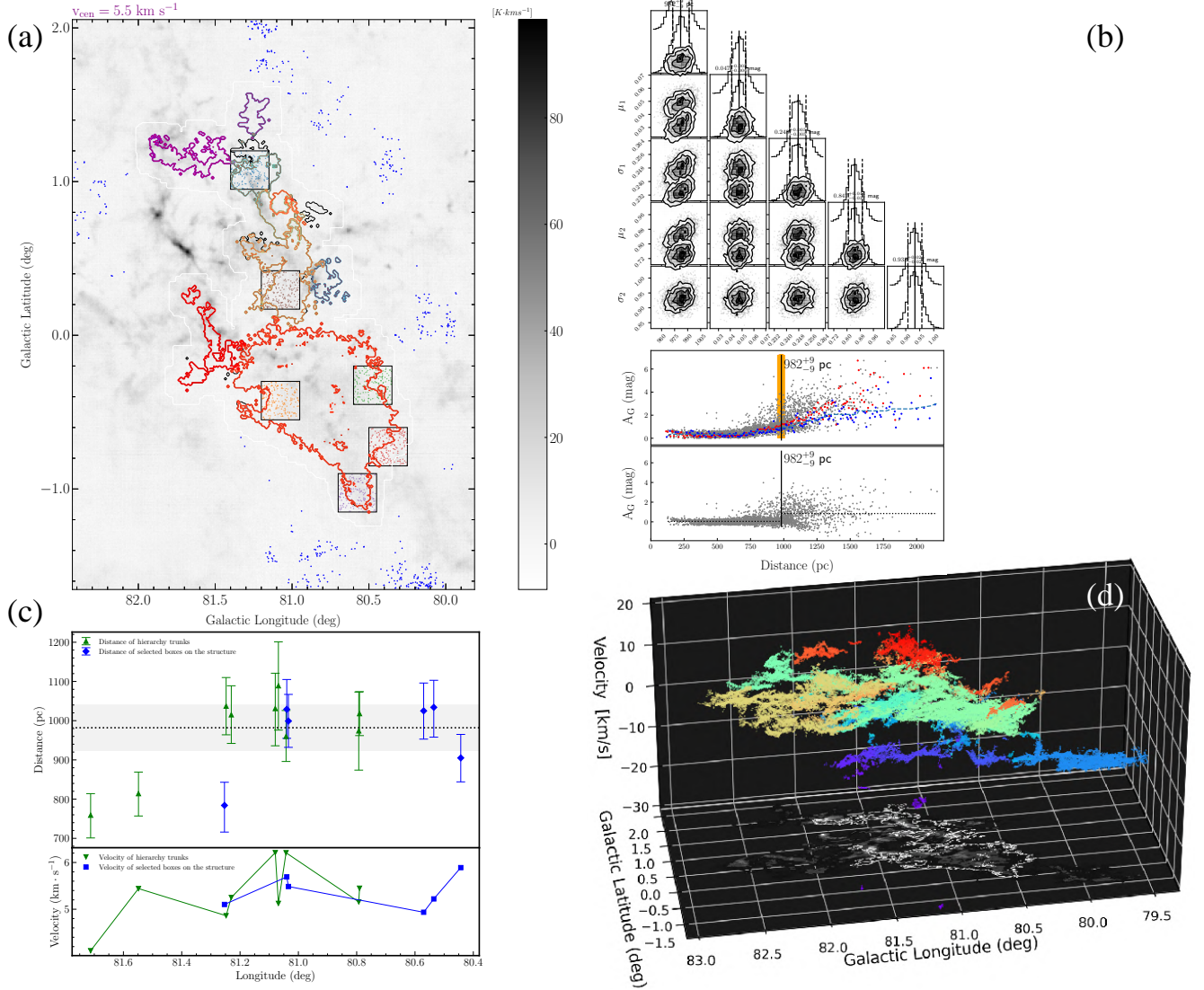


**Figure A1.** A validation of coherent structures (ID 118 in Table 1) identified by ACORNS based on Gaussian decomposition. We chose substructures of the large MC structure by manually marked boxes and hierarchical trunks (colored contours). Their distances are marked by blue squares and green triangles, respectively, while their confidence intervals (added 5% system error of Gaia) are denoted by error bars. The  $1\sigma$  confidence interval of distance is plotted in gray area of panel (c). In lower right panel, it is a 3D PPV scatter plot of centroid velocities of the cloud. All structures (other colors) overlaid with the cloud (in green) along LOS are also drawn, showing coherent velocity structures in PPV space.

These explain why almost all the samples have distance differences within 150 pc between the two models (A and B) when they detect the same jump point (see Section 4.2.2). It proves that, in current uncertainties of Gaia DR3, the *emcee* module provides robust results for the cloud distance measurement.

*Comparison with different sampling modules (emcee versus PyMC3).* *PyMC3* (Salvatier et al. 2016) module implicitly builds up a *Theano* function from the space of our parameters to their posterior probability density up to a constant factor. The probability distribution of  $A_G$  can be treated as a piecewise function. We use *SWITCH* function to describe the parameters in different intervals. In the sampling process, we use *Metropolis* sampler for jump point, and *NUTS* for the other four parameters (see Section 4). After 1000 draws, the returned objects *TRACE*, including posterior predictive samples, are generated from MCMC sampling. The median values from the above sampling are chosen as our results.

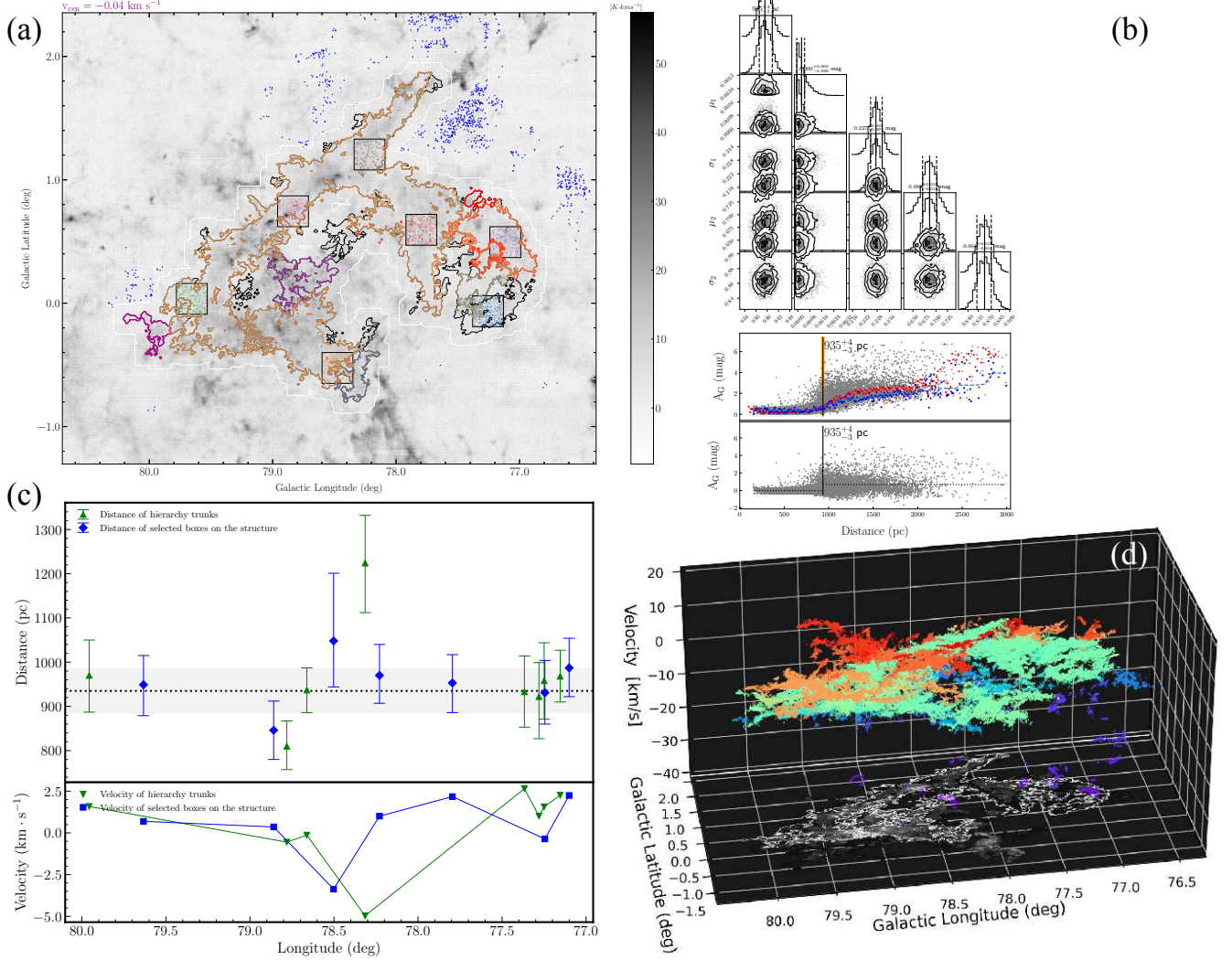


**Figure A2.** The same as Figure A1, but for MC L889 toward the Cygnus X South region.

In Figure B4a, we compare the distance measurement between *emcee* and *Pymc3* for clouds in Table 1. The distances by *emcee* are in good agreement with the posterior predictive samples produced by *Pymc3*. However, large discrepancies can be seen for some cases ( $\sim 10\%$ ).

Based on the 200 simulated samples (shown in Figure B4b), we find that *Pymc3* seems to work better than *emcee* on mock data. But the results from *Pymc3* match the mock data distances so closely with very small error bars, even when the jumps are not clear enough. This is actually caused by overfitting. Some results from *Pymc3* are not robust due to deviating from the preset distance out of uncertainties from sampling (see a case in blue box in Figure B4b). And a case detects multijump points (see red box in Figure B4b). Samplings from *Pymc3* are rather sensitive to small variations in  $A_G$ , and the detected jumps often deviate from the true value (by *emcee* or human judge). We thus choose *emcee* because it gives a more robust sampling result in application to real data by considering baseline fluctuations and  $A_G$  dispersion uncertainties.

### C. STAR DISTANCES ESTIMATED FROM PARALLAXES

In this work, we simply use MCMC sampling from the parallaxes of stars to estimate their distances. In comparison, we follow the method of Bailer-Jones (2015), Luri et al. (2018) to calculate median/uncertainty of the posterior based on the exponentially decreasing space density (EDSD) prior, the posterior of the UD prior, the method using naive inverse, and the transformation method (Smith & Eichhorn 1996).

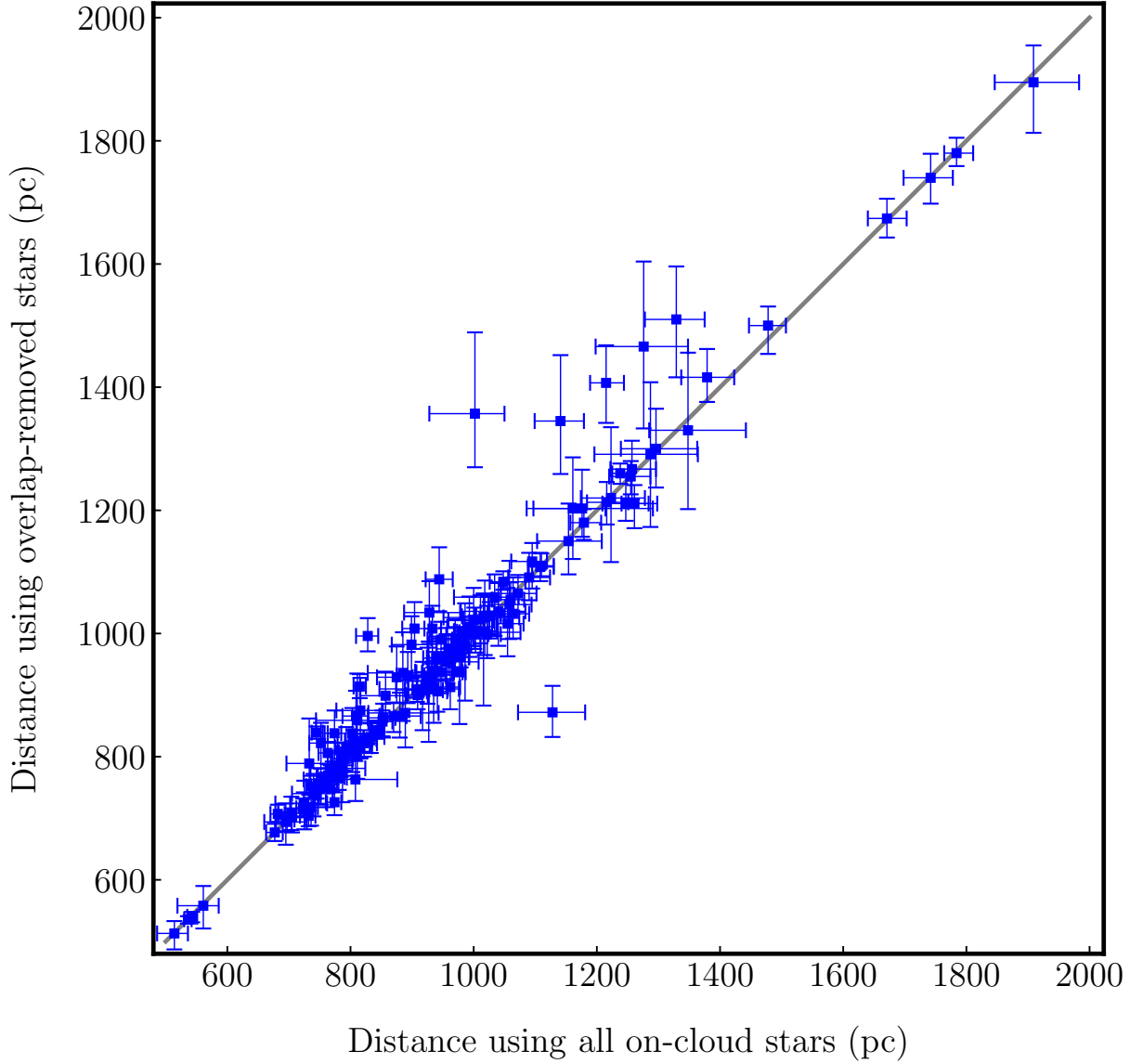


**Figure B1.** All on-cloud stars (red+black region in Figure 4) vs. overlap-removed on-cloud stars (red region in Figure 4).

The likelihood function of parallax ( $\varpi$ ), distance ( $r$ ), and uncertainty ( $\sigma$ ) is

$$P(\varpi | r, \sigma) = \frac{1}{\sqrt{2\pi}\sigma} \exp\left(-\frac{1}{2\sigma^2} \left(\varpi - \frac{1}{r}\right)^2\right) \quad (\text{C1})$$

The transformation Methods are applied by modifying the parallax  $\varpi$ :

$$r^* = \frac{1}{\varpi^*}, \quad \varpi^* = \beta\sigma\phi g_\phi \quad (\text{C2})$$

where

$$\phi = \frac{1}{0.8} \ln\left(1 + e^{\frac{0.8\varpi}{\sigma}}\right) \quad (\text{C3})$$

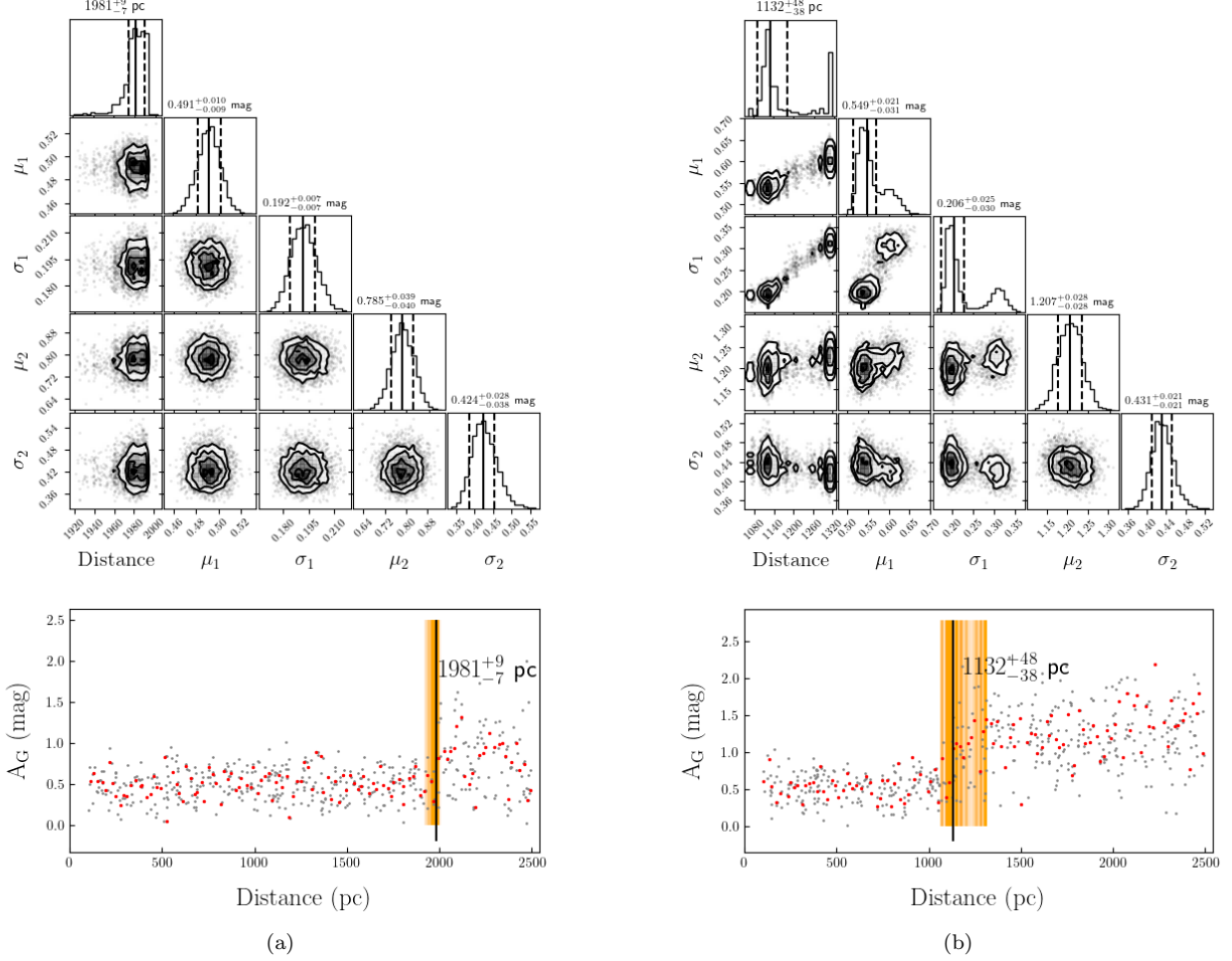


**Figure B2.** Two examples of measuring distance with mock data based on the Bayes model. Details in the panels can be seen in the caption of Figure 4, but points in lower panel are for the mock data.

and

$$\begin{cases} g_\phi = 1, & \varpi > 0, \\ g_\phi = e^{-0.605 \frac{\varpi^2}{\sigma^2}}, & \varpi \leq 0, \quad \beta = 1.01 \end{cases} \quad (\text{C4})$$

Therefore, the distance module  $\mu^*$  can be defined as

$$\mu^* = m - \hat{M} = -(5 \log(\hat{\varpi}) + 5) \quad (\text{C5})$$

Finally, the modified parallax  $\varpi$  satisfy

$$\hat{\varpi} = \beta \sigma \left( \frac{1}{e^\phi + e^{-\frac{5\varpi}{\sigma}}} + e^\phi \right) \quad (\text{C6})$$

Because our star samples are in a smaller parallax uncertainties ( $\leq 20\%$ ), the discrepancies between different methods can be ignored. Our distances are just like the naive inverse from parallaxes, but the median value and uncertainty are reproduced when we calculate the distance. The correlation of median distances and errors between different methods are presented in Figure C1.

#### D. INDIVIDUAL CASES IN COMPLICATED EXTINCTION ENVIRONMENT

In addition to the robust distance result confirmed by both Models A and B (class I), some cases failed to include enough field stars in Model A. For these clouds in the complicated extinction environment, we successfully measured

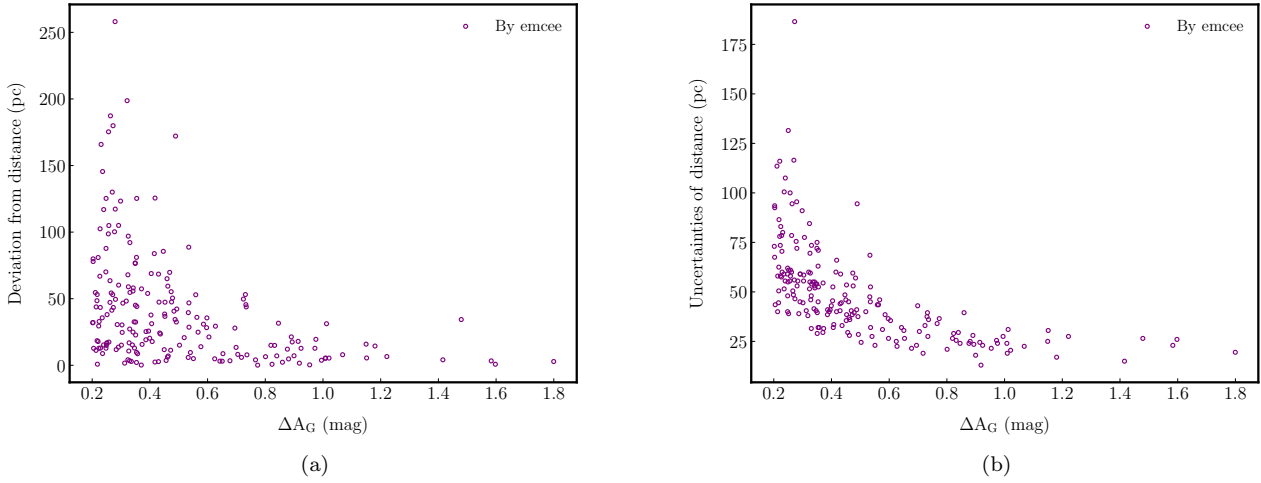


**Figure B3.** (a) Deviation between distances derived from emcee and preset distances in a relation with increasing  $\Delta A_G$ . (b) Uncertainties of distances derived from emcee in a relation with increasing  $\Delta A_G$ .

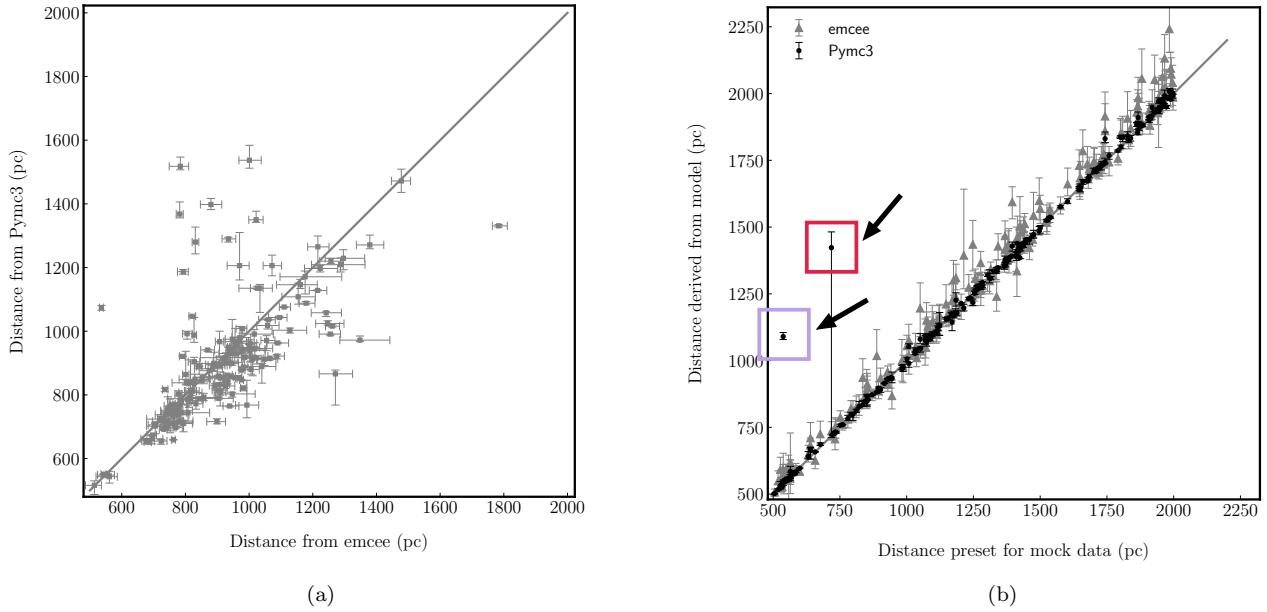


**Figure B4.** Comparison of distance measurements with different sampling modules. (a) The emcee module vs. Pymc3 module in our samples. (b) Distance derived from different modules vs. preset distance in mock data.

distances of 22 special cases by Model B because of the prominent extinction on the main body of the clouds. On the other hand, referenced stars near the measured clouds (see orange region in Figure 4b) may share the same but smaller background extinction along the LOS (see Figure 6b). We think distance measurements for these samples alone by Model B are also reliable.

From Figure D1, we can see these clouds match well with the identified gas layers in the text. More clouds with large-scale extensions are confirmed to be in the 1.3 kpc layer. In particular, toward the Cygnus X South region, these

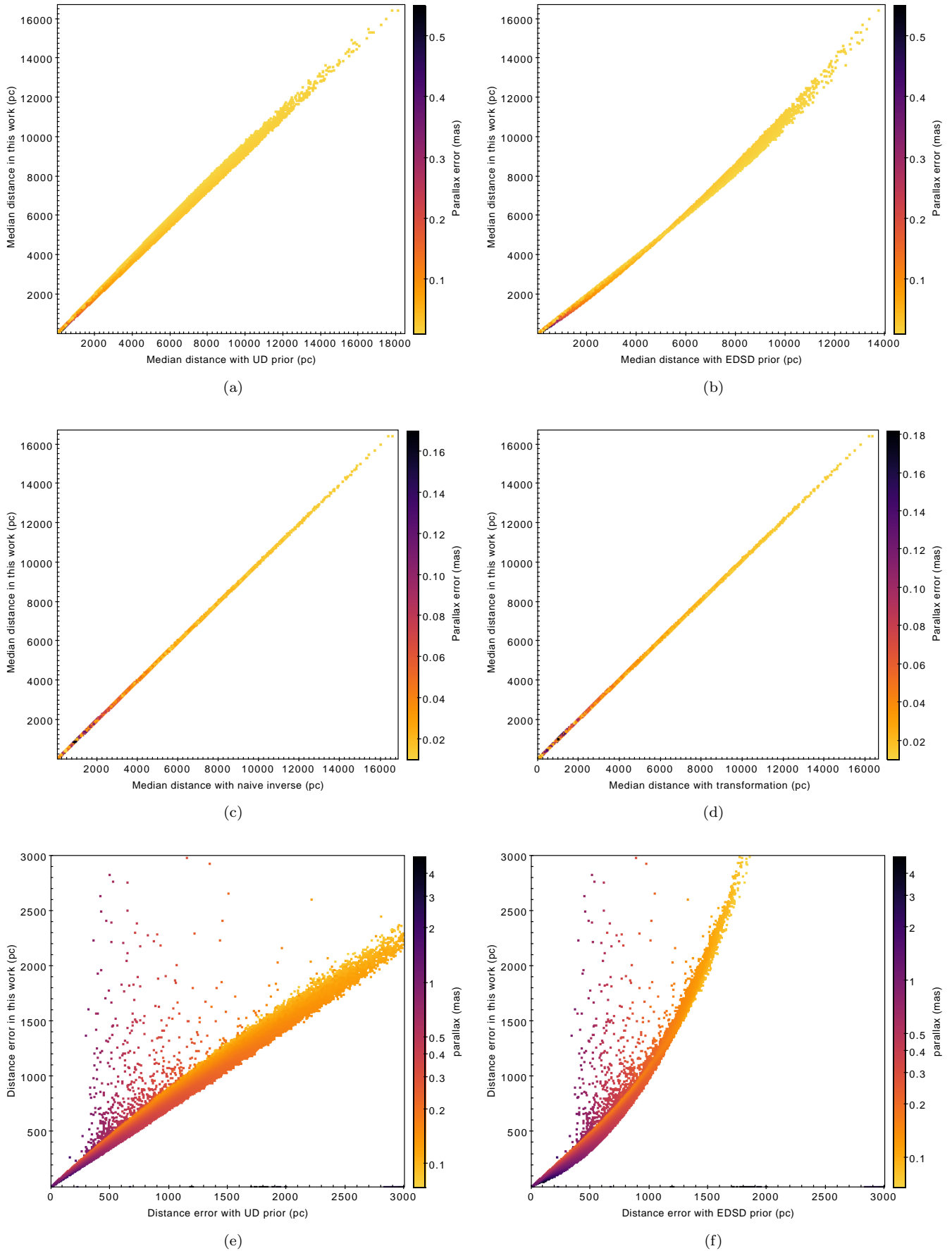
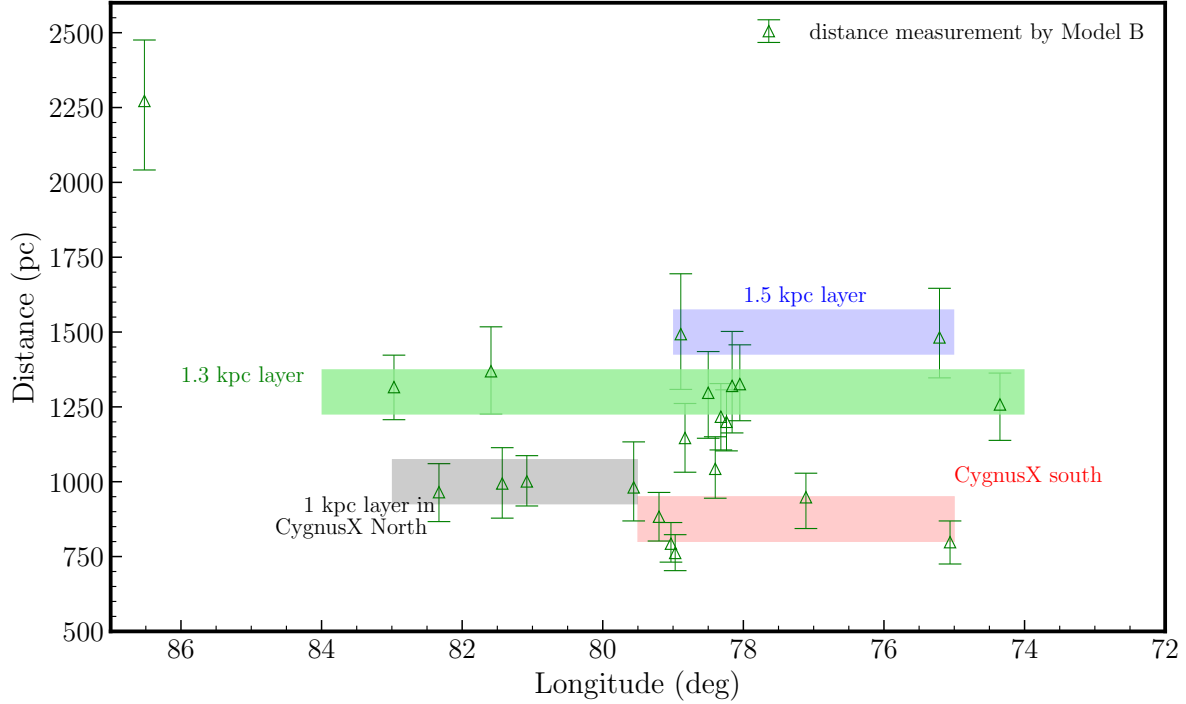


Figure C1. The median and uncertainty of distances derived by different methods compared to this work.

clouds have more of a contribution on masses, which is consistent with the 1.35 kpc overdensity in extinction of the Cygnus X South region (Dharmawardena et al. 2022).



**Figure D1.** Distances measured by Model B for those 22 clouds in complicated extinction environments. The colorful bands denote gas layers we identified previously.

### E. RETRIEVE PART OF FLUX LOSS DURING CLUSTERING

When we make a reconstruction using fully fledged clusters from ACORNS, a very small portion of the flux missed in the process of clustering. See panels (a) and (b) in Figure 2; the flux loss indicates some Gaussian components are dropped after clustering. We found the dropped components are mainly from three parts. The first is due to large amplitude error from Gaussian fitting. These components are excluded from catalog before the first loop in clustering. We do not retrieve those components, as it has little influence to the main structure of cloud. The second part is from the components isolated in spatial Euclidean distance or velocity. They could be false identifications by Gaussian fitting, while some are probably from line wings with smaller amplitudes. We drop them because they fail to meet our criteria for fledged clusters. Finally, some extra components are difficult for clustering because of the variance of centroid velocity and line width. We find these unassigned components are originated from Gaussian fitting and clustering processes. For some pixels, the overdecomposition in GaussPy+ might lead to failure of clustering with a uniform criteria.

We try to retrieve those unassigned components by adding another loop in the clustering process. Fully fledged clusters are already formed during the first three loops in the clustering process, so further development of the hierarchy is avoided. Next, we relax the criteria of velocity and line width to a large extent before the last loop, and remove the extra conditions when linking clusters. By using the same strategies of finding the most similar cluster in velocity and line width statistically, those unassigned components are merged into the nearest level of the hierarchy. To avoid developing the hierarchy and merging existing clusters together, we skip the “resolving ambiguities” method of ACORNS in the final loop we added, but restore the components with the smallest variation in equal weight of velocity and line width. Finally, an additional 1.5% flux is retrieved in our reconstruction map.

## F. YSO CANDIDATES TOWARD THE CYGNUS REGION

Our YSO candidates are selected based on infrared data collected from three surveys: the Spitzer Cygnus-X Legacy Survey (CXLS; Hora et al. 2009), the GLIMPSE360 program (Whitney et al. 2011), and the Wide-field Infrared Survey Explorer (WISE; Wright et al. 2010a) survey. We summarise the selection criteria here briefly for each data set, and the analysis of these YSOs will be presented in detail in a future paper (X.-L. Wang, et al. in preparation).

For the CXLS dataset, we select YSO candidates following the prescription in Gutermuth et al. (2009), but update the criteria with the new extinction law from Wang & Chen (2019). The new criteria are

- (1)  $[I2 - I3] > 0.7$  and  $[I1 - I2] > 0.7$ ;
- (2)  $[I2 - I4] - \sigma_{[I2-I4]} > 0.5$ ,  $[I1 - I3] - \sigma_{[I1-I3]} > 0.35$ ,  $[I1 - I2] - \sigma_{[I1-I2]} > 0.15$ , and  $[I1 - I3] - \sigma_{[I1-I3]} \leq 18 \times ([I2 - I4] - \sigma_{[I2-I4]} - 0.5) + 0.5$ ;
- (3)  $[K - I1]_0 - \sigma_{[K-I1]} > 0$ ,  $[I1 - I2]_0 - \sigma_{[I1-I2]} > 0.101$ , and  $[K - I1]_0 - \sigma_{[K-I1]} > -2.85714 \times ([I1 - I2]_0 - \sigma_{[I1-I2]} - 0.101) + 0.5$ ;
- (4)  $[I3 - M1] > 2.5$  for sources without  $I4$  measurements;
- (5)  $[I2 - M1] > 2.5$  for sources with no  $I3$  and  $I4$  measurements.

With these criteria, we selected 24,757 as YSO candidates.

For data from the GLIMPSE360 program, we select YSO candidates following Winston et al. (2020); again, the extinction law is updated with the Wang & Chen (2019) law. The new criteria are

- (1)  $0.9375 \times ([J - H] - 0.6 + \sigma_{[J-H]}) + 1.0 + \sigma_{[H-I2]} < [H - I2]$  and  $[J - H] > 0$ ;
- (2)  $0.9811 \times ([H - K] + \sigma_{[H-K]}) + 0.4 + \sigma_{[K-I2]} < [K - I2]$ ,  $[H - K] > 0$ , and  $[K - I2] > 0.2 + \sigma_{K-I2}$ ;
- (3)  $[I1 - I2]_0 - \sigma_{[I1-I2]} > 0$ ,  $[K - I1]_0 - \sigma_{[K-I1]} > 0.2 \times [I1 - I2]_0 + 0.3$ , and  $[K - I1]_0 - \sigma_{[K-I1]} > -([I1 - I2]_0 - \sigma_{[I1-I2]}) + 0.8$ .

With the above criteria, we select 6168 candidates.

For the WISE data, only the first two channels are used in the selection procedure. Since the first two WISE channels have a similar central wavelength as the first two IRAC bands, we utilize similar criteria as for the GLIMPSE360 data, but replace  $I1$  with  $W1$  and  $I2$  with  $W2$ . The selection criteria are

- (1)  $0.9375 \times ([J - H] - 0.6 + \sigma_{[J-H]}) + 1.0 + \sigma_{[H-W2]} < [H - W2]$  and  $[J - H] > 0$ ;
- (2)  $0.9811 \times ([H - K] + \sigma_{[H-K]}) + 0.4 + \sigma_{[K-W2]} < [K - W2]$ ,  $[H - K] > 0$ , and  $[K - W2] > 0.2 + \sigma_{[K-W2]}$ ;
- (3)  $[W1 - W2]_0 - \sigma_{[W1-W2]} > 0$ ,  $[K - W1]_0 - \sigma_{[K-W1]} > 0.2 \times [W1 - W2]_0 + 0.3$ , and  $[K - W1]_0 - \sigma_{[K-W1]} > -([W1 - W2]_0 - \sigma_{[W1-W2]}) + 0.8$ .

With the above criteria, we select 25,853 candidates.

These three lists of YSO candidates are combined, and the duplicates are removed, resulting in a total of 50,101 YSO candidates. In the current work, we are comparing the distribution of YSOs with  $^{13}\text{CO}$  traced molecular gas (as displayed in Figure F1 and details in discussion). Therefore, we focus on the subsample (22,158 candidates) that have Gaia parallaxes. Following Kuhn et al. (2020), possible giant star contaminants are removed, leaving 19,220 candidates in our FOV. Finally, 11,244 candidates are found to be within the interval  $[0.5, 3]$  kpc.

## REFERENCES

- Abbott, D. C., Bieging, J. H., & Churchwell, E. 1981, ApJ, 250, 645, doi: [10.1086/159412](https://doi.org/10.1086/159412)
- Adler, D. S., & Roberts, William W., J. 1992, ApJ, 384, 95, doi: [10.1086/170854](https://doi.org/10.1086/170854)
- Anderson, L. D., Bania, T. M., Balsaer, D. S., et al. 2014, ApJS, 212, 1, doi: [10.1088/0067-0049/212/1/1](https://doi.org/10.1088/0067-0049/212/1/1)
- Ando, K., Nagayama, T., Omodaka, T., et al. 2011, PASJ, 63, 45, doi: [10.1093/pasj/63.1.45](https://doi.org/10.1093/pasj/63.1.45)
- Andrae, R., Foesneau, M., Sordo, R., et al. 2023, A&A, 674, A27, doi: [10.1051/0004-6361/202243462](https://doi.org/10.1051/0004-6361/202243462)
- Astropy Collaboration, Robitaille, T. P., Tollerud, E. J., et al. 2013, A&A, 558, A33, doi: [10.1051/0004-6361/201322068](https://doi.org/10.1051/0004-6361/201322068)
- Astropy Collaboration, Price-Whelan, A. M., Sipőcz, B. M., et al. 2018, AJ, 156, 123, doi: [10.3847/1538-3881/aabc4f](https://doi.org/10.3847/1538-3881/aabc4f)
- Astropy Collaboration, Price-Whelan, A. M., Lim, P. L., et al. 2022, ApJ, 935, 167, doi: [10.3847/1538-4357/ac7c74](https://doi.org/10.3847/1538-4357/ac7c74)
- Bailer-Jones, C. A. L. 2015, PASP, 127, 994, doi: [10.1086/683116](https://doi.org/10.1086/683116)
- Banik, P., & Ghosh, S. K. 2022, ApJL, 931, L30, doi: [10.3847/2041-8213/ac7157](https://doi.org/10.3847/2041-8213/ac7157)
- Beaumont, C. N., Offner, S. S. R., Shetty, R., Glover, S. C. O., & Goodman, A. A. 2013, ApJ, 777, 173, doi: [10.1088/0004-637X/777/2/173](https://doi.org/10.1088/0004-637X/777/2/173)
- Beerer, I. M., Koenig, X. P., Hora, J. L., et al. 2010, ApJ, 720, 679, doi: [10.1088/0004-637X/720/1/679](https://doi.org/10.1088/0004-637X/720/1/679)

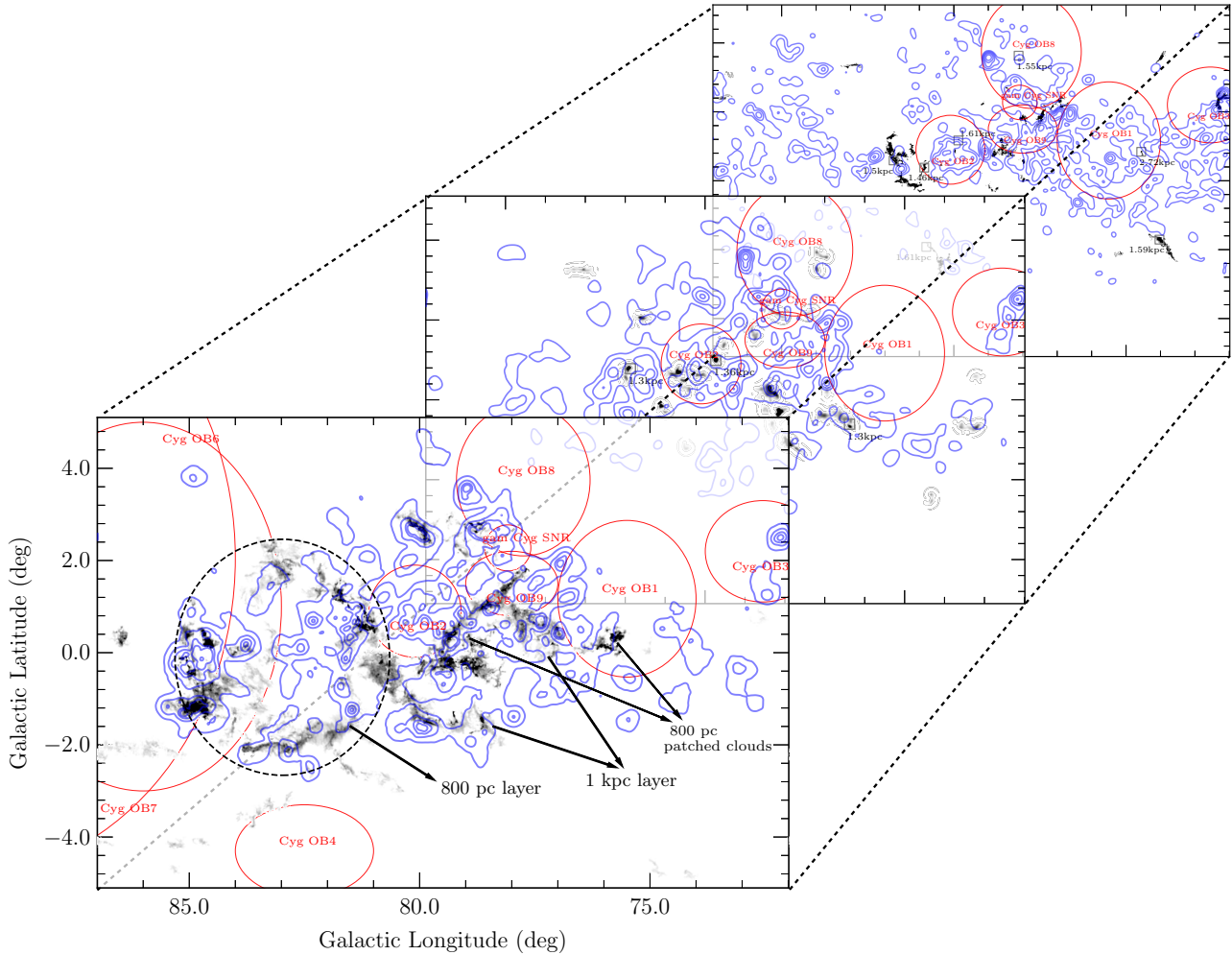


**Figure F1.** The multiple layers of gas structure with YSO candidates toward the Cygnus region. Similar to Figure 17, gray-scale maps are reconstructed by identified MC structures. The dashed ellipse shows a large-scale molecular loop with diameter of  $\sim 56$  pc at a distance of 800 pc. Red ellipses show OB associations and SNR, while boxes show the masers in Table 2. The overdensity of YSOs' candidates is shown as blue contours in each interval. The levels in different intervals are presented as follows:  $3\sigma$  to 99.5% of the maximum value with an increased step of 25% in a logarithm scale for [500, 1000] pc.  $3\sigma$  to 99.5% of the maximum value with an increased step of 20% in a logarithm scale for [1000, 1400] pc.  $10\sigma$  to 99.5% of the maximum value with an increased step of 20% in a logarithm scale for  $\geq 1400$  pc.  $\sigma$  ( $\sim 15 \text{ deg}^{-1}$ ) is the noise level of equivalent density map for each interval.

Berlanas, S. R., Wright, N. J., Herrero, A., Drew, J. E., & Lennon, D. J. 2019, *MNRAS*, 484, 1838, doi: [10.1093/mnras/stz117](https://doi.org/10.1093/mnras/stz117)

Beuther, H., Wyrowski, F., Menten, K. M., et al. 2022, *A&A*, 665, A63, doi: [10.1051/0004-6361/202244040](https://doi.org/10.1051/0004-6361/202244040)

Bolatto, A. D., Wolfire, M., & Leroy, A. K. 2013, *ARA&A*, 51, 207, doi: [10.1146/annurev-astro-082812-140944](https://doi.org/10.1146/annurev-astro-082812-140944)

Bonne, L., Bontemps, S., Schneider, N., et al. 2023, *ApJ*, 951, 39, doi: [10.3847/1538-4357/acd536](https://doi.org/10.3847/1538-4357/acd536)

Bontemps, S., Motte, F., Csengeri, T., & Schneider, N. 2010, *A&A*, 524, A18, doi: [10.1051/0004-6361/200913286](https://doi.org/10.1051/0004-6361/200913286)

Bourke, T. L., Garay, G., Lehtinen, K. K., et al. 1997, *ApJ*, 476, 781, doi: [10.1086/303642](https://doi.org/10.1086/303642)

Bron, E., Daudon, C., Pety, J., et al. 2018, *A&A*, 610, A12, doi: [10.1051/0004-6361/201731833](https://doi.org/10.1051/0004-6361/201731833)

Burns, R. A., Yamaguchi, Y., Handa, T., et al. 2014, *PASJ*, 66, 102, doi: [10.1093/pasj/psu094](https://doi.org/10.1093/pasj/psu094)

Cai, J.-J., Yang, J., Zheng, S., et al. 2021, *Research in Astronomy and Astrophysics*, 21, 304, doi: [10.1088/1674-4527/21/12/304](https://doi.org/10.1088/1674-4527/21/12/304)

Cao, Y., Qiu, K., Zhang, Q., & Li, G.-X. 2022, *ApJ*, 927, 106, doi: [10.3847/1538-4357/ac4696](https://doi.org/10.3847/1538-4357/ac4696)

- Cao, Y., Qiu, K., Zhang, Q., et al. 2019, *ApJS*, 241, 1, doi: [10.3847/1538-4365/ab0025](https://doi.org/10.3847/1538-4365/ab0025)
- Cao, Z., Aharonian, F. A., An, Q., et al. 2021, *Nature*, 594, 33, doi: [10.1038/s41586-021-03498-z](https://doi.org/10.1038/s41586-021-03498-z)
- Cao, Z., Aharonian, F., An, Q., et al. 2024, *ApJS*, 271, 25, doi: [10.3847/1538-4365/acfd29](https://doi.org/10.3847/1538-4365/acfd29)
- Chen, B. Q., Huang, Y., Yuan, H. B., et al. 2019, *MNRAS*, 483, 4277, doi: [10.1093/mnras/sty3341](https://doi.org/10.1093/mnras/sty3341)
- Clarke, S. D., Whitworth, A. P., Spowage, R. L., et al. 2018, *MNRAS*, 479, 1722, doi: [10.1093/mnras/sty1675](https://doi.org/10.1093/mnras/sty1675)
- Colombo, D., Rosolowsky, E., Duarte-Cabral, A., et al. 2019, *MNRAS*, 483, 4291, doi: [10.1093/mnras/sty3283](https://doi.org/10.1093/mnras/sty3283)
- Comerón, F., Djupvik, A. A., Schneider, N., & Pasquali, A. 2020, *A&A*, 644, A62, doi: [10.1051/0004-6361/202039188](https://doi.org/10.1051/0004-6361/202039188)
- Comerón, F., Pasquali, A., Rodighiero, G., et al. 2002, *A&A*, 389, 874, doi: [10.1051/0004-6361:20020648](https://doi.org/10.1051/0004-6361:20020648)
- Creevey, O. L., Sordo, R., Pailler, F., et al. 2023, *A&A*, 674, A26, doi: [10.1051/0004-6361/202243688](https://doi.org/10.1051/0004-6361/202243688)
- Dame, T. M., Hartmann, D., & Thaddeus, P. 2001, *ApJ*, 547, 792, doi: [10.1086/318388](https://doi.org/10.1086/318388)
- Dame, T. M., & Thaddeus, P. 1985, *ApJ*, 297, 751, doi: [10.1086/163573](https://doi.org/10.1086/163573)
- Dame, T. M., Ungerechts, H., Cohen, R. S., et al. 1987, *ApJ*, 322, 706, doi: [10.1086/165766](https://doi.org/10.1086/165766)
- De Angeli, F., Weiler, M., Montegriffo, P., et al. 2023, *A&A*, 674, A2, doi: [10.1051/0004-6361/202243680](https://doi.org/10.1051/0004-6361/202243680)
- de Leeuw, J. 1977, *Psychometrika*, 42, 141, doi: [10.1007/BF02293750](https://doi.org/10.1007/BF02293750)
- Dharmawardena, T. E., Bailer-Jones, C. A. L., Fouesneau, M., & Foreman-Mackey, D. 2022, *A&A*, 658, A166, doi: [10.1051/0004-6361/202141298](https://doi.org/10.1051/0004-6361/202141298)
- Downes, D., & Rinehart, R. 1966, *ApJ*, 144, 937, doi: [10.1086/148691](https://doi.org/10.1086/148691)
- Duarte-Cabral, A., Bontemps, S., Motte, F., et al. 2013, *A&A*, 558, A125, doi: [10.1051/0004-6361/201321393](https://doi.org/10.1051/0004-6361/201321393)
- Duarte-Cabral, A., Colombo, D., Urquhart, J. S., et al. 2021, *MNRAS*, 500, 3027, doi: [10.1093/mnras/staa2480](https://doi.org/10.1093/mnras/staa2480)
- Egan, M. P., Shipman, R. F., Price, S. D., et al. 1998, *ApJL*, 494, L199, doi: [10.1086/311198](https://doi.org/10.1086/311198)
- Fang, M., Hillenbrand, L. A., Kim, J. S., et al. 2020, *ApJ*, 904, 146, doi: [10.3847/1538-4357/abba84](https://doi.org/10.3847/1538-4357/abba84)
- Fitzpatrick, E. L. 1999, *PASP*, 111, 63, doi: [10.1086/316293](https://doi.org/10.1086/316293)
- Foreman-Mackey, D., Hogg, D. W., Lang, D., & Goodman, J. 2013, *PASP*, 125, 306, doi: [10.1086/670067](https://doi.org/10.1086/670067)
- Frerking, M. A., Langer, W. D., & Wilson, R. W. 1982, *ApJ*, 262, 590, doi: [10.1086/160451](https://doi.org/10.1086/160451)
- Ginsburg, A., & Mirocha, J. 2011, *PySpecKit: Python Spectroscopic Toolkit*, Astrophysics Source Code Library, record ascl:1109.001. <http://ascl.net/1109.001>
- Ginsburg, A., Sokolov, V., de Val-Borro, M., et al. 2022, *AJ*, 163, 291, doi: [10.3847/1538-3881/ac695a](https://doi.org/10.3847/1538-3881/ac695a)
- Goldsmith, P. F., Heyer, M., Narayanan, G., et al. 2008, *ApJ*, 680, 428, doi: [10.1086/587166](https://doi.org/10.1086/587166)
- Gong, Y., Ortiz-León, G. N., Rugel, M. R., et al. 2023, *A&A*, 678, A130, doi: [10.1051/0004-6361/202346102](https://doi.org/10.1051/0004-6361/202346102)
- Gottschalk, M., Kothes, R., Matthews, H. E., Landecker, T. L., & Dent, W. R. F. 2012, *A&A*, 541, A79, doi: [10.1051/0004-6361/201118600](https://doi.org/10.1051/0004-6361/201118600)
- Gratier, P., Pety, J., Bron, E., et al. 2021, *A&A*, 645, A27, doi: [10.1051/0004-6361/202037871](https://doi.org/10.1051/0004-6361/202037871)
- Green, G. M., Schlafly, E., Zucker, C., Speagle, J. S., & Finkbeiner, D. 2019, *ApJ*, 887, 93, doi: [10.3847/1538-4357/ab5362](https://doi.org/10.3847/1538-4357/ab5362)
- Guo, H. L., Chen, B. Q., & Liu, X. W. 2022, *MNRAS*, 511, 2302, doi: [10.1093/mnras/stac213](https://doi.org/10.1093/mnras/stac213)
- Gutermuth, R. A., Megeath, S. T., Myers, P. C., et al. 2009, *ApJS*, 184, 18, doi: [10.1088/0067-0049/184/1/18](https://doi.org/10.1088/0067-0049/184/1/18)
- Hacar, A., Tafalla, M., Kauffmann, J., & Kovács, A. 2013, *A&A*, 554, A55, doi: [10.1051/0004-6361/201220090](https://doi.org/10.1051/0004-6361/201220090)
- Hanson, M. M. 2003, *ApJ*, 597, 957, doi: [10.1086/378508](https://doi.org/10.1086/378508)
- Hennemann, M., Motte, F., Schneider, N., et al. 2012, *A&A*, 543, L3, doi: [10.1051/0004-6361/201219429](https://doi.org/10.1051/0004-6361/201219429)
- Henshaw, J. D., Ginsburg, A., Haworth, T. J., et al. 2019, *MNRAS*, 485, 2457, doi: [10.1093/mnras/stz471](https://doi.org/10.1093/mnras/stz471)
- Henshaw, J. D., Kruijssen, J. M. D., Longmore, S. N., et al. 2020, *Nature Astronomy*, 4, 1064, doi: [10.1038/s41550-020-1126-z](https://doi.org/10.1038/s41550-020-1126-z)
- Heyer, M., & Dame, T. M. 2015, *ARA&A*, 53, 583, doi: [10.1146/annurev-astro-082214-122324](https://doi.org/10.1146/annurev-astro-082214-122324)
- Higgs, L. A., Wendker, H. J., & Landecker, T. L. 1994, *A&A*, 291, 295
- Hiltner, W. A., & Johnson, H. L. 1956, *ApJ*, 124, 367, doi: [10.1086/146231](https://doi.org/10.1086/146231)
- Hora, J. L., Bontemps, S., Megeath, S. T., et al. 2009, in *American Astronomical Society Meeting Abstracts*, Vol. 213, American Astronomical Society Meeting Abstracts #213, 356.01
- Hottier, C., Babusiaux, C., & Arenou, F. 2020, *A&A*, 641, A79, doi: [10.1051/0004-6361/202037573](https://doi.org/10.1051/0004-6361/202037573)
- Hunter, J. D. 2007, *Computing in Science and Engineering*, 9, 90, doi: [10.1109/MCSE.2007.55](https://doi.org/10.1109/MCSE.2007.55)
- Knödlseeder, J. 2000, *A&A*, 360, 539, doi: [10.48550/arXiv.astro-ph/0007442](https://doi.org/10.48550/arXiv.astro-ph/0007442)
- Kruskal, J. B. 1964, *Psychometrika*, 29, 115, doi: [10.1007/BF02289694](https://doi.org/10.1007/BF02289694)
- Kuhn, M. A., & Hillenbrand, L. A. 2020, *Research Notes of the American Astronomical Society*, 4, 224, doi: [10.3847/2515-5172/abd18a](https://doi.org/10.3847/2515-5172/abd18a)

- Kuhn, M. A., Hillenbrand, L. A., Carpenter, J. M., & Avelar Menendez, A. R. 2020, *ApJ*, 899, 128, doi: [10.3847/1538-4357/aba19a](https://doi.org/10.3847/1538-4357/aba19a)
- Lallement, R., Babusiaux, C., Vergely, J. L., et al. 2019, *A&A*, 625, A135, doi: [10.1051/0004-6361/201834695](https://doi.org/10.1051/0004-6361/201834695)
- LHAASO Collaboration. 2024, *Science Bulletin*, 69, 449, doi: [10.1016/j.scib.2023.12.040](https://doi.org/10.1016/j.scib.2023.12.040)
- Li, C., Wang, H., Zhang, M., et al. 2018, *ApJS*, 238, 10, doi: [10.3847/1538-4365/aad963](https://doi.org/10.3847/1538-4365/aad963)
- Luri, X., Brown, A. G. A., Sarro, L. M., et al. 2018, *A&A*, 616, A9, doi: [10.1051/0004-6361/201832964](https://doi.org/10.1051/0004-6361/201832964)
- Ma, Y., Wang, H., Li, C., et al. 2021, *ApJS*, 254, 3, doi: [10.3847/1538-4365/abe85c](https://doi.org/10.3847/1538-4365/abe85c)
- Marchal, A., Miville-Deschênes, M.-A., Orioux, F., et al. 2019, *A&A*, 626, A101, doi: [10.1051/0004-6361/201935335](https://doi.org/10.1051/0004-6361/201935335)
- Massey, P., & Thompson, A. B. 1991, *AJ*, 101, 1408, doi: [10.1086/115774](https://doi.org/10.1086/115774)
- Mertsch, P., & Vittino, A. 2021, *A&A*, 655, A64, doi: [10.1051/0004-6361/202141000](https://doi.org/10.1051/0004-6361/202141000)
- Milam, S. N., Savage, C., Brewster, M. A., Ziurys, L. M., & Wyckoff, S. 2005, *ApJ*, 634, 1126, doi: [10.1086/497123](https://doi.org/10.1086/497123)
- Miville-Deschênes, M.-A., Murray, N., & Lee, E. J. 2017, *ApJ*, 834, 57, doi: [10.3847/1538-4357/834/1/57](https://doi.org/10.3847/1538-4357/834/1/57)
- Moscadelli, L., Cesaroni, R., Rioja, M. J., Dodson, R., & Reid, M. J. 2011, *A&A*, 526, A66, doi: [10.1051/0004-6361/201015641](https://doi.org/10.1051/0004-6361/201015641)
- Motte, F., Bontemps, S., Schilke, P., et al. 2007, *A&A*, 476, 1243, doi: [10.1051/0004-6361:20077843](https://doi.org/10.1051/0004-6361:20077843)
- Nagahama, T., Mizuno, A., Ogawa, H., & Fukui, Y. 1998, *AJ*, 116, 336, doi: [10.1086/300392](https://doi.org/10.1086/300392)
- Nagayama, T., Omodaka, T., Handa, T., et al. 2015, *PASJ*, 67, 66, doi: [10.1093/pasj/psu133](https://doi.org/10.1093/pasj/psu133)
- Orellana, R. B., De Biasi, M. S., & Paíz, L. G. 2021, *MNRAS*, 502, 6080, doi: [10.1093/mnras/stab457](https://doi.org/10.1093/mnras/stab457)
- Ortiz-León, G. N., Menten, K. M., Brunthaler, A., et al. 2021, *A&A*, 651, A87, doi: [10.1051/0004-6361/202140817](https://doi.org/10.1051/0004-6361/202140817)
- Pan, H.-A., Fujimoto, Y., Tasker, E. J., et al. 2015, *MNRAS*, 453, 3082, doi: [10.1093/mnras/stv1843](https://doi.org/10.1093/mnras/stv1843)
- Panopoulou, G. V., & Lenz, D. 2020, *ApJ*, 902, 120, doi: [10.3847/1538-4357/abb6f5](https://doi.org/10.3847/1538-4357/abb6f5)
- Pedregosa, F., Varoquaux, G., Gramfort, A., et al. 2011, *Journal of Machine Learning Research*, 12, 2825, doi: [10.48550/arXiv.1201.0490](https://doi.org/10.48550/arXiv.1201.0490)
- Peek, J. E. G., Tchernyshyov, K., & Miville-Deschenes, M.-A. 2022, *ApJ*, 925, 201, doi: [10.3847/1538-4357/ac3f34](https://doi.org/10.3847/1538-4357/ac3f34)
- Petzler, A., Dawson, J. R., & Wardle, M. 2021, *ApJ*, 923, 261, doi: [10.3847/1538-4357/ac2f42](https://doi.org/10.3847/1538-4357/ac2f42)
- Pineda, J. L., Goldsmith, P. F., Chapman, N., et al. 2010, *ApJ*, 721, 686, doi: [10.1088/0004-637X/721/1/686](https://doi.org/10.1088/0004-637X/721/1/686)
- Quintana, A. L., & Wright, N. J. 2021, *MNRAS*, 508, 2370, doi: [10.1093/mnras/stab2663](https://doi.org/10.1093/mnras/stab2663)
- . 2022, *MNRAS*, 515, 687, doi: [10.1093/mnras/stac1526](https://doi.org/10.1093/mnras/stac1526)
- Rastorguev, A. S., Zabolotskikh, M. V., Sitnik, T. G., et al. 2023, *Astrophysical Bulletin*, 78, 119, doi: [10.1134/S1990341323020050](https://doi.org/10.1134/S1990341323020050)
- Reid, M. J., Menten, K. M., Brunthaler, A., et al. 2019, *ApJ*, 885, 131, doi: [10.3847/1538-4357/ab4a11](https://doi.org/10.3847/1538-4357/ab4a11)
- Reipurth, B., & Schneider, N. 2008, in *Handbook of Star Forming Regions*, Volume I, ed. B. Reipurth, Vol. 4, 36
- Rice, T. S., Goodman, A. A., Bergin, E. A., Beaumont, C., & Dame, T. M. 2016, *ApJ*, 822, 52, doi: [10.3847/0004-637X/822/1/52](https://doi.org/10.3847/0004-637X/822/1/52)
- Riener, M., Kainulainen, J., Beuther, H., et al. 2020, *A&A*, 633, A14, doi: [10.1051/0004-6361/201936814](https://doi.org/10.1051/0004-6361/201936814)
- Riener, M., Kainulainen, J., Henshaw, J. D., et al. 2019, *A&A*, 628, A78, doi: [10.1051/0004-6361/201935519](https://doi.org/10.1051/0004-6361/201935519)
- Rygl, K., Brunthaler, A., Menten, K. M., et al. 2010, in *10th European VLBI Network Symposium and EVN Users Meeting: VLBI and the New Generation of Radio Arrays*, Vol. 10, 103, doi: [10.22323/1.125.0103](https://doi.org/10.22323/1.125.0103)
- Rygl, K. L. J., Brunthaler, A., Sanna, A., et al. 2012, *A&A*, 539, A79, doi: [10.1051/0004-6361/201118211](https://doi.org/10.1051/0004-6361/201118211)
- Salvatier, J., Wieckiâ, T. V., & Fonnesbeck, C. 2016, *PyMC3: Python probabilistic programming framework*, *Astrophysics Source Code Library*, record ascl:1610.016. <http://ascl.net/1610.016>
- Schneider, N., Bontemps, S., Simon, R., et al. 2006, *A&A*, 458, 855, doi: [10.1051/0004-6361:20065088](https://doi.org/10.1051/0004-6361:20065088)
- Schneider, N., Csengeri, T., Bontemps, S., et al. 2010, *A&A*, 520, A49, doi: [10.1051/0004-6361/201014481](https://doi.org/10.1051/0004-6361/201014481)
- Schneider, N., Simon, R., Bontemps, S., Comerón, F., & Motte, F. 2007, *A&A*, 474, 873, doi: [10.1051/0004-6361:20077540](https://doi.org/10.1051/0004-6361:20077540)
- Schneider, N., Bontemps, S., Motte, F., et al. 2016, *A&A*, 591, A40, doi: [10.1051/0004-6361/201628328](https://doi.org/10.1051/0004-6361/201628328)
- Schneider, N., Bonne, L., Bontemps, S., et al. 2023, *Nature Astronomy*, doi: [10.1038/s41550-023-01901-5](https://doi.org/10.1038/s41550-023-01901-5)
- Schuller, F., Csengeri, T., Urquhart, J. S., et al. 2017, *A&A*, 601, A124, doi: [10.1051/0004-6361/201628933](https://doi.org/10.1051/0004-6361/201628933)
- Shan, W., Yang, J., Shi, S., et al. 2012, *IEEE Transactions on Terahertz Science and Technology*, 2, 593, doi: [10.1109/TTHZ.2012.2213818](https://doi.org/10.1109/TTHZ.2012.2213818)
- Shetty, R., Collins, D. C., Kauffmann, J., et al. 2010, *ApJ*, 712, 1049, doi: [10.1088/0004-637X/712/2/1049](https://doi.org/10.1088/0004-637X/712/2/1049)
- Smith, Haywood, J., & Eichhorn, H. 1996, *MNRAS*, 281, 211, doi: [10.1093/mnras/281.1.211](https://doi.org/10.1093/mnras/281.1.211)

- Sokolov, V., Pineda, J. E., Buchner, J., & Caselli, P. 2020, *ApJL*, 892, L32, doi: [10.3847/2041-8213/ab8018](https://doi.org/10.3847/2041-8213/ab8018)
- Staudte, H. J., Lenzen, R., Dyck, H. M., & Schmidt, G. D. 1982, *ApJ*, 255, 95, doi: [10.1086/159807](https://doi.org/10.1086/159807)
- Straizys, V., Kazlauskas, A., Vansevicius, V., & Cernis, K. 1993, *Baltic Astronomy*, 2, 171, doi: [10.1515/astro-1993-0202](https://doi.org/10.1515/astro-1993-0202)
- Su, Y., Yang, J., Zhang, S., et al. 2019, *ApJS*, 240, 9, doi: [10.3847/1538-4365/aaf1c8](https://doi.org/10.3847/1538-4365/aaf1c8)
- Su, Y., Yang, J., Yan, Q.-Z., et al. 2020, *ApJ*, 893, 91, doi: [10.3847/1538-4357/ab7fff](https://doi.org/10.3847/1538-4357/ab7fff)
- Sun, L., Chen, X., Fang, M., et al. 2024, *AJ*, 167, 176, doi: [10.3847/1538-3881/ad2ea3](https://doi.org/10.3847/1538-3881/ad2ea3)
- Sun, M., Jiang, B., Zhao, H., & Ren, Y. 2021a, *ApJS*, 256, 46, doi: [10.3847/1538-4365/ac1601](https://doi.org/10.3847/1538-4365/ac1601)
- Sun, Y., Yang, J., Yan, Q.-Z., et al. 2021b, *ApJS*, 256, 32, doi: [10.3847/1538-4365/ac11fe](https://doi.org/10.3847/1538-4365/ac11fe)
- Takekoshi, T., Fujita, S., Nishimura, A., et al. 2019, *ApJ*, 883, 156, doi: [10.3847/1538-4357/ab3a55](https://doi.org/10.3847/1538-4357/ab3a55)
- Umemoto, T., Minamidani, T., Kuno, N., et al. 2017, *PASJ*, 69, 78, doi: [10.1093/pasj/psx061](https://doi.org/10.1093/pasj/psx061)
- Wang, C., Feng, H., Yang, J., et al. 2023, *AJ*, 165, 106, doi: [10.3847/1538-3881/acafee](https://doi.org/10.3847/1538-3881/acafee)
- Wang, S., & Chen, X. 2019, *ApJ*, 877, 116, doi: [10.3847/1538-4357/ab1c61](https://doi.org/10.3847/1538-4357/ab1c61)
- Wendker, H. J., Higgs, L. A., & Landecker, T. L. 1991, *A&A*, 241, 551
- Whitney, B., Benjamin, R., Meade, M., et al. 2011, in *American Astronomical Society Meeting Abstracts*, Vol. 217, American Astronomical Society Meeting Abstracts #217, 241.16
- Wilson, T. L., Rohlfs, K., & Hüttemeister, S. 2009, *Tools of Radio Astronomy*, doi: [10.1007/978-3-540-85122-6](https://doi.org/10.1007/978-3-540-85122-6)
- Winston, E., Hora, J. L., & Tolls, V. 2020, *AJ*, 160, 68, doi: [10.3847/1538-3881/ab99c8](https://doi.org/10.3847/1538-3881/ab99c8)
- Wright, E. L., Eisenhardt, P. R. M., Mainzer, A. K., et al. 2010a, *AJ*, 140, 1868, doi: [10.1088/0004-6256/140/6/1868](https://doi.org/10.1088/0004-6256/140/6/1868)
- Wright, N. J., Drake, J. J., Drew, J. E., & Vink, J. S. 2010b, *ApJ*, 713, 871, doi: [10.1088/0004-637X/713/2/871](https://doi.org/10.1088/0004-637X/713/2/871)
- Wright, N. J., Drew, J. E., & Mohr-Smith, M. 2015, *MNRAS*, 449, 741, doi: [10.1093/mnras/stv323](https://doi.org/10.1093/mnras/stv323)
- Xu, Y., Li, J. J., Reid, M. J., et al. 2013, *ApJ*, 769, 15, doi: [10.1088/0004-637X/769/1/15](https://doi.org/10.1088/0004-637X/769/1/15)
- Xu, Y., Reid, M., Dame, T., et al. 2016, *Science Advances*, 2, e1600878, doi: [10.1126/sciadv.1600878](https://doi.org/10.1126/sciadv.1600878)
- Yamagishi, M., Nishimura, A., Fujita, S., et al. 2018, *ApJS*, 235, 9, doi: [10.3847/1538-4365/aaab4b](https://doi.org/10.3847/1538-4365/aaab4b)
- Yan, Q.-Z., Yang, J., Su, Y., Sun, Y., & Wang, C. 2020, *ApJ*, 898, 80, doi: [10.3847/1538-4357/ab9f9c](https://doi.org/10.3847/1538-4357/ab9f9c)
- Yan, Q.-Z., Yang, J., Su, Y., et al. 2021a, *ApJ*, 922, 8, doi: [10.3847/1538-4357/ac214f](https://doi.org/10.3847/1538-4357/ac214f)
- Yan, Q.-Z., Yang, J., Sun, Y., Su, Y., & Xu, Y. 2019a, *ApJ*, 885, 19, doi: [10.3847/1538-4357/ab458e](https://doi.org/10.3847/1538-4357/ab458e)
- Yan, Q.-Z., Yang, J., Sun, Y., et al. 2021b, *A&A*, 645, A129, doi: [10.1051/0004-6361/202039768](https://doi.org/10.1051/0004-6361/202039768)
- Yan, Q.-Z., Yang, J., Yang, S., Sun, Y., & Wang, C. 2021c, *ApJ*, 910, 109, doi: [10.3847/1538-4357/abe628](https://doi.org/10.3847/1538-4357/abe628)
- Yan, Q.-Z., Zhang, B., Xu, Y., et al. 2019b, *A&A*, 624, A6, doi: [10.1051/0004-6361/201834337](https://doi.org/10.1051/0004-6361/201834337)
- Yu, B., Chen, B. Q., Jiang, B. W., & Zijlstra, A. 2019, *MNRAS*, 488, 3129, doi: [10.1093/mnras/stz1940](https://doi.org/10.1093/mnras/stz1940)
- Yuan, L., Yang, J., Du, F., et al. 2022, *ApJS*, 261, 37, doi: [10.3847/1538-4365/ac739f](https://doi.org/10.3847/1538-4365/ac739f)
- . 2023, *ApJ*, 958, 7, doi: [10.3847/1538-4357/acf9ef](https://doi.org/10.3847/1538-4357/acf9ef)
- Zamora-Avilés, M., Ballesteros-Paredes, J., & Hartmann, L. W. 2017, *MNRAS*, 472, 647, doi: [10.1093/mnras/stx1995](https://doi.org/10.1093/mnras/stx1995)
- Zhang, B., Reid, M. J., Menten, K. M., Zheng, X. W., & Brunthaler, A. 2012, *A&A*, 544, A42, doi: [10.1051/0004-6361/201219587](https://doi.org/10.1051/0004-6361/201219587)
- Zhang, S., Xu, Y., & Yang, J. 2014, *AJ*, 147, 46, doi: [10.1088/0004-6256/147/3/46](https://doi.org/10.1088/0004-6256/147/3/46)
- Zhang, S., Yang, J., Xu, Y., et al. 2020, *ApJS*, 248, 15, doi: [10.3847/1538-4365/ab879a](https://doi.org/10.3847/1538-4365/ab879a)
- Zhao, H., Jiang, B., Li, J., et al. 2020, *ApJ*, 891, 137, doi: [10.3847/1538-4357/ab75ef](https://doi.org/10.3847/1538-4357/ab75ef)
- Zucker, C., Alves, J., Goodman, A., Meingast, S., & Galli, P. 2023, in *Astronomical Society of the Pacific Conference Series*, Vol. 534, Protostars and Planets VII, ed. S. Inutsuka, Y. Aikawa, T. Muto, K. Tomida, & M. Tamura, 43, doi: [10.48550/arXiv.2212.00067](https://doi.org/10.48550/arXiv.2212.00067)
- Zucker, C., Speagle, J. S., Schlafly, E. F., et al. 2020, *A&A*, 633, A51, doi: [10.1051/0004-6361/201936145](https://doi.org/10.1051/0004-6361/201936145)
- . 2019, *ApJ*, 879, 125, doi: [10.3847/1538-4357/ab2388](https://doi.org/10.3847/1538-4357/ab2388)